Spring 1-1-2017

NIST Microwave Blackbody: the Design, Testing, and Verification of a Conical Brightness Temperature Source

Derek Anderson Houtz
University of Colorado at Boulder, derek.houtz@colorado.edu

University of Colorado Boulder
Department of Aerospace Engineering and Sciences
Funded by the National Institute of Standards and Technology

NIST MICROWAVE BLACKBODY

The design, testing, and verification of a conical brightness temperature source

Derek Anderson Houtz

Revised Apr 2017

This thesis entitled:

"NIST microwave blackbody: The design, testing, and verification of a conical brightness temperature source" written by Derek Anderson Houtz

has been approved for the degree Doctor of Philosophy in the Department of Aerospace Engineering and Sciences

_____

Committee chair: Dr. William Emery

_____

Dr. Albin Gasiewski

Date_____

The final copy of this thesis has been examined by the signatories, and we find that both the content and the form meet acceptable presentation standards of scholarly work in the above mentioned discipline.

Houtz, Derek A. (Ph.D., Department of Aerospace Engineering and Sciences)

NIST microwave blackbody: The design, testing, and verification of a conical brightness temperature source

Thesis directed by Professor William Emery and research conducted under the supervision of David Walker

Abstract:

Microwave radiometers allow remote sensing of earth and atmospheric temperatures from space, anytime, anywhere, through clouds, and in the dark. Data from microwave radiometers are high-impact operational inputs to weather forecasts, and are used to provide a vast array of climate data products including land and sea surface temperatures, soil moisture, ocean salinity, cloud precipitation and moisture height profiles, and even wind speed and direction, to name a few. Space-borne microwave radiometers have a major weakness when it comes to long-term climate trends due to their lack of traceability. Because there is no standard, or absolute reference, for microwave brightness temperature, nationally or internationally, individual instruments must each rely on their own internal calibration source to set an absolute reference to the fundamental unit of Kelvin. This causes each subsequent instrument to have a calibration offset and there is no 'true' reference. The work introduced in this thesis addresses this vacancy by proposing and introducing a NIST microwave brightness temperature source that may act as the primary reference. The NIST standard will allow pre-launch calibration of radiometers across a broad range of remote sensing pertinent frequencies between 18 GHz and 220 GHz. The blackbody will be capable of reaching temperatures ranging between liquid nitrogen boiling at approximately 77 K and warm-target temperature of 350 K. The brightness temperature of the source has associated standard uncertainty ranging as a function of frequency between 0.084 K and 0.111 K. The standard can be transferred to the calibration source in the instrument, providing traceability of all subsequent measurements back to the primary standard. The development of the NIST standard source involved predicting and measuring its brightness temperature, and minimizing the associated uncertainty of this quantity. Uniform and constant physical temperature along with well characterized and maximized emissivity are fundamental to a well characterized blackbody. The chosen geometry is a microwave absorber coated copper cone. Electromagnetic and thermal simulations are introduced to optimize the design. Experimental verifications of the simulated quantities confirm the predicted performance of the blackbody.

Acknowledgements

I would like to acknowledge the following people for their generous contributions without which this work would not have been possible.

Dazhen Gu for his infinite patience for my interrupting questions and always going above and beyond to teach me and further my understanding, rather than simply answer a question.

Richard Wylde and everyone at Thomas Keating Ltd. for their patience and hard work collaborating on this design and fabricating the standards.

Axel Murk for his helpful advice and experience and providing some high-frequency material measurements of Stycast absorber samples.

Arne Schroder for helpful discussions on HFSS and GO modeling of conical blackbodies and for providing BoR-MoM simulations results for comparison.

Karl Jacob for performing free-space measurements of Carbonyl-loaded Stycast samples at 75 GHz and above.

Michael Janezic for teaching me to measure waveguide loaded material samples using the vector network analyzer (VNA).

Sung Kim for providing Nicolson-Ross-Weir method code for material property extraction.

Edward Kim for his support and promoting of the NIST blackbody in NASA and JPSS circles.

Nathan Orloff for fighting along with me to secure the purchase of the NIST HPC machine that allowed electromagnetic finite element solutions of the blackbody.

Shannon Brown for provided advice on the cryogenic performance of Emerson & Cuming Eccosorb.

David Novotny for providing measured antenna efficiency quantity for our radiometric measurements and effective blackbody brightness temperature calculations.

Bill Tandy and Bill Goode for their generous collaboration with the Ball Experimental Sea Surface Temperature (BESST) infrared imager.

My advising committee have been incredibly supportive, sacrificing their time, and contributing knowledge to help make this project proposal into the doctoral thesis it is now.

Contents

List of Figures

I. BACKGROUND

Passive microwave remote sensing has its foremost application in environmental remote sensing, typically of the earth. Radiometers are capable of measuring the small amounts of microwave power naturally emitted as a function of a body's physical temperature and emissivity. The theory of this emission is based on Planck's law of thermal radiation. By quantifying the amount of microwave radiation emitted from land, sea, or clouds, a myriad of environmental parameters may be extracted. Some examples of these climatological variables include sea surface temperature, land surface temperature, cloud liquid water content profiles, ocean wind speed and direction, soil moisture, ocean salinity and countless others. By exploiting the broad spectrum of microwave frequencies, microwave radiometry has become an invaluable tool for weather forecasting and study of earth's climate as well as distant planets and moons.

The spectral radiance measured by a radiometer in a given frequency band is typically expressed as microwave brightness temperature, related to the amount of energy emitted by a 'blackbody' at a given temperature. The theory of brightness temperature relies heavily on Planck's law and the concept of a blackbody.

> *A black body is an idealized physical body that absorbs all incident electromagnetic radiation, regardless of frequency or angle of incidence. (...)*
> *A black body in thermal equilibrium (that is, at a constant temperature) emits electromagnetic radiation called black-body radiation. The radiation is emitted according to Planck's law, meaning that it has a spectrum that is determined by the temperature alone, not by the body's shape or composition.*
> *A black body in thermal equilibrium has two notable properties:*
> *1. It is an ideal emitter: at every frequency, it emits as much energy as – or more energy than – any other body at the same temperature.*
> 2. *It is a diffuse emitter: the energy is radiated isotropically, independent of direction.* [1]

This concept is critical to understanding the remainder of the following thesis, wherein the design of an approximate blackbody is discussed. The term blackbody is used in the remainder of this document to refer to a physically realizable approximation of a theoretical blackbody. Microwave brightness temperature is expressed in absolute temperature units of Kelvin, or occasionally

Rankine, because the amount of radiation emitted is related to its absolute temperature. A body at absolute zero will not emit any blackbody radiation. Though Kelvin is a fundamental SI unit, until recently there was no standardized traceability between the absolute temperature unit and microwave brightness temperature. The National Institute of Standards and Technology recently demonstrated traceability between the Kelvin of physical temperature and brightness temperature using the NIST noise temperature radiometer 'gold standards' [2]. The use of gold-standard radiometers demonstrated calibration standard uncertainty to within ±0.7 K at best. In order for such a standard to be broadly useful to the environmental remote sensing community, it requires lower uncertainties, the level to which we discuss in the following paragraphs.

Due to the absence of a reference source and lack of traceability among space-borne radiometer measurements, various techniques have been implemented to "recalibrate", "cross-calibrate" or compare data post-launch from different instruments. Some techniques have employed setting a 'stable' reference source on earth such as Antarctica [3, 4] or the amazon rainforest [5, 6]. These 'references' tend to break down across different instruments, antenna patterns, frequencies, and orbits, and it becomes difficult to obtain a directly comparable measurement. The many unknowns, e.g. incidence angle and frequency dependencies, of these 'references' can be modeled and they can work reasonably well for short-term relative cross-calibration, but for long-term climate trends an absolute reference becomes a necessity. In fact, it is misleading to call this type of comparison a calibration at all because with the lack of a primary reference only precision is being investigated and there is no tie to accuracy, to the fundamental units of Kelvin. These sorts of post-launch calibrations are often called simultaneous nadir overpass (SNO) [7] or inter-satellite calibration [8].

A technique of achieving agreement between radiometric measurements on different instruments, due to the lack of a standard, involves arbitrarily assigning a 'reference' instrument and aligning other instruments accordingly. As in [9] the NOAA 18 and NOAA 15 satellites are chosen as this 'reference' and other NOAA Microwave Sounding Unit (MSU) instruments are compared accordingly. Figure 1 shows the mean global brightness temperature of different MSU channels for different NOAA satellites. The offsets between instruments can be considered errors due to absolute calibration, and are observed to be larger than 1 K in some cases. It is also clear that temporal calibration drifts occur particularly between NOAA 15 and NOAA 16 on the order of 0.5 K on certain channels. With long-term global temperature changes on the order of 0.1 K per decade [10], the need for a more accurate reference becomes apparent. Temporal calibration

drifts will not be remedied by the ground-based reference standard discussed herein but it will provide a pre-launch standard point of absolute reference as opposed to the arbitrary 'reference' sources previously used.

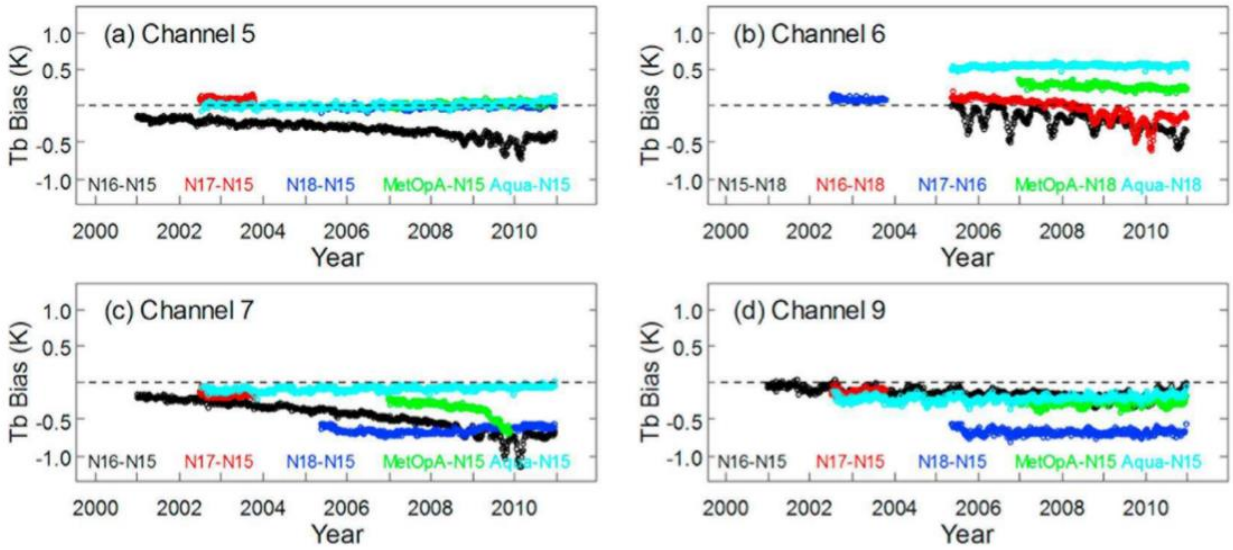

Figure 1: Comparison of Global Mean Temperatures of NOAA Satellites

The National Institute of Standards and Technology (NIST) is responsible for maintaining national standards for spectral irradiance and electromagnetic intensity. NIST provides calibration services and traceability certificates for infrared [11], visible [12], and ultraviolet [13] parts of the electromagnetic spectrum. The microwave part of the spectrum has been slower to develop a free-space irradiance calibration service at NIST because of the increased complexity of designing such a standard. The demonstration of a radiometer-based standard of [2] was the necessary first step, but as mentioned previously this approach is only capable of achieving ±0.7 K calibration uncertainty. Attempts to quantify the necessary brightness temperature accuracy for valuable extraction of various climate variables has yielded the following requirements for microwave radiometer measured climate variables [14].

Table 1: Requirements for Climate Variable Accuracy

Climate Variable	Accuracy	Stability (per decade)
Troposphere temperature	0.5 K	0.04 K
Stratosphere temperature	1.0 K	0.08 K

Water-vapor	1.0 K	0.08 K
Cloud liquid water path	0.3 K	0.1 K
Precipitation	1.25 K	0.03 K
Sea surface temperature	0.03 K	0.01 K

It is clear that from this small sampling of microwave radiometer derived data products, an absolute calibration uncertainty of less than 0.7 K is necessary to make traceability worthwhile for new instruments. Realistically speaking, and as will be shown throughout the remainder of the following report, 0.03 K accuracy would currently be an insurmountable goal, but we can certainly improve upon 0.7 K. The pre-launch NIST standard would provide the absolute accuracy and transfer the brightness temperature standard to a space-borne instrument's internal calibration reference. The long-term per decade stability would then be up to the individual instrument to maintain. Physical effects such as degradation of reflectors [15], and ferrite switches [16] can cause long-term drifts, or occasionally drifts in stability can only be recognized, but the underlying source remains unknown [17].

Measurements from microwave radiometers, particularly the temperature sounding channels between 50 GHz and 60 GHz, have a significant impact on numerical weather prediction (NWP) models [18]. The water vapor sounding channels near 183 GHz have more recently been assimilated into numerical weather prediction models and also have a significant impact on the accuracy of weather prediction [19]. Calibration biases in radiometric data result in biases in NWP modeled temperatures, particularly amplified in the polar regions [18]. Post processing bias correction algorithms allow removal of calibration biases from individual instruments to minimize residuals in the numerical model, but this process lacks any traceability to absolute temperature units, providing only relative statements about temperature [20].

The goal of the NIST standard microwave blackbody was to achieve a traceable calibration accuracy at frequencies between 18 GHz and 220 GHz of less than 0.1 K. The NIST standard should provide this calibration uncertainty independent of radiometer geometry, antenna pattern, or polarization. The NIST standard will be a variable temperature blackbody ranging between liquid nitrogen temperatures of approximately 80 K up to above ambient warm temperature of 350 K.

II. INTRODUCTION

The National Institute of Standards and Technology (NIST) has had an ongoing microwave remote sensing project since 2001 (with a lapse from 2006-2008). The project has worked towards creating, maintaining and improving a national standard for microwave brightness temperature. This thesis discusses the design, fabrication, and verification of the NIST microwave blackbody. The blackbody will serve as the national primary standard for brightness temperature between 18 GHz and 220 GHz.

From its inception, the design has been configured to allow integration with the calibration system of the Advanced Technology Microwave Sounded (ATMS) instrument. ATMS currently flies on the Suomi NPP satellite, and additional iterations will be launched on future polar-orbiting satellites commissioned by the Joint Polar Satellite System (JPSS), a collaboration between the National Oceanic and Atmospheric Administration (NOAA) and the National Aeronautics and Space Administration (NASA). Recent discussions with the European Space Agency (ESA) have also led to the strong possibility of future collaboration regarding the second generation meteorological satellites, MetOp Second-Gen. Providing the NIST traceable standard to ESA and JPSS would provide international traceability to and between two prominent operational microwave radiometers, and would increase the accuracy of weather models and long-term climate records [21]. The Global Space-based Inter-Calibration System (GSICS) [22] has been studying the impact of biases across instruments and satellites, and would greatly benefit from having two operational radiometers that are traceable and pre-launch inter-calibrated.

By referring to a brightness temperature calibration source as a blackbody we are implying that the source emits microwave radiation according to Planck's law, also known as the blackbody curve. The theoretical blackbody has an emissivity of unity, and thus the physical temperature is the only parameter necessary to describe the microwave radiance as a function of wavelength or frequency. In reality, we can only approximate a theoretical blackbody with a finite emissivity less than one. Maximizing the microwave emissivity allows straightforward characterization of brightness temperature by eliminating concerns of temperature and frequency dependence, and maximizes the emitted microwave power for a given temperature. A calibration source of arbitrary, but characterized emissivity is feasible, but maximizing the emissivity minimizes uncertainty and simplifies the uncertainty budget analysis.

In order to calculate microwave radiance or brightness temperature following Planck's law, or Rayleigh-Jean's approximation, the physical temperature must be expressed as a single scalar value. This assumes that the entirety of the body is at a single spatially uniform and temporally steady temperature. We show that in practice we can express this temperature as a spatial integral over the temperature field of the body, but in general, in order to effectively approximate a theoretical blackbody, we want to minimize temperature gradients.

The concept of a primary standard is fundamentally different than the concept of a transfer standard. The blackbody calibration source discussed here is intended to perform as a primary reference standard, directly traceable to the fundamental SI units of Kelvin. The NIST gold standard radiometers are based on two primary standards, the ambient load and the cryogenic load, that act as calibration references for the highly linear detector of the radiometer, and the two calibration standards are individually traceable with quantified uncertainty to the fundamental unit of Kelvin. The uncertainty in this traceability path is what we call 'type B' uncertainty [23], and has also been called systematic error, or absolute accuracy. The path of traceability for the standard radiometers stems from the calibration of the temperature sensors in the primary standards and eventually propagates to the brightness temperature in Kelvin. The traceability path to the fundamental unit has uncertainty contributions from: the cryogenic load emissivity, the ambient load emissivity, power ratios, mismatch factors, asymmetry, connector repeatability, isolation, frequency offset, and sensor nonlinearity [24].

The proposed primary blackbody source simplifies the traceability path for free-space brightness temperature units to decrease the achievable type B uncertainty. Instead of having nine contributing uncertainty terms we will have three; associated with emissivity, physical temperature, and antenna pattern. The antenna will be measurement-dependent, on an individual basis, so, in order to minimize the uncertainty associated with the brightness temperature of the blackbody we minimize uncertainties due to emissivity and physical temperature.

III. INITIAL DESIGN

A. Geometry

i. Space-borne and heritage geometries

The typical on-orbit calibration target design consists of an array of square pyramidal structures coated with a microwave absorbing material. From a high-frequency, ray-trace-approximating perspective, these structures allow multiple bounces of incoming radiation, increasing the probability of absorption. The larger the height-to-base aspect ratio, the more expected bounces before the wave is reflected back towards the viewing antenna, and thus the better the performance [25]. The performance of the pyramidal array targets is frequency dependent and varies as a function of the pyramid height and base size [26, 27]. This design is not optimal for emissivity or temperature gradient reduction, and is used mostly as a compromise between performance versus size and mass in aircraft and space-borne instruments. Figure 2 shows a photograph of two examples of these pyramidal array type targets with different base to height aspect ratio, and Figure 23 shows the engineering drawing with cross sectional view example.

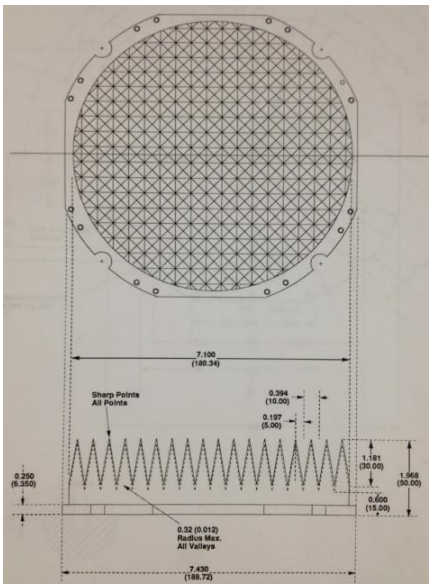

Figure 2: (left) Two pyramidal array microwave calibration targets, & Figure 3: (right) Engineering drawing of calibration target

ii. Unique Geometries

An alternative and more broadband absorbing geometry is the conical or wedge shaped cavity. Some recent projects such as the Atacama Large Millimeter Array (ALMA) telescope have utilized a variation of the larger but more effective conical cavity blackbody [28]. The conical target follows the multiple bounce principle similar to the pyramidal arrays, but allows for a broader operating frequency range because of the lack of interference with the periodic structures; i.e., Bragg scattering. The conical design is also attractive from the thermal perspective, decreasing temperature gradients compared to the traditional geometries, as discussed in section IV. Figure 4 shows a geometric optics ray trace diagram example of the multiple bounces experienced by the incident wave [28]. The geometric optics approach is an approximation used when the wavelength is much smaller than the aperture of the cone, appropriate across all but the small apex tip of the cone. The cross section of the wedge or conical geometry appears similar to the valley between two tines of a pyramidal array, but with this larger single cavity geometry the shape appears essentially the same across the wavelengths of interest.

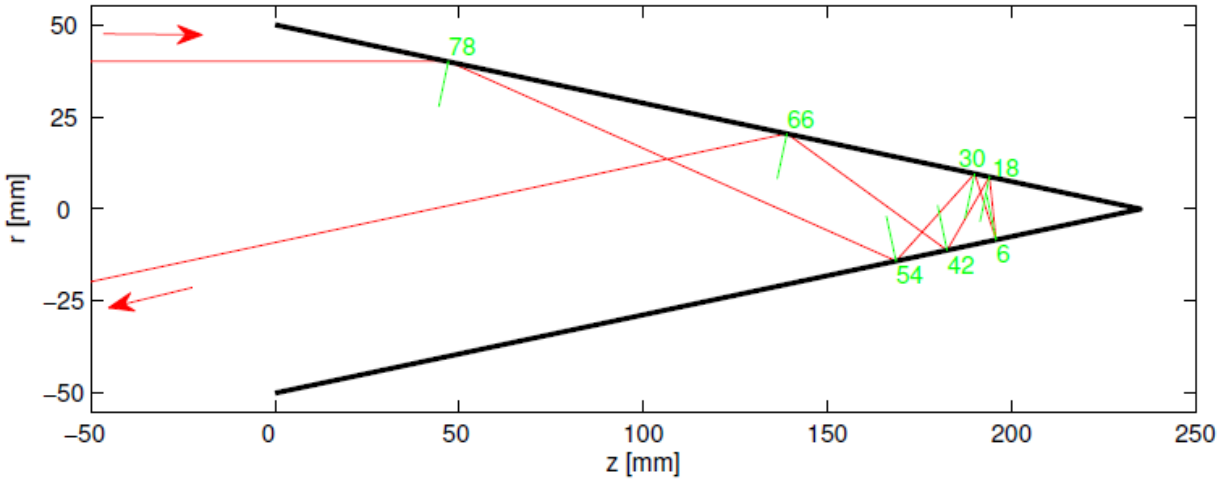

Figure 4: Example of Multiple Bounce Geometry with Ray Tracing. The green values denote the angle between the ray and the normal to the surface.

In a two-dimensional sense, the wedge and circular cone structures are identical, the difference coming in the third dimension, or polarization. As one might expect, and as is seen in the literature [29] and confirmed by our simulations, the wedge shows polarization dependence across the two linearly aligned axes. The wedge geometry can provide exceptional matching and

emissivity when calibrating radiometers of a single polarization [30], but must be rotated 90 degrees to achieve similar calibration accuracy at the orthogonal linear polarization. One of the requirements of the NIST blackbody, for the purpose of compatibility maximization, is to be polarization independent, so for this reason the wedge target was deemed incapable of fulfilling the requirements and other solutions were pursued. In a vacuum testing environment, we do not want to depressurize the chamber, rotate a wedge 90 degrees and re-pressurize the chamber to calibrate dual-polarized channels.

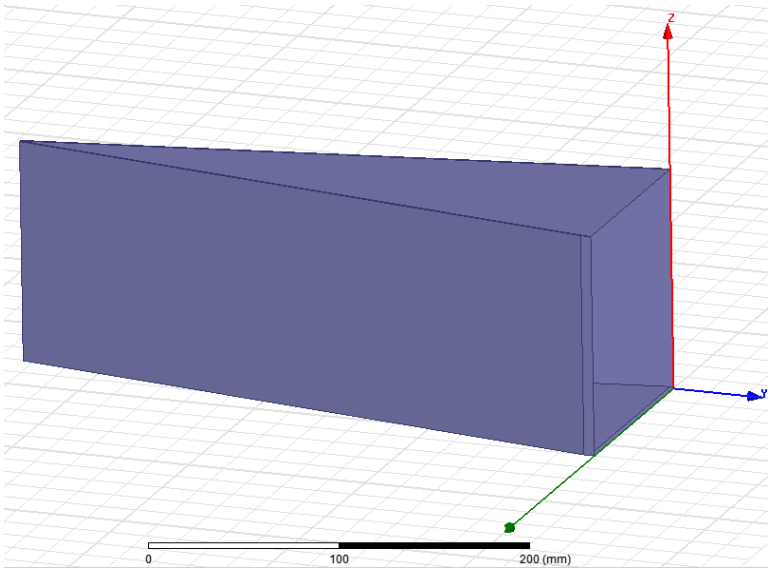

Figure 5: Example of wedge cavity geometry

The circular cone cavity target has been shown to be capable of low reflections, and thus high emissivity over a broad range of frequencies and minimize physical temperature gradients [31]. For a laboratory-based standard, the mass and size constraints are more relaxed than for a flight target, so a conical geometry is feasible.

iii. Circular cone

The geometry of a circular cone can be constrained to an angle and an aperture radius. The radius must be considered as a function of the electromagnetic wavelength to be calibrated, while the cone angle remains a geometric variable. As can be inferred from Figure 4, from the high-frequency approximation perspective, as the cone angle decreases the number of ray bounces increases. If the radius is fixed, the length of the cone increases as cone angle decreases. There are still physical constraints tied to the target such as the requirement for it to fit within a thermal-

vacuum chamber, so it is not practical to make the cone angle excessively small. The cone angle was chosen relatively early in the design based on these practical constraints.

During the initial design phase, many variables remained undetermined such as the thickness and type of microwave absorber to be used. It became necessary to first determine the geometry and then begin iterating to optimize microwave emissivity while maintaining minimal temperature gradients. Early in the design process, the lack of material properties for electromagnetic absorbers was a challenge for modeling the target performance above 40 GHz. As discussed in section V. A., a fitting was applied to the material data to extrapolate up to 220 GHz. It was determined that the physical constraints of the vacuum chamber, along with the required radii, limited the cone angle of the cone to greater than about 8 degrees. The geometric optics modeling approach discussed in section V.B. was applied as a function of cone angle in order to select a functional geometry. Figure 6 shows an example of predicted target reflectance as a function of cone half angle and frequency. This particular solution example is for the final Stycast absorber design, discussed in the following sections. The decision was originally made using different varieties of Emerson & Cuming Eccosorb CR properties, but the process was the same. A half-cone angle of 10° was selected as a compromise between physical size and electromagnetic performance. This angle provided predicted reflectance under -40 dB across the frequency spectrum with some safety factor, and also allowed some safety factor for size clearance in the thermal-vacuum chamber.

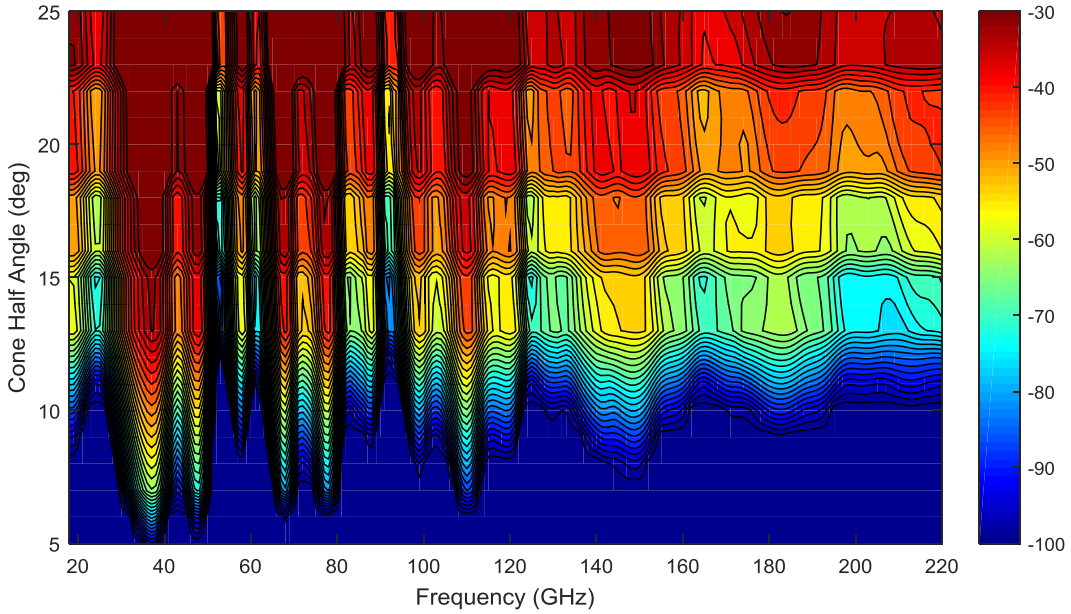

Figure 6: Example cone angle selection matrix

B. Design Constraints

i. ATMS

One of the first goals for the NIST standard target is to transfer traceability to the third iteration of the ATMS instrument, aboard the JPSS-2 satellite. This satellite is scheduled for launch in 2021 and is scheduled for pre-launch calibration at the instrument level in 2019. The contractor for building and calibrating the previous two iterations of ATMS was Northrup-Grumman, and this is expected to stay the same for the JPSS-2 copy of the instrument. The NIST standard was designed to interface with the Northrop-Grumman thermal-vacuum calibration system and hardware. Two standards of different radius were designed and built in order to calibrate the two ATMS antenna feed arrays and reflectors.

The current ATMS pre-launch calibration scheme uses four external targets, one for each of the feed apertures at cold and variable temperature. The cold target is designed to mimic the on-orbit, cold-sky calibration, and the variable temperature target is designed to mimic the earth-scene brightness temperature. The NIST standard targets have been designed to replace the variable temperature targets in this calibration system. The ATMS external calibration targets are oval-shaped pyramidal arrays elongated in the scan-axis to maximize the number of averaged target looks per scan. The NIST targets, to maintain polarization independence and for manufacturability, are circular aperture devices, so they will not completely fill the same scan angle as the original targets. The radii of the two targets were chosen to interface with the current instrument-level vacuum chamber calibration hardware. The larger target to be used to calibrate frequencies between 23 GHz and 60 GHz has a radius of 108.5 mm, and the smaller with a radius of 68.5mm will calibrate frequencies between 88.2 GHz and 190.3 GHz.

The vacuum chamber allows a target length of about 1 m, and the large target with 10° half-cone angle has an internal absorber length of 0.62 m, allowing clearance for copper base structure, vacuum compatible connectors and tubing, and wiring for temperature monitoring sensors.

ii. Thermal-Vacuum compatibility

Thermal-vacuum chamber compatibility was a concern for the entirety of the design process. All components had to be designed with vacuum compatibility in mind and stand up to low pressure cycling. Outgassing and total mass loss of chosen materials was also a concern. As

will be discussed in the following sections, a sheet of closed-cell foam is used in the design. Without access to a vacuum chamber for testing, we relied on outside knowledge and experience to make decisions on the foam material. We had laboratory experience with, and previous material data on a closed-cell polyethylene foam, Plastizote Zotefoam HD-30. The number in the name refers to the density, 30 kg/m^3. A collaborator shared a proprietary report that indicated that HD-30 does not withstand cycling in the vacuum chamber, and the least dense similar material that did survive was Zotefoam HD-60. Since this report was an internal proprietary study it cannot be referenced, and we were not able to perform vacuum testing of the materials ourselves. We obtained some samples of this material and did electromagnetic testing, reported in section V.A..

The heat exchanger copper tubing connectors require vacuum compatible interfacing. The KF-16 connector was chosen for its dependability and heritage in vacuum related applications.

All screws used in construction have been hollowed out to avoid voids in tapped holes, and are thus vacuum ready. The thermal paste, Kapton tape, and copper tape combination used to secure the temperature sensors is likely not vacuum ready, and the leads on the sensors are not cryogenically compatible, so the temperature sensors will need to be reinstalled before cryogenic and vacuum use. The PRTs currently installed have also not been calibrated down to liquid nitrogen temperatures, so this will also need to be revisited before thermal-vacuum use.

iii. Size & Mass

As mentioned earlier, the mass and size constraints on the pre-launch calibration system are considerably more relaxed than for typical on-orbit calibration sources. The weight requirement was determined by the practical need to move the blackbody within the lab, and was set at under 50 kg, or able to be safely carried by 2 people. The final mass of the 108.5 mm radius target was about 40 kg and the 68.5 mm target was about 20 kg.

The size requirement set by the limited space in the Northrop-Grumman vacuum chamber was less than 1 m in length for both targets. The 108.5 mm radius target has a final total length of 0.645 m and the 68.5 mm radius target a total length of 0.330 m.

IV. THERMAL DESIGN

A. Heat Exchanger

The requirement to cryogenically cool and heat the target above ambient temperatures required a robust thermal design. Many space-borne targets utilize electric resistance heaters to achieve temperatures above ambient background. Electric heaters require a temperature controller to switch the heater and maintain a stable temperature, and have been shown to be capable of achieving stable target temperatures above 350 K in the lab [32]. Resistance heating was considered for the above-ambient operation of the NIST standard target, but an alternative solution was still required to attain cryogenic temperature operation. Liquid nitrogen was the obvious path to achieving temperatures near 80 K, though there have been some alternative cooling techniques recently demonstrated using peltiers [33].

The vacuum chamber at Northrop-Grumman is equipped with plumbing and equipment to pump liquid nitrogen through a cold plate and a cold-scene calibration target. It became apparent that utilizing as much of the existing infrastructure as possible would simplify the design and maximize the probability of success during pre-launch calibration of ATMS. The decision was made to create a heat-exchanger-like hose system spiraling around the back of the microwave absorber cone. Liquid nitrogen will be pumped through copper tubes by the existing hardware at Northrop-Grumman. Another step to simplify the system included the decision to use the same heat exchanger concept for target heating as well. An 'engineering fluid' with high boiling point, low freezing temperature, and high thermal conductivity, 3M Novec 7500, will be pumped through the heat exchanger lines by a refrigerating and heating temperature controlled fluid circulator for target use above ambient. A heated fluid circulator is used to maintain the thermally conductive fluid at a constant temperature. An ultra-low temperature circulator will be used to reach temperatures down to -100 C (173 K) to cover the required variable-temperature range for ATMS. The low temperature circulator has not yet been purchased but multiple such products exist on the market and are capable of stability within ±0.01 K.

When designing the helical tubing path, we considered the possibility of liquid nitrogen boil-off creating gas bubbles in the upper sections of the coils. If gas bubbles formed, we would expect to see vertical temperature gradients when operated in horizontal orientation, the requirement for ATMS thermal-vacuum calibration. Upon discussion with experts in the field, it

was decided that with sufficient flow rate and pressure from the nitrogen circulation pump we should be able to avoid formation of gas bubbles.

Another aspect of the heat exchanger tubing design was the decision to include two parallel helical lines, to allow counter-flow. The concept behind this design inclusion was that fluid straight out of the circulator, at or very near the exact setting temperature, would be first contacting the cone at both the apex and the aperture end. If the fluid was only flowing from one end to the other there may be temperature gradients along the length of heat exchanger tubing as heat was transferred along the length of tubing. The outside of the cone and tubing will be heavily insulated to minimize heat loss from the fluid. Theoretically, when running hot fluid through the lines there is a temperature minimum at the midpoint on the tubing between the two inlets, the insulation and use of high thermal conductivity copper backing has minimized this gradient effect to equalize the steady-state temperature. This temperature minimum in the tubing lines is assumed negligible relative to the gradients on the absorber surface for a well-insulated heat exchanger.

B. Tubing Spacing

The spacing between the helical tubing wraps is an important factor for maintaining temperature uniformity. The high thermal conductivity of copper helps to evenly distribute temperature across the cone, and the large thermal mass of the copper in the design slows any temporal drifts of temperature.

A simplified CAD model was constructed to study the effect of tubing spacing on the resulting absorber surface temperature. A section of the cone was taken and approximated as a flat sheet. The tubes were attached to the copper with the same surface area to which the tubes will be electroformed to the copper cone in the actual target, a 5mm contact length in the tube cross section. The copper tubes are approximated as square cross sections for finite element meshing efficiency. Figure 7 shows an example of the simplified geometry employed for the heat exchanger simulations. The sides parallel to the tubes are assigned as adiabatic boundaries which are effectively symmetry boundaries in thermal modeling. The HD-60 outer surface is assigned as a heat flux boundary with the value determined from the simulation in the proceeding section, C. The heat flux out of the HD-60 surface is a function of position along the cone so the maximum value is taken, corresponding to approximately the outer aperture end of the cone. The tubes are assigned as constant temperature boundary conditions at 350 K assuming any temperature

gradients in or along the tube are negligible for this study. The material properties, thermal conductivity, density, and specific heat capacity are defined from the material specification sheets or built-in values for copper. The steady-state temperature distribution is solved for and visualized on the absorber surface. Figure 8 shows the resulting temperature distribution on the surface of the Stycast absorber.

With the 40 mm separation distance between tubing coils, we see about 0.02 K gradient across the surface between tubing sections. It would have been difficult mechanically to wrap the coils any closer and still fasten the cone base, and drill holes for PRTS in the copper base structure. Also, as the wrap distance decreases the total length of tubing required increases, which both increases the back pressure to fluid through the tubing, and increases likelihood of temperature gradients in the longitudinal tube direction. The 40 mm distance was decided to be a good compromise, and a 0.02 K gradient is relatively small compared to the goal uncertainty budget of 0.1 K.

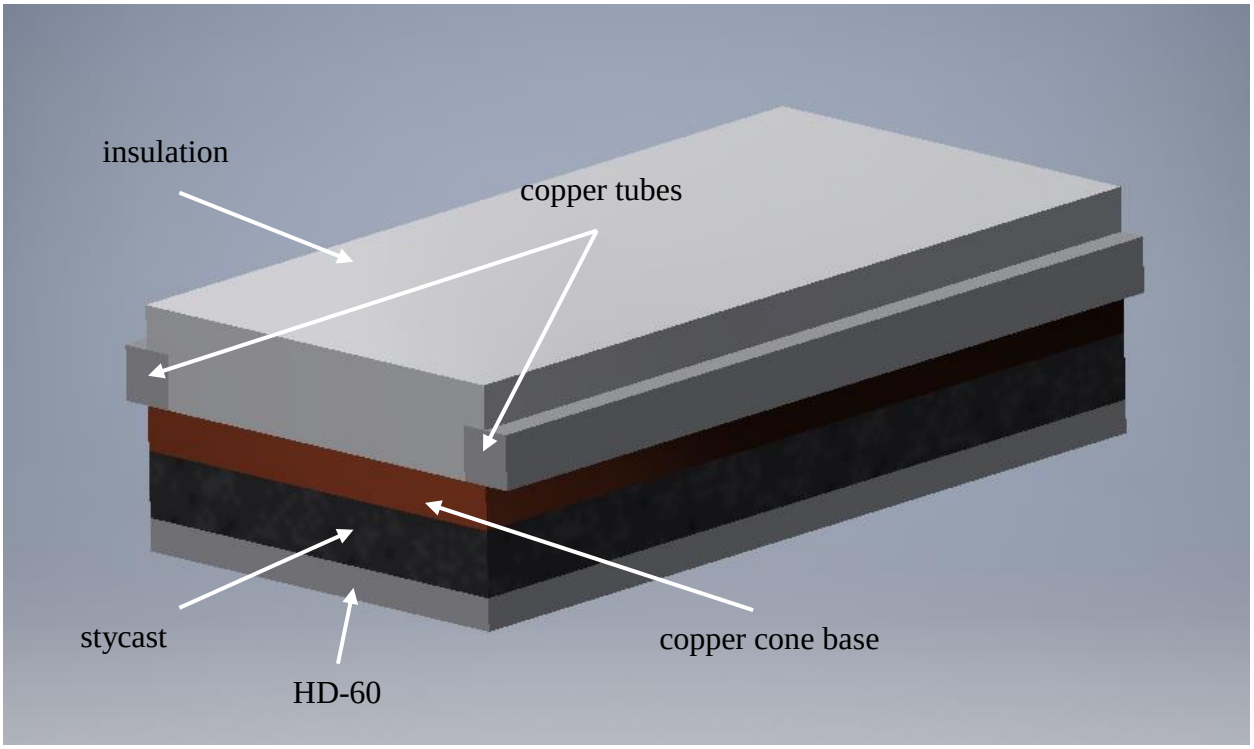

Figure 7: Example simplified flattened geometry for heat exchanger tubing study

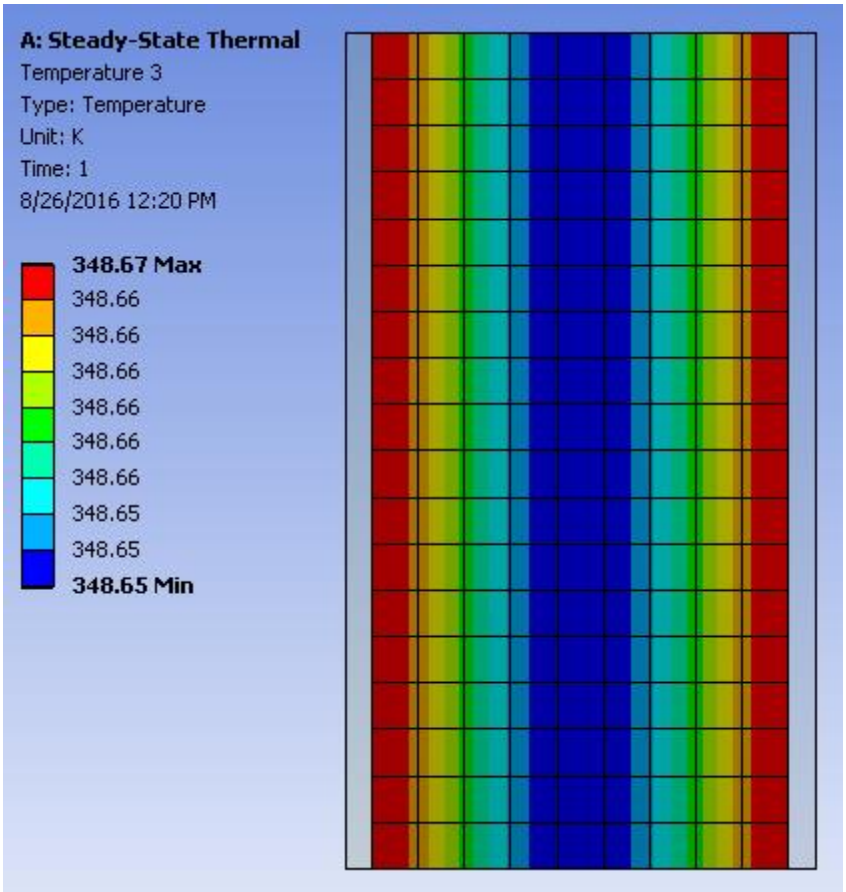

Figure 8: Temperature distribution on absorber surface

C. Full Thermal Simulation

Much of the thermal aspect of the design relied on finite element model (FEM) simulations and computational fluid dynamics (CFD) software. For laboratory use, outside of a thermal-vacuum chamber, the physical temperature of the blackbody is influenced by heat transfer by both convection and radiation. Convective heat transfer coefficients can be quite difficult to determine analytically on anything but a simple geometry due to the complexity of airflow. Our laboratory measurements will be conducted in an anechoic chamber with dimensions of approximately 1.5 m length by 1.2 m width by 1.2 m height. In the model, the anechoic chamber is ventilated by an inlet and an outlet fan, to keep the background temperature steady when working with the heated target. The tradeoff to keeping a steady uniform background temperature is the additional heat loss due to convection from the fans. This tradeoff is a topic of future study and has not been experimentally determined yet. The fans have not been installed in the chamber yet to allow for

this study. When the target is used in vacuum we only have to worry about radiative heat loss, so we simulate both laboratory and thermal-vacuum conditions to verify the design.

The convective heat transfer coefficient is difficult to obtain analytically, particularly for low velocity forced convection on complex geometry. We elected to use the FEM along with commercial CFD software, ANSYS CFX to model the full anechoic chamber convective environment. This software has the added benefit that its infrared ray-trace heat transfer capabilities are robust so the same software and model can be adapted to both the laboratory anechoic chamber and the thermal-vacuum chamber cases.

The anechoic chamber and simplistic target design are modeled in 3D computer aided design (CAD) program Autodesk Inventor to be input to CFX for meshing. Figure 9 shows the simplified cone geometry utilized for the full fluid simulation. Due to meshing constraints and complexity the helical tubing structure was omitted from the model, and the copper cone was assumed isothermal, a good approximation as shown in section B, above. Figure 10 shows the simplified cone geometry in the anechoic chamber at approximately its mounting location. The inlet and outlet fan holes are also visible on the front and rear sides of the chamber. The pyramidal absorber structures on the chamber walls are neglected due to complexity. The mounting structure has not yet been determined so the cone is seen 'floating' in the chamber. The mounting structure is assumed to have a negligible effect on the convective airflow, though heat transfer to conduction through the mount is a considerable heat-sink, increasing required heat flux from the circulating temperature control fluid.

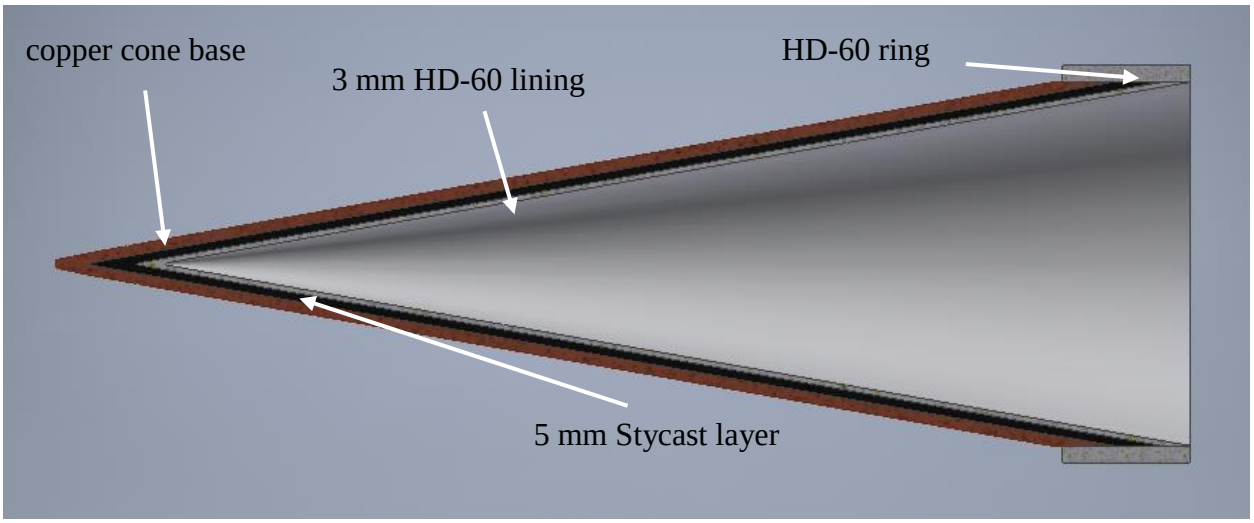

Figure 9: Cross-section of simplified target for CFX thermal simulations

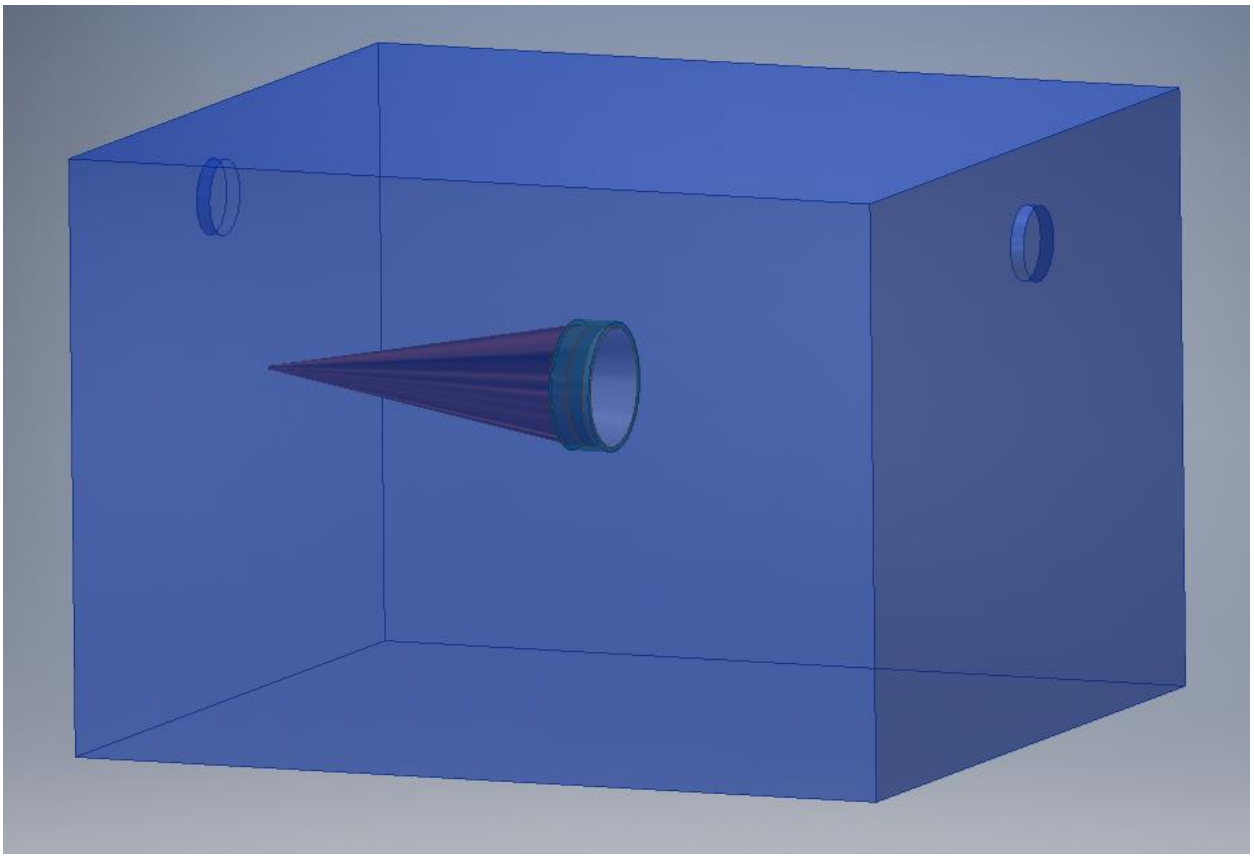

Figure 10: Example of simple target in anechoic chamber

The outer surface of the copper cone was defined as an isothermal boundary condition, at 350 K for the laboratory case, and at both 350 K and liquid nitrogen 77 K for the thermal-vacuum chamber case. The chamber walls are defined as adiabatic boundary conditions, due to the thick foam microwave absorber lining, acting as an excellent thermal insulator. The inlet and outlet fans are defined as inlet and outlet boundary conditions with ambient inlet temperature and mass flow rates according to the fan specification. The 120 mm computer fans move approximately 0.04045 kg/s, but we throttle them down to a quarter of this to reduce convection. The material properties are defined based on specification sheets. The properties for pure Stycast 2850 FT with 23 LV catalyst are used because the thermal conductivity of Carbonyl loaded Stycast are not known and we did not have time to measure the thermal properties. Many of the material thermal properties used in the FEM simulation are provided in Table 2.

Table 2: Material properties for thermal simulations

Material	Density	Thermal Conductivity	Specific Heat Capacity	Linear Coefficient of Thermal Expansion
Zotefoams HD-60	60 kg/m^3 [*34*]	0.0572 W/m/K [34]	2285.5 J/kg/K [35]	5 10^{-6}/K [*36*]
Stycast 2850 FT with 23 LV catalyst	2190 kg/m^3 [37]	1.02 W/m/K [37]	209 J/kg/K [*38*]	39.4 10^{-6}/K [37]
Eccosorb CR absorber	1600-4900 [39] kg/m^3	1.2552 W/m/K [39]	N/A	30 10^{-6}/K [39]
Copper	8960 kg/m^3 [40]	401 W/m/K [40]	385 J/kg/K [40]	17.7 10^{-6}/K [41]
G-10	1800 kg/m^3 [42]	0.288 W/m/K [42]	N/A	9.9 10^{-6}/K [42]

We use the CFX FEM software to solve the steady-state conditions in the chamber. The solver utilizes the 3D Navier-Stokes equations with heat-flux and energy conservation to fully solve the system. Buoyancy effects are included, an important factor for gravity-induced convection, and turbulence. The solver uses the P-1 radiation model [43][44].

Figure 11 shows the solved velocity streamlines in the chamber with the target's copper surface heated to 350 K. The convective heat-loss or convection coefficient is spatially dependent and is determined by the air temperature and velocity across the solid interfaces. This is the motivation behind using computational fluid dynamics software. Figure 12 shows the solved absorber surface temperature with the target heated to 350 K in the anechoic chamber including the HD-60 polyethylene layer. Figure 13 shows the solved absorber surface temperature of the target cooled to 77 K with liquid nitrogen in vacuum. The vacuum chamber solutions do not require fluid dynamics capabilities, but the software was already setup and meshed, and the CFX software has a fully capable radiation solver. The temperature gradients between the cone apex and the knife-edge aperture are shown to be up to 1 K or greater, but we must consider that the resulting effective brightness temperature will be antenna pattern and distance dependent. The closer the antenna to the cone, the greater the contribution from the inner region's temperature;

analogously, the higher the directivity of the antenna, the greater the contribution from the inner region of the cone. The effective brightness temperature quantifies this contribution, though the ultimate goal was to be antenna independent, requiring the minimization of temperature gradients across the whole cone. The output of the CFD temperature simulation is saved to a file for later processing of the effective brightness temperature in section V.C..

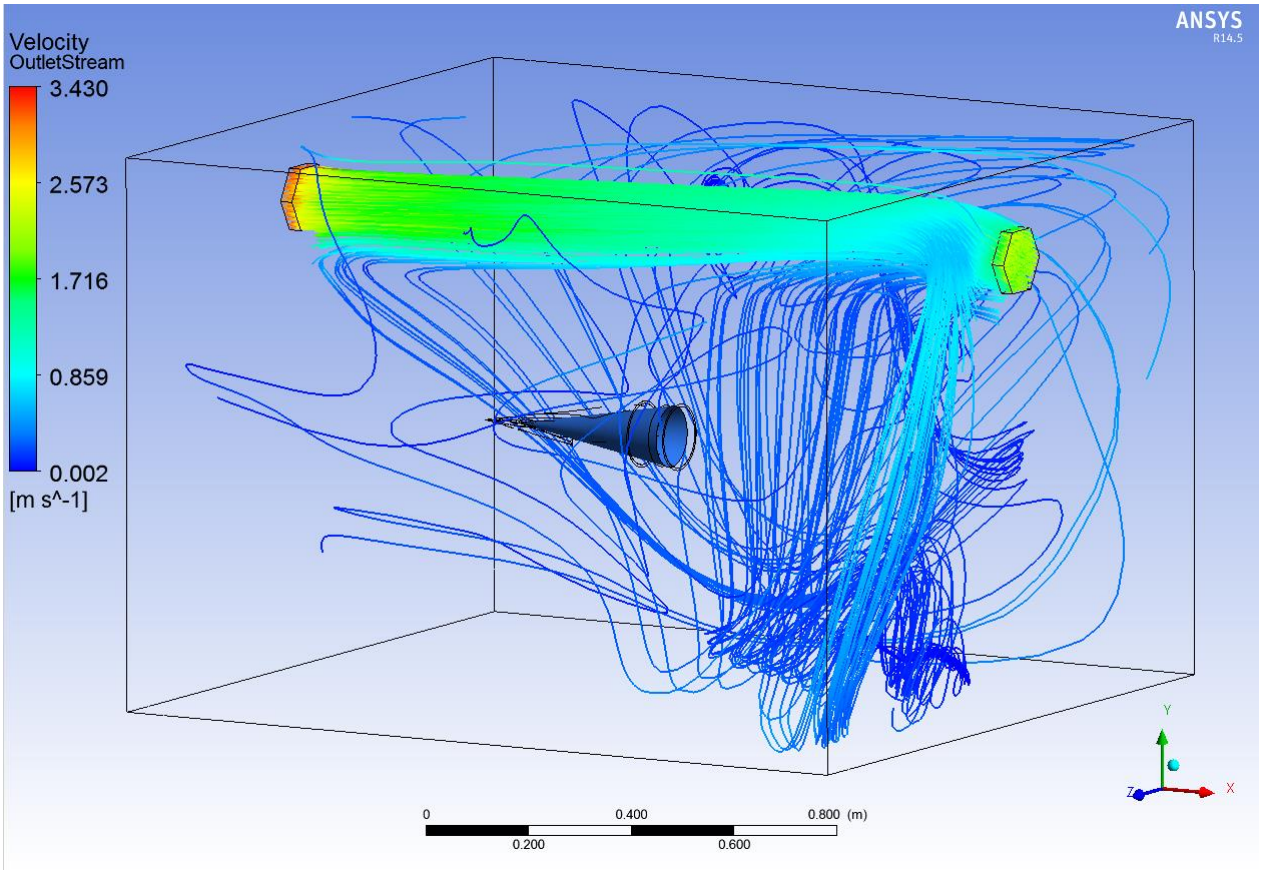

Figure 11: Solved velocity streamlines in anechoic chamber with fans at one-quarter throttle. A pre-requisite to determining convection coefficient and temperature fields.

The full chamber geometry and CFD software setup is user-intensive and quite time consuming, so only the likely design candidates were simulated in the full solver, and design decisions were made based on comparisons of a few total absorber thicknesses and insulation thicknesses. These CFX simulations have only considered the simplified geometry suspended in the chamber. We also investigate the actual mount structure and full geometry to determine the steady-state temperatures of parts when the target is heated or cooled.

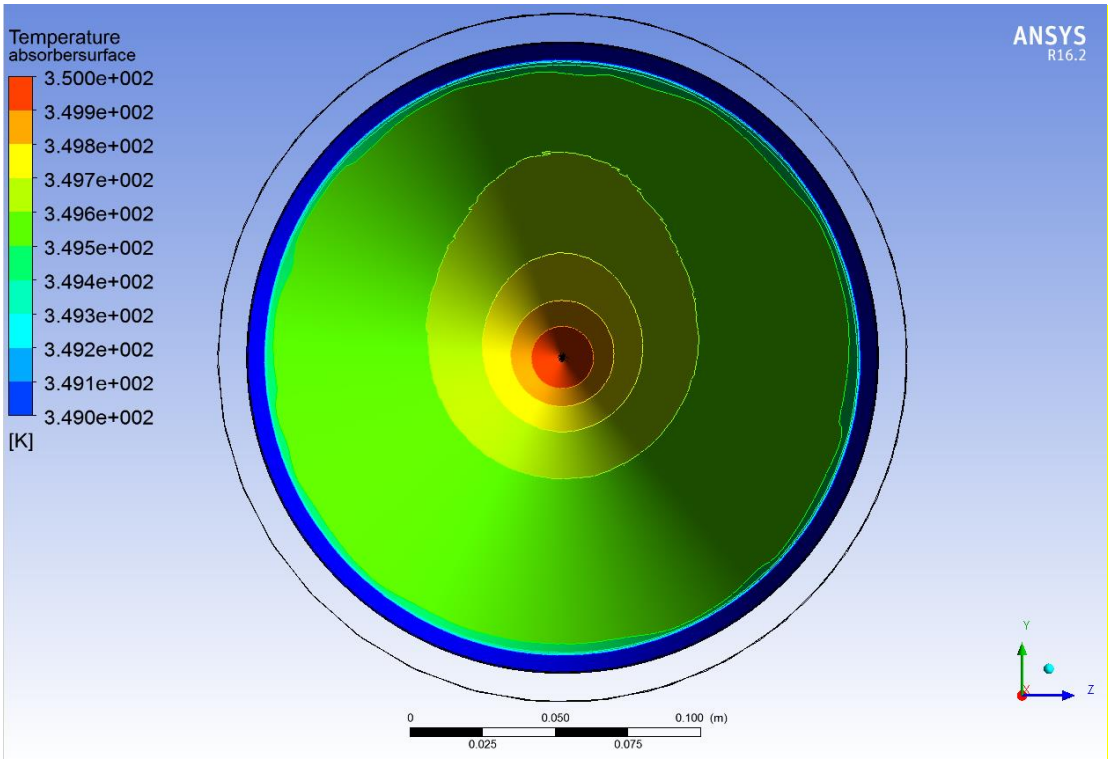

Figure 12: Solved temperature field on absorber surface. Target heated to 350 K in ambient laboratory. Includes 5 mm thick HD-60 layer.

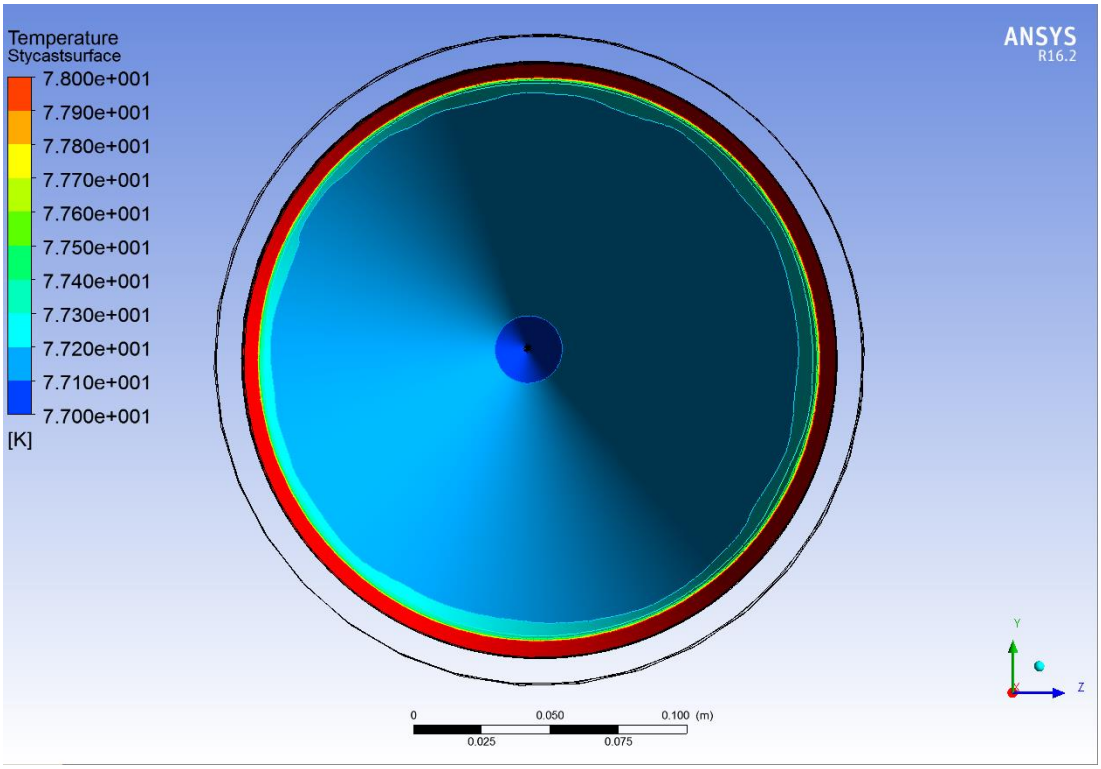

Figure 13: Solved temperature field on absorber surface. Target cooled to 77 K in ambient-temperature vacuum environment (radiation only). Includes 5 mm thick HD-60 layer.

D. Full Geometry Steady-State Simulation

An attempt was made during the design process to thermally isolate the copper and absorber cones from the mounting structure and surroundings. The contact points to the copper were made from G10, otherwise known as Garolite, a low thermal conductivity composite with high strength and high operating temperature. This material was intended to insulate the heated or cooled copper from the mounting structure and thus from the rest of the surrounding chamber and background.

The CAD assembly file for the full target mount structure is input to the ANSYS steady-state temperature solver. The copper tubes are assigned as constant temperature boundaries with a temperature of 350 K. The HD-60 surface is assigned with radiation heat-loss to ambient temperature and the mean surface convection coefficient determined from the simulations in section C is used. We see that at steady-state the entire mounting structure reaches a temperature close to 350 K. This is not an issue for the mounting structure itself, but will have to be considered when designing interfaces with sensitive hardware such as in the thermal-vacuum chamber for ATMS calibration. Figure 14 shows the steady-state temperature distribution for the full mounting structure and cone geometry heated to 350 K.

The cold steady-state temperature was not simulated but it can be assumed that the heavy copper thermal mass will dominate and the temperature of the entire structure will eventually also reach approximately 77 K. Excluded here was the insulation around the copper, also a polyethylene sheet-type insulation, as well as any heat loss from the outside of the structure. The mounting structure will take a long time to equalize due to the low thermal conductivity of G10, whereas the copper cone should reach steady temperature relatively quicker because of its high thermal conductivity. We expect that most calibrations can be completed before the entire mounting structure reaches 350 K, but this was not confirmed by simulation. We examine the time to reach heated temperatures experimentally in section VI.D.

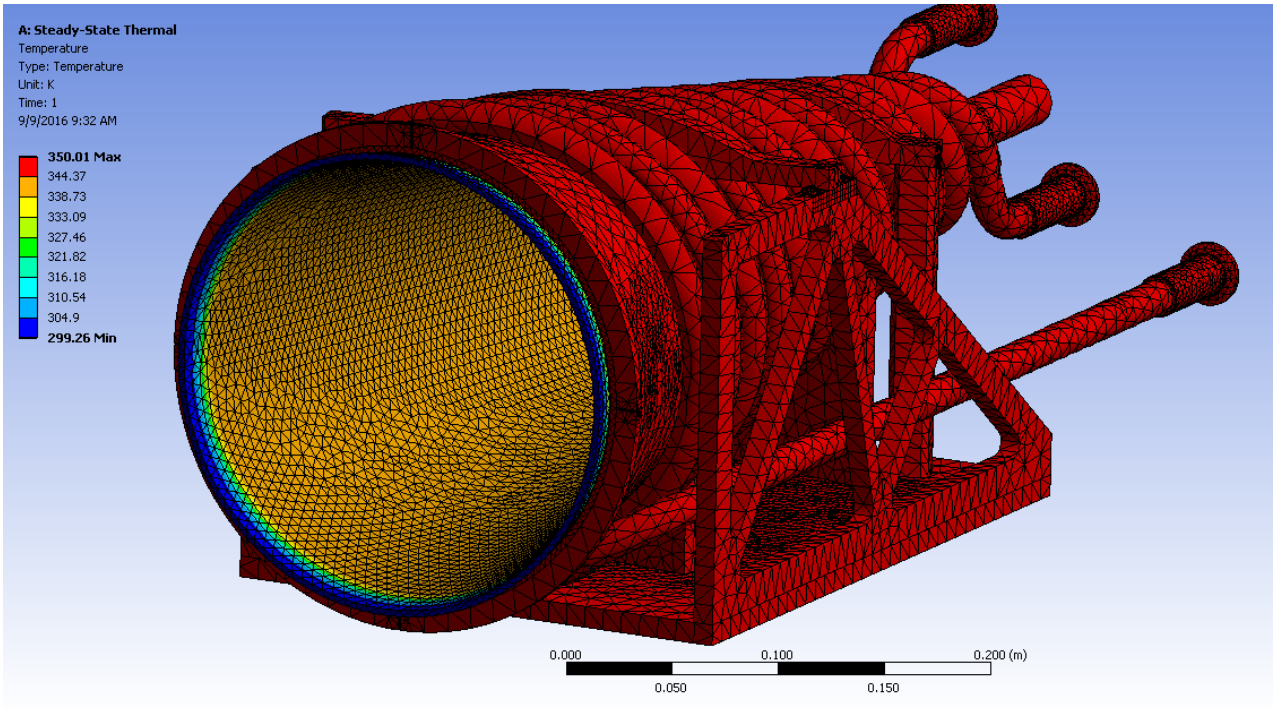

Figure 14: Steady-state temperature field of full mounting assembly when heated to 350 K

E. Absorber

The initial design included the use of a commercially available Emerson & Cuming Eccosorb microwave absorber with heritage in many previous microwave calibration sources [45][46][47]. One benefit of using commercial absorber materials was that there were data available on their thermal and electromagnetic material properties. It turned out that the absorber material selection was not as trivial as it initially seemed due to cold temperature issues.

The design and simulations proceeded with the Eccosorb materials until shortly after the manufacturer contract was awarded. It was then brought to our attention that Eccosorb CR, the epoxy-based castable absorbers we planned to use, do not handle cold temperatures very well, particularly in large geometries. We were advised by Axel Murk and Richard Wylde about the Sentinel-3 wedge calibration target, and Shannon Brown of JPL on a small conical target, both had experienced cracking of these targets when exposed to cold temperatures. Both parties advised against using the Eccosorb CR down to liquid nitrogen temperatures as they had experienced the issues with cracking due to thermal contraction, and from the absorber becoming brittle at low temperatures.

Thomas Keating Ltd. advised us to proceed by using a different epoxy matrix from which they had formulated a microwave absorber. The suggested epoxy was Stycast 2850 FT with 23 LV catalyst. The 23 LV is designed for cold temperature use and the epoxy is advertised as having good thermal conductivity, a benefit for our thermal design. Though

Table 2 suggests that Eccosorb CR has a higher thermal conductivity then Stycast 2850 FT, we are unsure of the unloaded thermal properties of the base epoxy in the Eccosorb. We expect that the addition of the iron particles, or 'Part Y' according to Emerson & Cuming [39], increases the thermal conductivity, but this was never confirmed experimentally. The linear coefficient of thermal expansion of Eccosorb is also lower, hence closer to copper, which would suggest it would be a better material to bond to copper, but the Stycast with 23 LV catalyst is intended for low temperature use, and Thomas Keating would not warranty their work if we proceeded with Eccosorb.

One difficulty of using Stycast was that there exists no electromagnetic data on Stycast, and it appeared to contain alumina particles to increase the thermal conductivity. This was hypothesized to also increase the microwave reflectivity and thus lower emissivity. The electromagnetic performance ended up being satisfactory, as discussed in detail in section V.A., and the design proceeded with iron-carbonyl loaded Stycast absorber.

Due to the lack of published thermal properties of iron-carbonyl loaded Stycast, the properties of pure Stycast 2850 FT were used instead. It was hypothesized that the addition of iron carbonyl particles would increase the thermal conductivity of the mixture because iron has a high thermal conductivity. This hypothesis was not tested or confirmed, but we are rather confident that the addition of iron would not lower the thermal conductivity. Stycast 2850 FT when combined with catalyst 23 LV is considerably more pliable than Eccosorb CR, and maintains this pliability when brought to cold temperatures. The electromagnetic and thermal simulations were re-run for the Stycast properties, the absorber layer design was electromagnetically optimized for this absorber, and the manufacturing proceeded.

It was next discovered that when loaded with a high volume fill fraction of iron carbonyl, up to 50%, the epoxy would no longer bond to the copper base cone. We then introduced a layer of pure Stycast epoxy between the carbonyl loaded absorber and the copper to maintain a solid bond between the materials. This 1 mm layer would be detrimental to both the electromagnetic and thermal performance but was deemed necessary for structural integrity.

The initial absorber cone was cast to the layer specifications discussed in section V.B. and then cycled to -80 °C. The Stycast was not as flexible or cold-temperature-withstanding as initially believed. The absorber on the cold-cycled target cracked. Figure 15 shows the crack in the Stycast layers after removal from the freezer. The appearance of cracking when cycled to -80 °C (193 K) was concerning considering that we would be running it down to approximately 77 K. The bonding of the absorber to the copper was reconsidered as it was assumed that stress from differential thermal contraction at the interface caused the crack in the Stycast layer. We investigated the thermal stress and discuss this in the following sub-section F.

Figure 15: Cracked Stycast after cold-cycling of initial copper bonded absorber

In order to relieve the stress at the bonded interface we decided to allow the bodies to move freely, one inside the other. This design decision required some engineering to affix the absorber cone into the copper, maintaining thermal contact but eliminating the stress from bonded thermal contact. We also wanted to eliminate scatterers from the aperture ring, so clipping or pushing the absorber back into the copper was not a preferable solution. The solution we came up with was to pull the absorber cone in from the apex of the cone through a hole in the copper. A hole was drilled in the apex of the copper and a 'spigot' was cast in the first layer of absorber, the pure Stycast. A hole is tapped into the Stycast and a plastic screw is placed into it. The absorber cone

is pulled into the copper at the apex by this plastic screw. Tension is applied to the screw by a set of o-rings stacked under it. Figure 16 shows a sketch of this concept and Figure 17 shows a photograph of the finished device. Rather than an air release hole as depicted in the sketch, the final product utilizes a plastic screw with a hole bored through it instead, to avoid air-filled voids for vacuum compatibility. A thin layer of high thermal conductivity silver loaded grease is planned to be applied at the interface between the copper and Stycast to increase thermal contact, eliminate any air gaps, and fill any imperfections in the surfaces. This thermal paste has not been applied yet due to unknown guidelines for outgassing in the ATMS/Northrop-Grumman vacuum chamber. The high thermal-conductivity greases also have no specified performance at cryogenic temperatures, so some future testing will be required to verify its cryogenic compatibility.

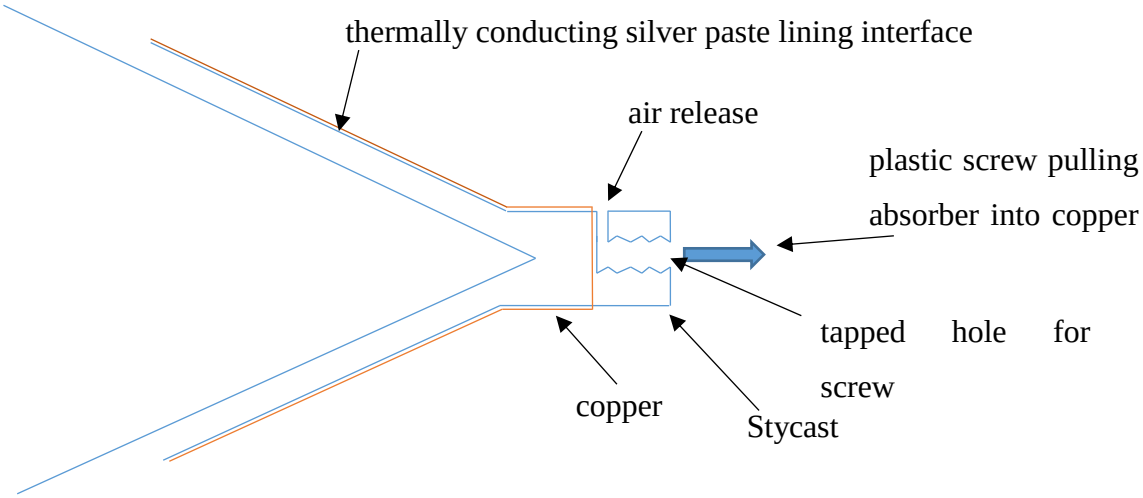

Figure 16: Conceptual drawing of apex absorber securing design

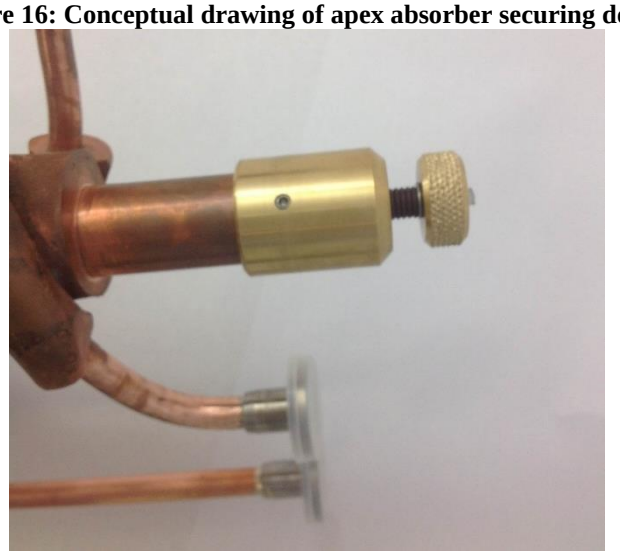

Figure 17: Photograph of absorber securing mechanism

F. Thermal Stress Analysis

The cracking of the first Stycast casting was concerning and prompted some analysis to determine a better solution for the next casting. Some thermal stress analyses were performed in ANSYS mechanical finite element software to investigate the levels of stress resulting from thermal contraction. The copper cone and 5 mm total thickness Stycast absorber piece were modeled in CAD and a bonded interface was set at ambient temperature. The modeled assembly was then cooled to liquid nitrogen temperature (77 K) and the stresses were examined. Figure 18 shows the equivalent, or von-Mises, stress contour on the Stycast layer. The maximum stress is seen at the apex of the cone which does not explain the crack we saw develop close to the aperture of the cone.

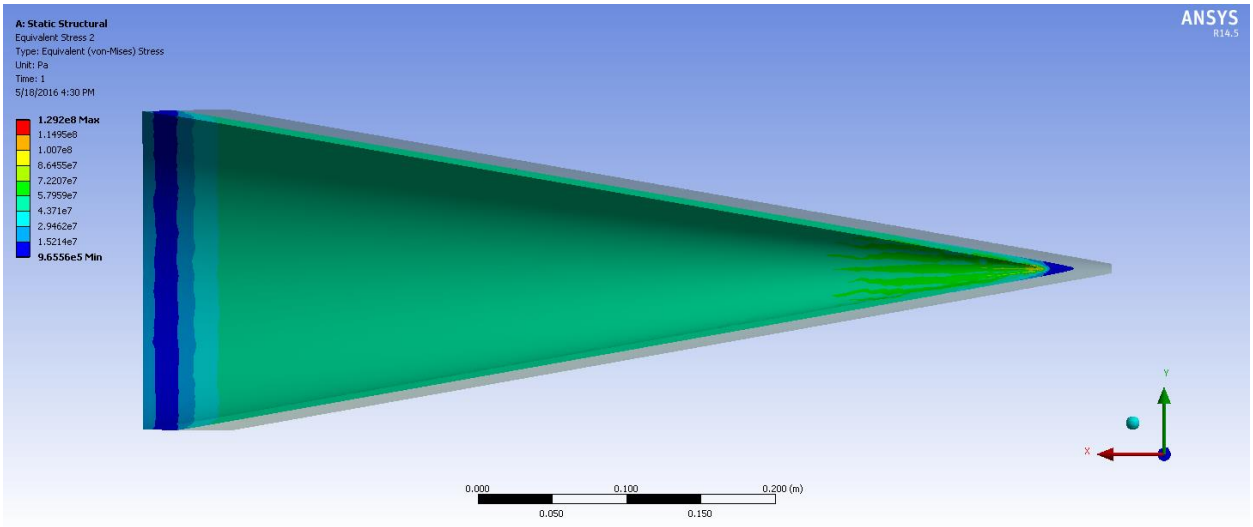

Figure 18: Von-Mises stress on 77 K Stycast due to bonded interface

We next examined the stress vectors to see if we could explain the location of the crack. The vector principal stress feature of ANSYS Mechanical allows visualization of the maximum principal stress vector. Principal stress transformation rotates the Cauchy stress tensor so that the off-diagonal terms in the 3 by 3 tensor are zeroed. The state of stress on a point can thus be expressed by 3 quantities, the principal stresses. The maximum of these three quantities is the maximum principal stress. Figure 19 shows the principal stress vectors on the simplified cone geometry. The vectors are hard to resolve in the full view, so a zoomed perspective is provided in Figure 20. We observe a change in direction of the maximum principal stress at the location highlighted in Figure 19. The maximum shear stress at the bonded interface between copper and

Stycast goes from being aligned with the cone axis to the orthogonal shear direction, acting radially around the cone. The location of this directional transition corresponds to the location of the crack on the cooled Stycast seen in Figure 15, the shape of the crack also suggests that the Stycast segment nearer to the apex of the cone pulled away causing the crack to run radially, and then propagating to the aperture edge.

The epoxy bond between the copper and Stycast was determined to be the source of the internal stress and the cause of cracking when the Stycast was cooled. This bond, due to direct casting of the Stycast absorber, maximized thermal contact between the surfaces, but could not tolerate the wide range of temperatures required for this device. The design decision was made to cast the absorber cone as a freestanding part, sacrificing some thermal contact as a tradeoff for eliminating the possibility of cracking the absorber. With the absorber freestanding within the copper, fixed only at the apex, the internal stresses in the system are effectively eliminated.

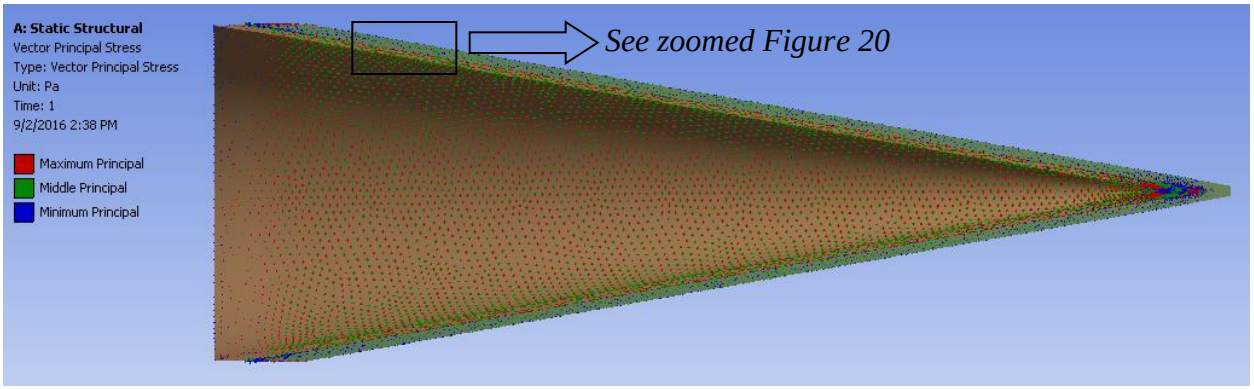

Figure 19: Principal stress vector visualization from ANSYS Mechanical on cross section of 3D cone assembly

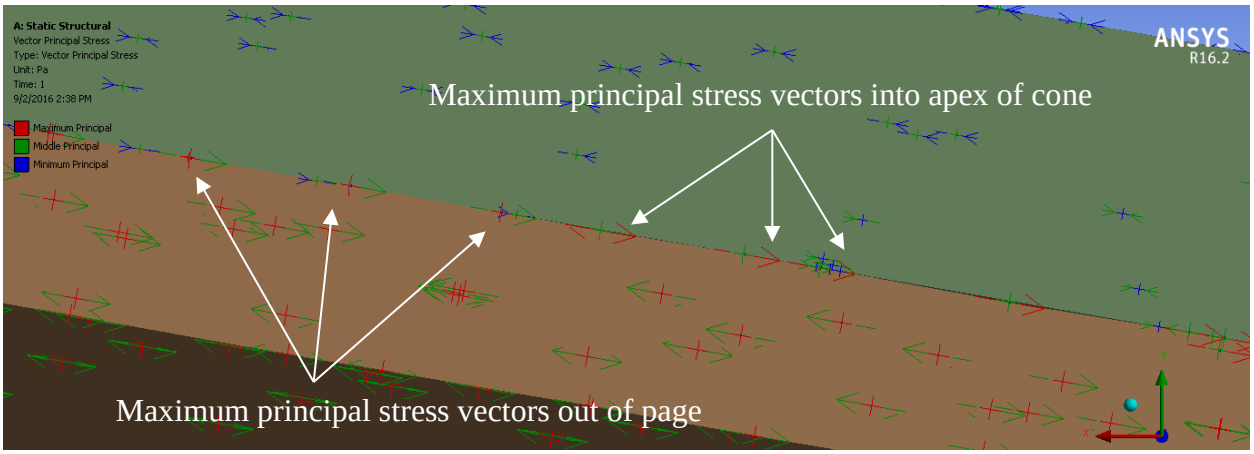

Figure 20: Zoom-in of principal stress vectors at transition point

G. PRT Location

Monitoring the physical temperature of the blackbody is critical to expressing brightness temperature. Calibrated temperature sensors provide traceability to the fundamental unit of Kelvin, to link physical temperature to brightness temperature. Monitoring temperature in multiple locations near the emitting object provides knowledge of temperature uniformity and stability.

Traditionally, temperature sensors have been embedded in pyramidal array calibration sources at various locations to monitor temperature gradients in the pyramidal axis and in the plane of the array. We take a similar approach with the conical target, aiming to monitor any temperature gradients on the copper, in the radial plane and the cone axis. When used in the laboratory with a horizontal orientation we expect to see some gradients in the radial plane due to buoyant convective heat transfer. Simulations have suggested a rotational airflow within the cone creating slightly higher temperatures on the top side of the cone due to rising heat and slightly cooler temperatures on the lower side. When the cone is used in thermal-vacuum chamber we expect to see negligible temperature gradients in the radial plane, due to cone-axis symmetric radiation being the only heat loss mechanism.

Heat loss to radiation will cause some temperature gradients, particularly near the aperture of the blackbody. The radiation heat loss is a function of the surfaces being radiated to and their thermal infrared emissivities. At the apex of the cone, the hemispherical solid angle of a point radiator is largely subtended by the cone itself, and there is a relatively small aperture through which this radiator can view the background. The ratio of background to cone solid angle increases towards the aperture so we expect to see more radiative heat exchange. The closed-cell polyethylene foam (HD-60) insulation layer aids in reducing temperature gradients from both convection and radiation due to its low thermal conductivity, low infrared emissivity, and opacity to infrared radiation.

The location of the platinum resistance thermometers (PRT) was chosen to provide a full range of information about the radial and cone-axis temperature distributions. It is assumed that the copper body will have reached steady-state when calibrations are being performed so we are concerned most heavily with spatial temperature differences and not temporal. There may be some small temporal drifts due to imperfect temperature stability of the circulator, but these are considered negligible, as will be shown in experimental results.

The twelve PRT sensors on the larger target were spaced along four equally-spaced radial lines around the circular cross-section. Essentially, providing a plus sign configuration at three individual cone-axis locations. The engineering drawing of the PRT locations is shown in Figure 21. The eight PRTs in the smaller target were installed in the same radial locations and at the same two axis positions closest to the aperture. The third row of PRTs closest to the aperture were excluded for the smaller target.

The holes for PRTs were drilled 3.5 mm deep to avoid fully puncturing the copper cone. The holes were drilled to a diameter of 1.7 mm. It turned out upon receiving the target that many of the PRTs were on the larger end of the quoted tolerance of 1.6±0.25 mm so many of the holes were too small. It was also determined that having a significant part of the ~1 cm long ceramic PRT bead and lead wire sticking perpendicularly out of the copper was not optimal for thermal contact. Instead of using the drilled holes, the PRTs were installed horizontally following the manufacturer's, Lakeshore Cryotronics, procedure for PRT installation [48]. A small piece of Kapton tape was placed on the copper to prevent conductivity across the leads, and the PRT bead was placed directly on the copper with a small amount of zinc oxide thermal grease. The exposed leads are sandwiched with another piece of Kapton tape, and then the whole installation and PRT lead is covered with copper tape for optimal thermal contact.

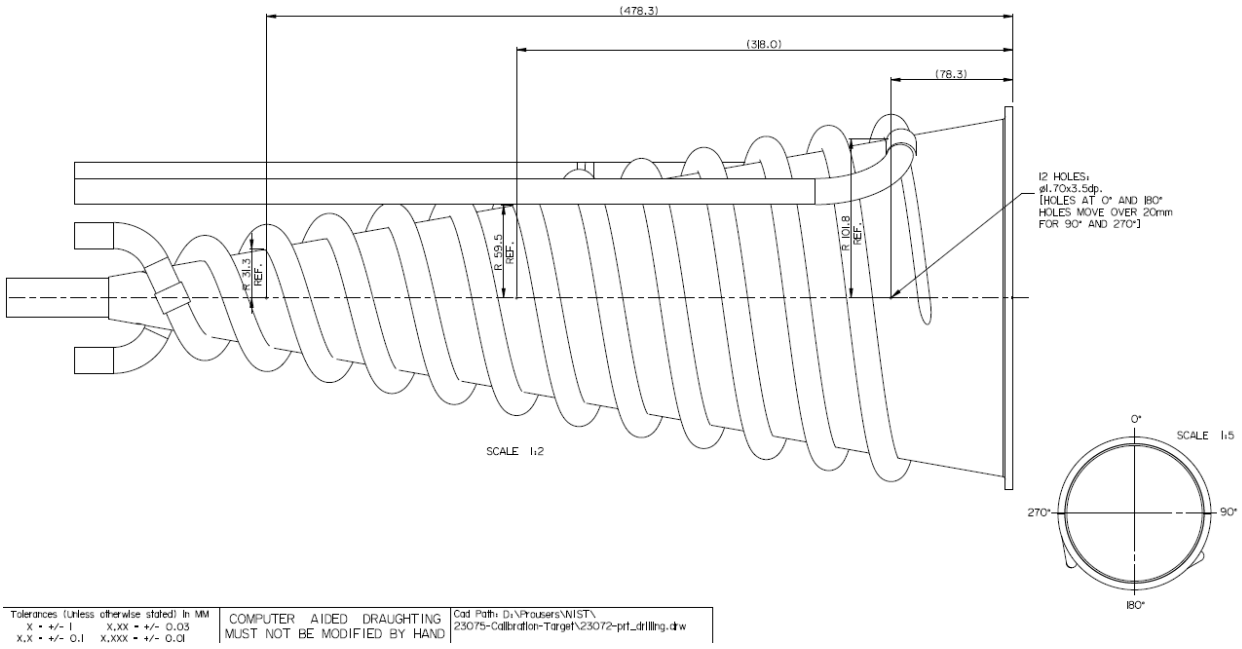

Figure 21: Engineering drawing of drilled PRT hole locations

V. ELECTROMAGNETIC DESIGN

A. Material property determination

Permittivity and permeability are the fundamental electromagnetic material properties, important for performance prediction, simulation, and engineering design of electrical systems, and most importantly, microwave blackbodies. Determining complex permeability and permittivity of low-loss microwave materials is often challenging. The implicit nature of the full physical relationship between these properties and measured scattering parameters of the material, and/or the sensitivity of the system, both make it difficult to arrive at the correct root, and to accurately fit the material parameters. Popular methods include the Nicholson-Ross-Weir (NRW) method [49][50] and NIST iterative nonlinear fitting technique [51]. We are specifically interested in the complex permittivity and permeability of iron carbonyl powder (CBI) loaded epoxy. Stycast 2850 FT with 23 LV catalyst was chosen for its cryogenic performance, but electromagnetic properties are unknown and required for design and simulation of the blackbody.

i. Measuring Unloaded Epoxy

The first step towards designing a new absorber material was measuring the unloaded epoxy material to see if it would be too highly reflective for use as an absorber. The chosen material, Stycast 2850 FT with the cryogenic compatible catalyst 23 LV, is loaded with alumina particles to increase thermal conductivity and low temperature performance, but this was hypothesized to also increase its dielectric constant and surface reflections. A pure epoxy with too high of a dielectric constant would result in a large impedance mismatch to air, large reflections, and would not be suitable as a base material for a magnetically lossy microwave absorber. The electromagnetic material properties of Stycast 2850 FT material are not in literature, and as far as we know have not been measured at the frequencies we are interested in. Samples of the pure epoxy were cast into WR-42 and WR-28 waveguide shims and measured.

A pervading challenge encountered when characterizing electromagnetic properties is the error resulting from the numerical singularity that exists when the sample thickness is equal to an integer multiple of half the guide wavelength. The singularity is highly pronounced in low-loss materials because there is little damping from attenuation loss in the sample. Baker-Jarvis [52] explains that in the low-loss limit, the permeability and permittivity are only expressed as a product

and are non-separable. This resonance was seen in the unloaded Stycast sample and required modification of the standard material property extraction techniques. Because the low frequency regime was considered to be the most sensitive and design critical, when this resonance influenced the WR-42 band, alternative extraction techniques were sought.

The remainder of the discussion in this subsection has been peer-reviewed and published in [53]. The method introduced shows improvement in determination of complex permittivity and permeability near resonance points for low-loss materials in transmission lines. The method requires only a single material sample and measurements at a single frequency, and we see improvements over the comparable alternative methods. The theory and results presented pertain to the TE_{10} mode in a waveguide transmission line, but the general method can be broadly applied to many types of transmission including on-wafer coplanar-waveguide (CPW) and coaxial lines. By adding a one-port reflection measurement of the sample terminated with a short, we are able to create an alternate independent fitting parameter and eliminate the use of the noisy and low-magnitude S_{11} term from the two-port measurement. In section *a* we introduce and formulate the single-mode theory for the reflection coefficient of the shorted, lossy, and magnetic sample, and discuss the inclusion of this scattering measurement into the implicit least-squares fitting for permittivity and permeability determination. In section *b* we formulate the analytical uncertainty for the new method, and section *c* outlines the measurement setup for the experimental data. Section *d* presents the example data for a WR-42 waveguide line loaded with the pure Stycast epoxy, and for a sample of higher-loss iron-loaded Emerson & Cuming Eccosorb CR114 microwave absorber. Section *e* discusses results from a commercial finite element software used to generate representative S-parameter data in order to compare the method results to some 'true' permittivity and permeability values, as input to the modeler. The new method is compared to the NRW formulation and the iterative Baker-Jarvis method for both the experimental and simulated S-parameter data. Section *f* draws conclusions, discusses the implications, and touches on the benefits of the proposed electromagnetic material property extraction technique.

a. Theoretical Approach

We use a two port microwave network analyzer to measure scattering parameters and calculate the complex permittivity and permeability. All of the discussed methods are equally applicable to waveguide and coaxial measurements, though the examples discussed herein are

performed in waveguide. Following the implicit formulation of [52] for our symmetric and reciprocal samples, we can express the theoretical S-parameters as:

$$S_{11} = \frac{\Gamma(1-z^2)}{1-\Gamma^2 z^2}, \tag{1}$$

$$S_{21} = \frac{z(1-\Gamma^2)}{1-\Gamma^2 z^2}, \tag{2}$$

$$S_{22} = S_{11}, \tag{3}$$

$$S_{12} = S_{21}, \tag{4}$$

where z is $\exp(-\gamma L)$, L is the sample length, γ is the propagation constant and Γ is the reflection coefficient, both functions of the complex permittivity and complex permeability. These quantities are readily available as explicit expressions for many transmission lines. We omit the reference plane shift term for simplicity, and because the nature of our samples does not require it. Without the reference plane shift, (3) and (4) are redundant but provide additional degrees of freedom for the fitting. The traditional iterative method solves for the material parameters by minimizing the error between measured S-parameters and those theoretically calculated from (1)-(4). Typically, any nonlinear least-squares technique suffices, but the method used will vary the requirement of the initial guess in order to arrive at the correct root.

When the transmission line length is equivalent to an integer multiple of the half-wavelength of the guided transmission line wavelength ($n\frac{\lambda_g}{2}$, where n is an integer and λ_g is the guided wavelength in the transmission line), low-loss materials experience a resonance effect that causes a dip in S_{11} and a peak in S_{21}. This resonance effect has been widely recognized and various attempts have been made to circumvent and decrease the errors caused by it [54]-[60]. Hasar [54] proposes a combination of data at more than one frequency point, but this requires some assumptions about the material parameters across the frequency perturbation gap. Baker-Jarvis [55] studied a method using two samples of different thicknesses, but in addition to requiring two material samples, uncertainty in sample thickness can propagate to material properties, and inhomogeneity across the samples can also contribute to error. Baker-Jarvis also investigated two methods using short circuits, either two samples of different lengths, or measurements at two different positions in the line, both introducing more length-based uncertainties. Other alternative and modern methods have either only solved for permittivity, required a combination of

measurements at multiple frequencies, or individual data windowing and intensive processing [56][57][58][59][60].

The proposed short-circuit modified NIST iterative method introduces an additional, easy to perform, independent measurement to replace the two-port S_{11} and S_{22} measurements, and greatly reduces the influence of the resonance. The method allows solving both complex permittivity and complex permeability, at each individual measurement frequency, while decreasing overall uncertainty.

The samples we intend to measure are made from an epoxy material that has been cast into short, 3.6 mm, waveguide sections we call shims. This type of sample has the benefit of not suffering from air-gap uncertainty, the type encountered from an imperfect fit within the waveguide line, but we are also not able to move the sample within the sample holder. We have formulated the method discussed in this paper to allow for improved permittivity and permeability characterization of a single sample of this type.

We introduce a reflector or short-circuit to the system on one side of the sample. The short is placed directly behind the sample so that any air gap between the two is minimized. We then measure the one-port reflectance, S_{11}. There is still a resonance inside the sample with the short, but due to the altered setup this resonance occurs at a different frequency than for the traditional two-port measurement. The resonance wavelength of the shorted sample occurs at $\left(n+\frac{1}{2}\right)\frac{\lambda_g}{2}$. The benefit is that we can greatly improve the accuracy of the solution, particularly the real permittivity and permeability of low loss materials by decreasing the material parameter sensitivity to the S-parameters at both resonant frequencies. Instead of having a situation where all measurements experience a spike in S-parameter uncertainty and material property sensitivity to these uncertainties, we spread these spikes across two resonances allowing at least one measurement at each frequency unaffected by resonance. In addition, the signal amplitude is now much higher than in the two-port configuration, and the uncertainty of this measurement is considerably lower compared to the traditional S_{11} and S_{22} measurements in the two-port configuration. These combined effects will be shown to reduce the propagated material property uncertainty.

To obtain an analytic expression for the shorted S_{11} measurement, we follow an analysis similar to the derivation of (1) and (2) with the main difference being a perfect reflection on one

side of the sample as opposed to the interface to air. Figure 22 provides an illustration of the measurement setup and S_{11} calculation theory.

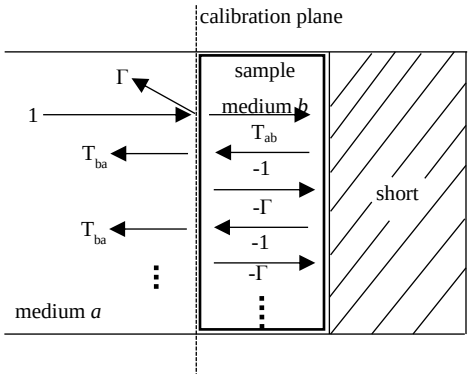

Figure 22: Illustration of shorted sample with reflection and transmission behavior.

The total S_{11} for the short, denoted S_{11s}, upon considering the infinite multipath reflections inside the sample becomes

$$S_{11s} = \Gamma - T_{ab}T_{ba}z^2 - T_{ab}T_{ba}\Gamma z^4 - T_{ab}T_{ba}\Gamma^2 z^6 + \cdots, \tag{5}$$

where T_{ab} is the transmission coefficient going from medium a (transmission line) to medium b (sample-loaded transmission line), and vice-versa for T_{ba}. This expression is recognized as a geometric series and rewritten in the form

$$S_{11s} = \Gamma - \frac{T_{ab}T_{ba}z^2}{1-\Gamma z^2}. \tag{6}$$

We further simplify using the relationships $T_{ab} = 1 + \Gamma$ and $T_{ba} = 1 - \Gamma$. The shorted-sample S_{11} expression is now expressed in terms of only the transmission coefficient z in the sample, and reflection coefficient Γ, similar to (1) and (2)

$$S_{11s} = \Gamma - \frac{(1-\Gamma^2)z^2}{1-\Gamma z^2}. \tag{7}$$

With this analytical expression and an experimental measurement of this term, we can replace the S_{11} and S_{22} terms obtained in the traditional two-port measurement of the standard Baker-Jarvis iterative method.

The objective function to be minimized for a nonlinear-least-squares-type fitting is now given as:

$$f(\varepsilon,\mu)=\left[\left(|S_{21}^{meas}|-|S_{21}^{pred}|\right)^2+\left(\frac{\angle S_{21}^{meas}-\angle S_{21}^{pred}}{\pi}\right)^2+\left(|S_{12}^{meas}|-|S_{12}^{pred}|\right)^2+\left(\frac{\angle S_{12}^{meas}-\angle S_{12}^{pred}}{\pi}\right)^2+\left(|S_{11s}^{meas}|-|S_{11s}^{pred}|\right)^2+\left(\frac{\angle S_{11s}^{meas}-\angle S_{11s}^{pred}}{\pi}\right)^2\right], \tag{8}$$

where the superscripts $meas$ and $pred$ refer to measured and predicted values respectfully.

b. Uncertainty

The NIST iterative technique has a well-established analytical Type-B uncertainty calculation for propagation of the systematic S-parameter and sample length errors into the permittivity and permeability [55]. The differential uncertainty analysis is assumed and the form for each component is given as

$$\Delta y_i=\sqrt{\sum_j^9\left(\frac{\partial y_i}{\partial x_j}\Delta x_j\right)^2}, \tag{9}$$

where y_i takes on four real values: $\varepsilon',\varepsilon'',\mu',\mu''$, where $\varepsilon_r=\varepsilon/\varepsilon_0=\ \varepsilon'-j\varepsilon''$ and $\mu_r=\mu/\mu_0=\ \mu'-j\mu''$. The nine quantities x_j are derived from the four complex values and one scalar quantity: $|S_{11}|$, $\angle S_{11}$, $|S_{21}|$, $\angle S_{21}$, $|S_{22}|$, $\angle S_{22}$, $|S_{12}|$, $\angle S_{12}$ and L, the sample length. The uncertainties Δx_j in the contributing terms are the standard measurement errors for the scattering parameters, and the uncertainty in the length is calculated from the standard deviation of ten individual measurements of the sample length. Because of the reciprocity in two-port measurements, the derivative terms for S_{11} in [55] can be used for S_{22} uncertainty and S_{21} terms can be substituted with S_{12} to complete the differential analysis. The uncertainty approach of [55] computes the Type-B uncertainty, assuming a direct relationship between the measured and solved parameters, but since the data are fit with a numerical non-linear-least-squares fitting technique, we also include the statistical uncertainty contribution resulting from the fitting. In the fitting model (1)-(4), we consider L as a constant and vary the material parameters to minimize the least-squares error with the measured values. We effectively have eight measurements and four unknowns, individually considering the real and imaginary components of the two complex material parameters. We calculate the standard Type-A uncertainty in the fitting by [61]:

$$s_{y_i}=\sqrt{diag_i\left(\frac{\chi^2}{DOF}[J^TJ]^{-1}\right)}, \tag{10}$$

where s_{y_i} is the standard type-A uncertainty of component y_i, χ^2 is the sum of the squared residuals of the fitting, DOF is the degrees of freedom in the system, in this case four, and J is the eight by

four Jacobian matrix representing the sensitivities of the S-parameters to changes in the material properties. We now combine the Type-A and Type-B uncertainties by adding their variances:

$$u_{y_i} = \sqrt{\Delta y_i{}^2 + s_{y_i}{}^2}, \tag{11}$$

where u_{y_i} is the total uncertainty in component y_i.

The implicit derivative technique of [55] is carried over to formulate the uncertainty for the short method. We maintain independence between S_{11s}, the total reflection coefficient for the shorted sample, and S_{21}, the total transmission for the two-port measurement, so we can still write

$$\left(\frac{\partial S_{11s}}{\partial z}\frac{\partial z}{\partial \varepsilon_r} + \frac{\partial S_{11s}}{\partial \Gamma}\frac{\partial \Gamma}{\partial \varepsilon_r}\right)\frac{\partial \varepsilon_r}{\partial |S_{11s}|} + \left(\frac{\partial S_{11s}}{\partial z}\frac{\partial z}{\partial \mu_r} + \frac{\partial S_{11s}}{\partial \Gamma}\frac{\partial \Gamma}{\partial \mu_r}\right)\frac{\partial \mu_r}{\partial |S_{11s}|} = \exp(\angle S_{11s} j), \tag{12}$$

and,

$$\left(\frac{\partial S_{11s}}{\partial z}\frac{\partial z}{\partial \varepsilon_r} + \frac{\partial S_{11s}}{\partial \Gamma}\frac{\partial \Gamma}{\partial \varepsilon_r}\right)\frac{\partial \varepsilon_r}{\partial |S_{21}|} + \left(\frac{\partial S_{11s}}{\partial z}\frac{\partial z}{\partial \mu_r} + \frac{\partial S_{11s}}{\partial \Gamma}\frac{\partial \Gamma}{\partial \mu_r}\right)\frac{\partial \mu_r}{\partial |S_{21}|} = 0, \tag{13}$$

where j is the imaginary unit. All of the partial derivative terms given in [55] remain the same with the exception of $\frac{\partial S_{11s}}{\partial z}$ and $\frac{\partial S_{11s}}{\partial \Gamma}$, which are now given by

$$\frac{\partial S_{11s}}{\partial z} = \frac{2z(\Gamma^2 - 1)}{(1 - \Gamma z^2)^2} \tag{14}$$

and

$$\frac{\partial S_{11s}}{\partial \Gamma} = \frac{(1 - z^4)}{(1 - \Gamma z^2)^2}. \tag{15}$$

All other instances of S_{11} can simply be replaced with S_{11s}. We use the same formulation (9) to calculate the total uncertainty except that now the seven x_j become: $|S_{11s}|$, $\angle S_{11s}$, $|S_{21}|$, $\angle S_{21}$, $|S_{12}|$, $\angle S_{12}$ and L. The Type-A uncertainty calculation also remains the same as (10), but there are now two degrees of freedom, and the Jacobian is a six by four matrix. The reduction in the degrees of freedom by changing to the new method causes a slight increase in the type-A fitting uncertainty but this is dwarfed by the considerable decrease in Type-B uncertainty of this method.

c. Measurement Setup

The S-parameters are measured with a network analyzer calibrated in the WR-42 waveguide band (18 to 26.5 GHz) with the multiline thru-reflect-line (M-TRL) method with two line lengths. The calibration standard and sample measurements are processed externally from the network analyzer with a NIST-developed software called the Microwave Uncertainty Framework (MUF) [62][63].

The MUF calibrates the sample measurements and also calculates standard uncertainties for the S-parameters, such as those used in (9). The S-parameter uncertainties are based on the physical length and electrical uncertainty associated with each of the calibration standards, as well as uncertainty of the calibration reference plane position. The manufacturer-quoted network analyzer uncertainty is additionally considered in the total S-parameter uncertainty. The MUF processes repeat measurements allowing uncertainty estimates to include connector reproducibility, environmental factors, and any other repeatability considerations. We measure the low-loss Stycast 2850 FT epoxy with 23 LV catalyst that has been cast into a WR-42 waveguide shim, and Emerson & Cuming CR114 microwave absorber material cast in a similar fashion.

The four calibration standards are measured prior to the samples and then the samples are measured first in the two-port configuration, the short is then added in place of the port two connector, and S_{11} is measured again with the short-circuited samples. Both the epoxy and microwave absorber samples are cast into gold-plated WR42 waveguide shims with measured lengths of 3.598±0.0024 mm and 3.774±0.0015 mm respectively. This measurement process is repeated three times over the course of a few days. Figure 23 shows the experimental measurement setup.

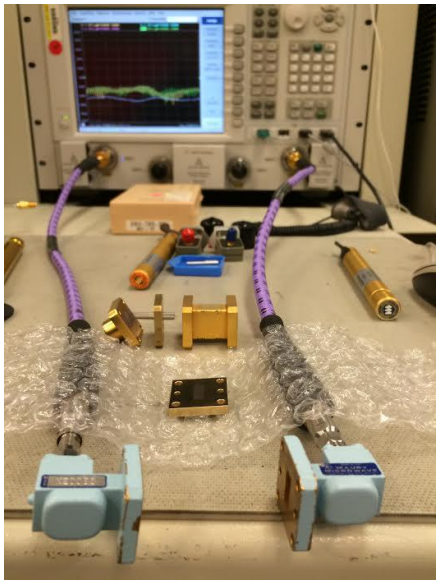

Figure 23: Photograph of measurement setup. From foreground to background; waveguide adapter ports, cast sample, calibration standards, and network analyzer

d. Experimental Results

The measurement results for the S-parameters (Figure 24-Figure 27) show the larger uncertainty in S_{11} than in S_{21} for the standard two-port measurement. Figure 24 in particular shows the drop in the magnitude of S_{11} and rise in uncertainty at the half-wavelength resonance frequency, around 19.7 GHz. We also see the large uncertainty in the phase of S_{11}. The uncertainty in the magnitude and phase of S_{11s}, with the short technique, are considerably smaller at the two-port resonance frequency seen in comparing Figure 24 and Figure 25. This is the principal cause of the uncertainty improvement offered by this method. We processed these data with the classical NRW technique, the standard Baker-Jarvis iterative method and the newly-developed short-circuit technique (see Figure 28, Figure 29). The epoxy sample is a relatively low-loss material, highly affected by the half-wavelength resonance. The microwave absorber is a higher-loss iron-loaded epoxy material that is less affected by the half-wavelength resonance, but exemplifies another potential issue with the Baker-Jarvis and NRW methods that will be discussed in the following subsections. Figure 28 and Figure 29 compare the complex permittivity and permeability results for the different methods and show the uncertainties.

Certain combinations of imaginary permittivity and permeability in a sample material, along with enough error in S_{11} will cause the solution to become non-physical, and result in a negative imaginary permittivity. The Baker-Jarvis method can constrain the parameters to physical values, but all of the loss can end up in the imaginary permeability instead, leaving the

imaginary permittivity at zero, as these parameters are highly anti-correlated. Nevertheless, we have demonstrated a good agreement between the short method and the Baker-Jarvis method for low loss material, in particular the real part of the permittivity and permeability, as shown in Figure 28. For the relatively lossy material, a clear difference is evident. We see a value of zero for the imaginary permittivity using the Baker-Jarvis technique, and a negative imaginary permittivity using the NRW. The uncertainty is also quite large for this parameter. The modified short-method provides a positive physical solution with a relatively smaller uncertainty.

For the absorber material with relatively large ε'', neither NRW nor BJ methods have success in adequately solving ε''. As we can see from Figure 29, NRW tends to generate a nonphysical parameter (negative ε'') and BJ enforces a lower bound to the fitting outcome, which essentially generates ε'' at a fixed value of zero. From our analysis, the underestimate of ε'' leads to an underestimate of ε' and an overestimate of μ''. This is in accordance with our observation from the fitting comparison in Figure 29. We believe the short method does not suffer this limitation and consequently provides more reliable results. As a result, we conclude that the pronounced disparity in ε' value among different methods is due to the limitation in NRW and BJ methods.

For the low-loss epoxy sample, the half-wavelength resonance is occurring at about 19.7 GHz, corresponding to $n = 1$ in $\left(n\frac{\lambda_g}{2}\right)$. We see that the Baker-Jarvis method is somewhat less affected by the half-wavelength resonance than the NRW, but the uncertainties in this vicinity are large. We see the anti-correlation of the imaginary terms when the ε'' term suddenly drops to zero at 19.4 GHz and the μ'' term jumps to non-zero. With this sample being pure epoxy, we don't expect to see any considerable magnetic loss, so this jump in the imaginary permeability is likely a numerical artifact. The short-circuit method smooths the imaginary terms and maintains relatively constant values with considerably smaller uncertainty than the standard iterative method. The average standard uncertainties across the WR-42 band for the short method were; 0.059, 0.049, 0.013, and 0.011 compared to the values for the NIST iterative method; 0.061, 0.067, 0.022, 0.019, for $\varepsilon', \varepsilon'', \mu', \mu''$ respectively. We see a reduction in average uncertainty across the band for all four material parameters most significant in the imaginary terms.

For the lossy absorber sample, we see that the NRW has arrived at a non-physical solution for the dielectric loss. The Baker-Jarvis method also seems to be affected by this negative root though the bounds on the fitting force the imaginary permittivity to a non-negative value, zero in

this case. The analytical uncertainty calculation assumes that the nominal solution is close to the 'true' value and evaluates the partial derivatives at the nominal solution value. This treatment of uncertainty does not account for the possibility of arriving at the incorrect local minima in the fitting procedure. The short method provides physical values for material parameters with relatively small uncertainties. We expect the ferrite-loaded absorber sample to exhibit both dielectric and magnetic losses, so the short method provides a more realistic solution.

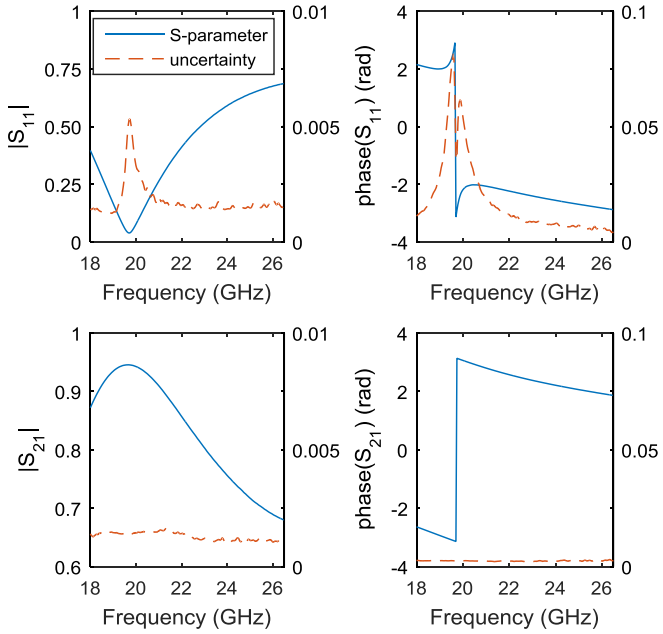

Figure 24: 2-port scattering parameter results (blue, left axis) and standard uncertainty (orange, right axis) for epoxy sample.

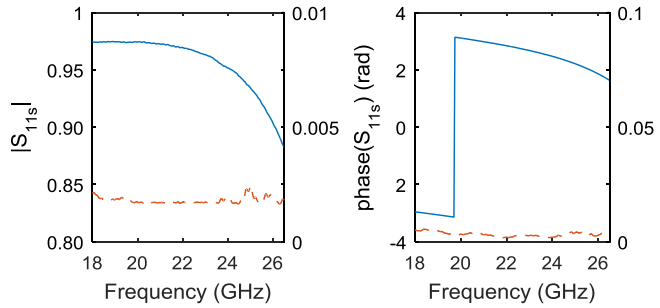

Figure 25: Short-circuited sample scattering parameter results (blue, left axis) and standard uncertainty (orange, right axis) for epoxy sample.

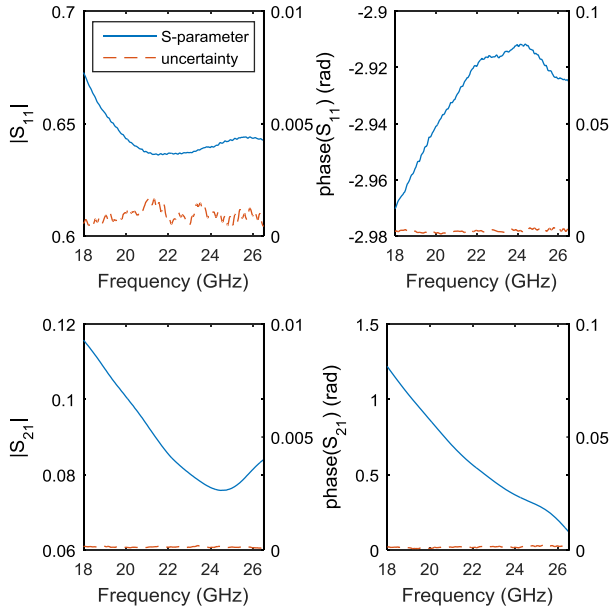

Figure 26: 2-port scattering parameter results (blue, left axis) and standard uncertainty (orange, right axis) for microwave absorber sample.

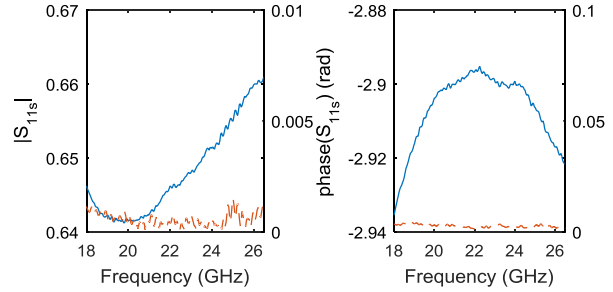

Figure 27: Short-circuited sample scattering parameter results (blue, left axis) and standard uncertainty (orange, right axis) for microwave absorber

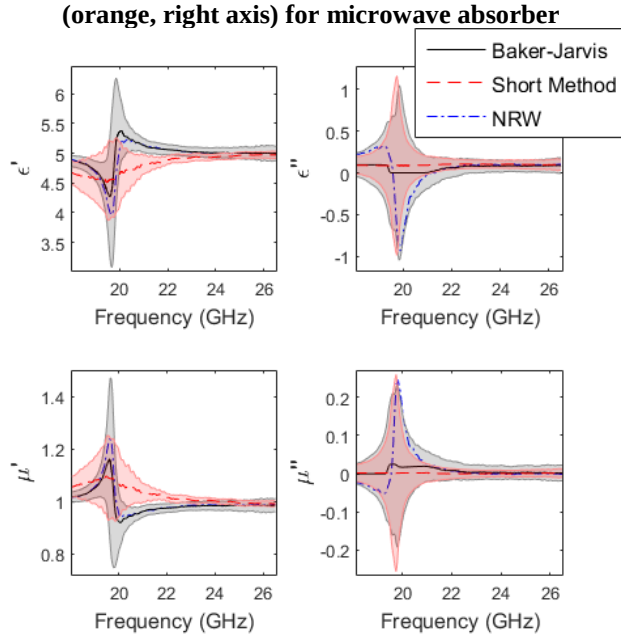

Figure 28: Comparison of extracted material parameters for epoxy-loaded sample using; Nicolson-Ross-Weir (NRW), Baker-Jarvis, and the new short-circuit method. Three standard uncertainties are plotted in shaded colors for the Baker-Jarvis and short

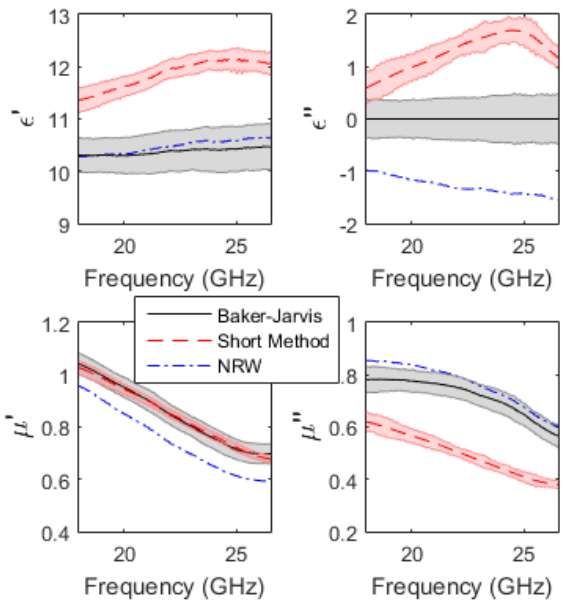

Figure 29: Comparison of extracted material parameters for microwave absorber-loaded sample using; Nicolson-Ross-Weir (NRW), Baker-Jarvis, and the new short-circuit method. Three standard uncertainties are plotted in shaded colors for the Baker-Jarvis and short

e. Simulated Material Samples

In order to compare the calculated material parameters to some 'true' value we create a frequency-independent material sample and model it in commercial finite element electromagnetics software. We model the same sample length as the epoxy sample, 3.598 mm, and chose the mean extracted material parameter values of the epoxy-loaded sample. The properties are defined as; $\varepsilon_r = 4.95 - 0.09j$ and $\mu_r = 1.025 - 0.085j$. The finite element simulation predicts the half-wavelength resonance when the mesh is sufficiently dense for convergence. Both the two-port and shorted-sample one-port S-parameters are simulated. We take these simulated S-parameters as the inputs to the material parameter algorithms. The S-parameter uncertainties associated with simulated values are difficult to derive accurately and are small compared to the measured values based on the convergence criteria, so the uncertainty analysis is omitted for the following discussion. We look only at the nominal values obtained with the Baker-Jarvis method and the modified short-circuit method.

Figure 30 shows the material parameter results for this simulated material. All four real and imaginary components of the material parameters for the short method are much closer to the 'true' values, compared to the classic Baker-Jarvis technique except for the real parts at the point of inflection of the resonance where they cross the true value. The imaginary components of the material properties are affected by the anti-correlation in the Baker-Jarvis iterative technique. We

see similar behavior to Figure 28 where the imaginary terms make opposite jumps near the resonance frequency around 19.7 GHz. The direction of the resonance spikes in the real terms are opposite between the simulated and measured solution which again shows the strong anti-correlation between these parameters. The short method shows accurate retrieval of the imaginary terms in the whole band. The $n = 1$ resonance of $\left(n + \frac{1}{2}\right)\frac{\lambda_g}{2}$ for the shorted sample measurement occurs out of the WR42 band and will occur at about 28.5 GHz, as calculated from extrapolated material properties.

The persistent underestimation of the real permittivity and overestimation of the real permeability appears to be a systematic artifact and is discussed further in the following subsections.

The FEM 3D geometry contained finite air gaps between the excited wave port and the material sample, necessary to model the interface of air to material. This type of air gap uncertainty is handled in the experimental results as a reference plane position uncertainty in the MUF. Three gap sizes were simulated and shown in Figure 30 with thicknesses; 0.0254 mm (0.001 in), 0.0172 mm (0.0005 in), and 0.00635 mm (0.00025 in). To be consistent, we also added the same finite air gap between the short and the sample. We found that a large portion of the disagreement between 'true' and simulated material parameters resulted from these air gaps. A small but less significant contribution also comes from using copper instead of ideal conductors for waveguide walls and short, as is assumed in the single-mode waveguide theory. It was found that the convergence error of S-parameters had an insignificant contribution to the measured versus true value discrepancy. The initial mesh in the software, of approximately 3000 nodes was dense enough to accurately solve the S-parameters. As the air gap in the model decreases, the effect of the resonance decreases, but the short method is less sensitive to this air gap than the Baker-Jarvis iterative method, and overall provides a more accurate result. The short method shows its strength particularly in retrieving the imaginary parts of the two material properties, with little sensitivity to both the air gaps between calibration plane and sample, and the sample and short.

When discontinuities from the half-wavelength resonance are seen in material property extraction, a smoothing fit is often applied, such as a Debye fitting [52] for dielectrics. If the material properties are highly frequency dependent, the Debye model may not provide enough poles to accurately represent complex behavior or the resonance may have enough broadband

effect to bias the smoothed result. The short method provides a measurement-based, frequency independent, smooth result without requiring any additional fitting or assumptions.

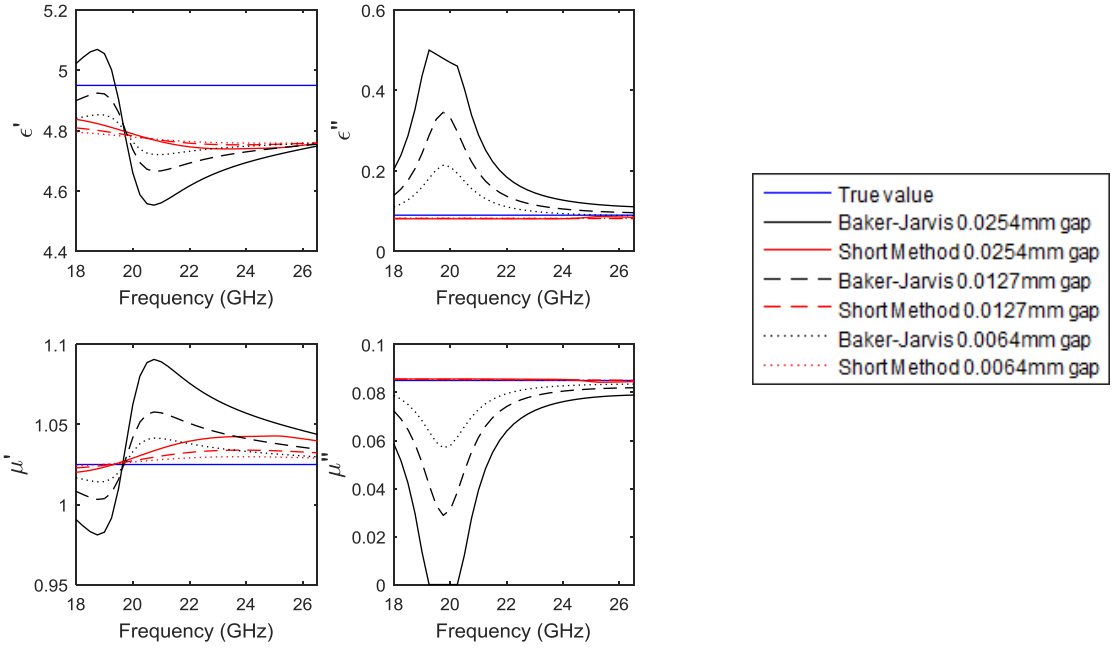

Figure 30: Comparison of extracted material parameters for simulated fictional sample: Baker-Jarvis, and the new short-circuit method. Extraction results for different simulated air gap lengths on either side of the sample are shown.

f. Discussion

Electromagnetic material properties are needed for design, simulation, and any kind of engineering use of electromagnetic systems. Communications, defense, medical, and environmental remote sensing are just a few of the many industries invested in microwave-related development and design. Easy and accurate characterization of permittivity and permeability, along with rigorous uncertainty analysis, allows for efficient design and minimizes prototyping and testing expenses by expanding the capability of simulation. Many modern applications are trending towards on-wafer microwave circuits and CPW transmission lines. The method discussed in this section could be readily adapted for on-wafer use such as in the setup described in [64] and [65].

The method discussed here resolves two of the main difficulties in making measurements of complex permittivity and permeability. The first of these is the mitigation of the half-wavelength resonance effect that can plague the material parameter solution for low-loss materials.

By omitting the S_{11} result of the standard two-port network analyzer measurement and replacing it with a one-port S_{11} measurement of the sample terminated by a reflecting short, we eliminate the highest uncertainty terms. The S-parameter uncertainties directly propagate into all four components of the complex electromagnetic material properties, and these uncertainties are considerably higher at and in the vicinity of a resonance frequency for the two-port S_{11}. We have decreased the uncertainty in the S-parameters by using an independent short-circuited measurement and analytical expression in addition to the retained S_{21} and S_{12} measurements from the two-port measurement.

The second main benefit of the proposed method is its robustness in avoiding the wrong root of the implicit model. The non-linear least-squares method involved in the original iterative method can occasionally land on a solution in which the optimal value would be nonphysical, but because the output is bounded to physical, positive values the algorithm rests on the boundary of the function range at zero. This non-physical root may provide a smaller value of the objective function of the fitting even when forced to zero. This can happen even if the initial value given to the fitting algorithm is close to and above the physically viable solution, because of the error in S_{11}. The short-circuit method has shown to maintain the correct physical root of the implicit physical model. This increase in robustness over the traditional NIST iterative method is due to the smaller S_{11} measurement error, and the newly-formulated physical model.

In the experimental results, the short method appears to produce a lower real part of the permittivity and larger real part of permeability compared to the NRW and Baker-Jarvis iterative method. The uncertainty sensitivities of the real parts are dominant with respect to the magnitude of S_{11} and S_{22} in the iterative method and S_{11s} in the short method. Because the theoretical calculation of S_{11s} is highly dependent on the short having a reflection magnitude of one, any deviation from this will cause bias in the retrieved result. A way to minimize this bias would be to perform a one-port calibration on the network analyzer prior to the one-port measurement instead of relying on the two-port calibration. The results for the imaginary parts of permittivity and permeability are much smoother than for the iterative method, likely a result of the method's inherent lower sensitivity to the phase of S_{11s} compared to S_{11} and the lower overall phase uncertainty in the frequencies investigated.

The method introduced here makes its largest impact for low-loss materials when both complex permeability and permittivity are unknown. The short-circuit method can easily be used in parallel with the classic technique as the data required to solve the classic method will likely be

saved along with the transmission measurements. The short-circuit method only requires one additional measurement, and the short is likely already on hand as a calibration standard. These convenient details make the method easy and quite practical in any real world application.

ii. Measuring Carbonyl Loaded Epoxy

Material samples were mixed and cast into waveguide sections with CBI loading percentages of 0, 5, 10, 20, 30, and 50 percent by tap volume. Waveguide samples in K-band (WR-42) and Ka-band (WR-28) were measured for all concentrations except 10 percent was only measured in WR-42. The two-port scattering parameters of the samples were measured on a network analyzer calibrated with the multi-line through, reflect, line (MTRL) method. The calibration was performed in the respective waveguide band at the flanges of two coaxial to waveguide adapters. The complex permittivity and permeability were determined using the NIST iterative technique [51]. As discussed at length in the previous section *i*, the low-loss unloaded (0% CBI) epoxy samples exhibited a half-wavelength resonance affecting the extraction so the modified method [53] was used instead.

It was initially assumed that the lowest frequencies would be the design constraint for the blackbody where the absorber thickness is thin relative to wavelength. This assumption proved incorrect, as discussed in the following section, but this was the motivation behind only measuring K-band and Ka-band waveguide samples. In order to facilitate design and simulation above 40 GHz, free-space measurements were conducted at the Institute of Applied Physics (IAP) at the University of Bern in W-band (75 GHz – 110 GHz), D-band (90 GHz – 140 GHz), G-band (140 GHz to 220 GHz), Y-band (350 GHz – 420 GHz) and between 560 GHz and 620 GHz. The 30 and 50 percent CBI loading samples were only additionally measured at W-band. The 0, 5, and 20 percent CBI loading samples at D-band and above used a slightly different variant of CBI, called ES as opposed to the EW-I in the other samples. The difference in material properties due to this difference were assumed small but will be investigated in the future. Figure 31 shows a picture of the samples that were measured for design purposes. Figure 32 and Figure 33 show the measured electromagnetic material parameters along with the uncertainties as calculated according to [55]. We see good agreement at the waveguide band crossover for most samples and parameters, with some steps seen in the real permittivity. We suspect that the offset seen for example in the 50% real permittivity is from sample variation. We could see a slight coloration change between the edges and center of some of the WR-28 waveguide samples.

A full set of 5% CBI and 50% CBI samples were cast in WR-42, WR-28, WR-22, WR-15, WR-10, WR-08, and WR-05. These samples were cast from the same absorber batch and at the same time as the absorber cone in order to confirm the repeatability of the material properties and monitor long-term degradation of the materials.

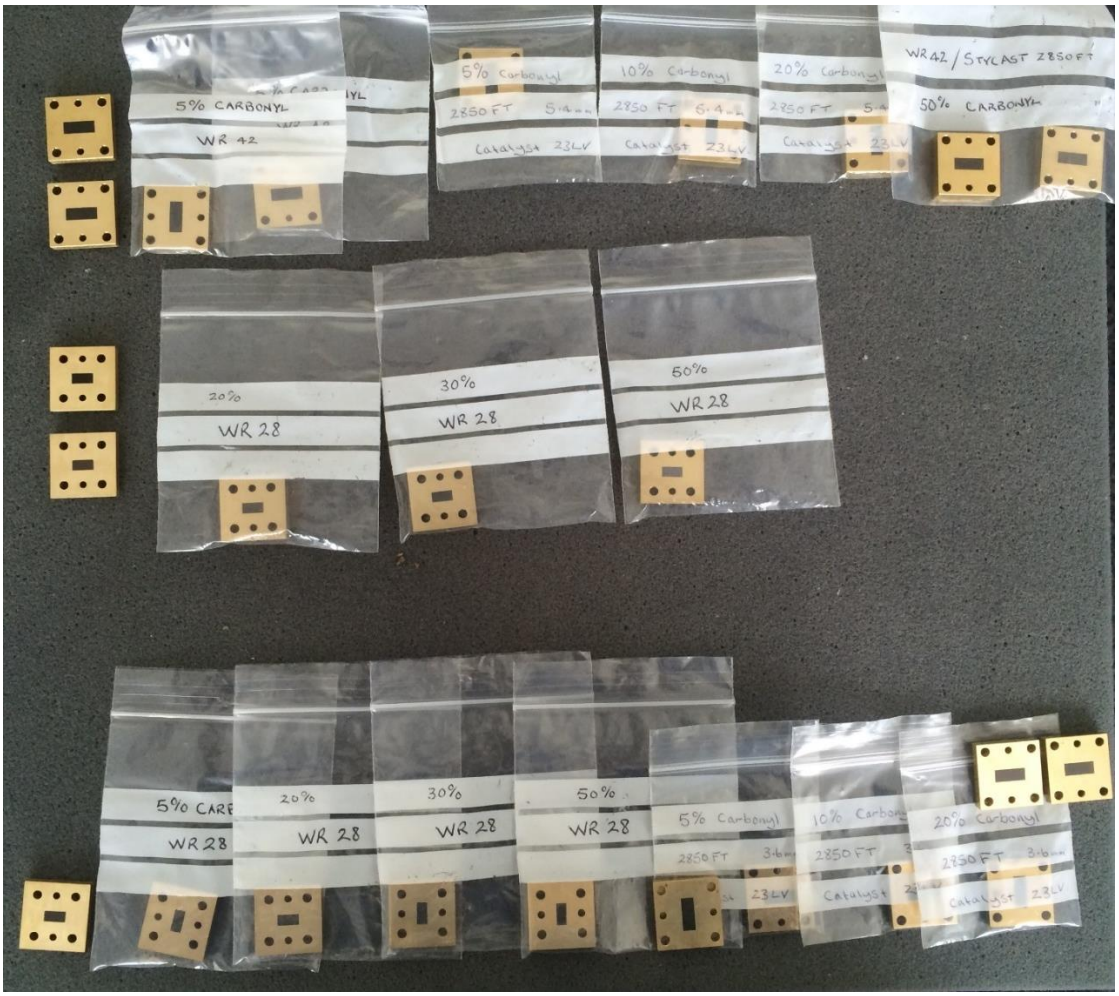

Figure 31: WR-42 and WR-28 waveguide shims loaded with varying concentrations of iron carbonyl powder

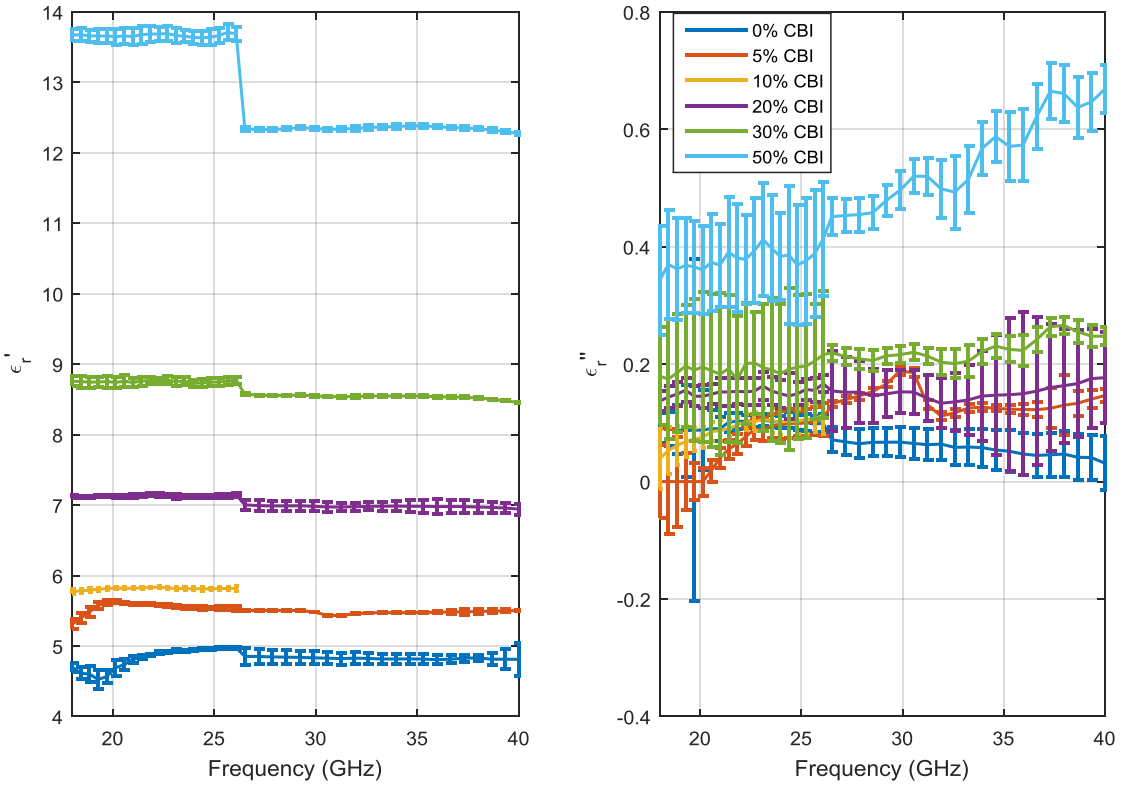

Figure 32: Plot of complex permittivity of Stycast 2850 FT 23 LV with variable carbonyl loading by volume

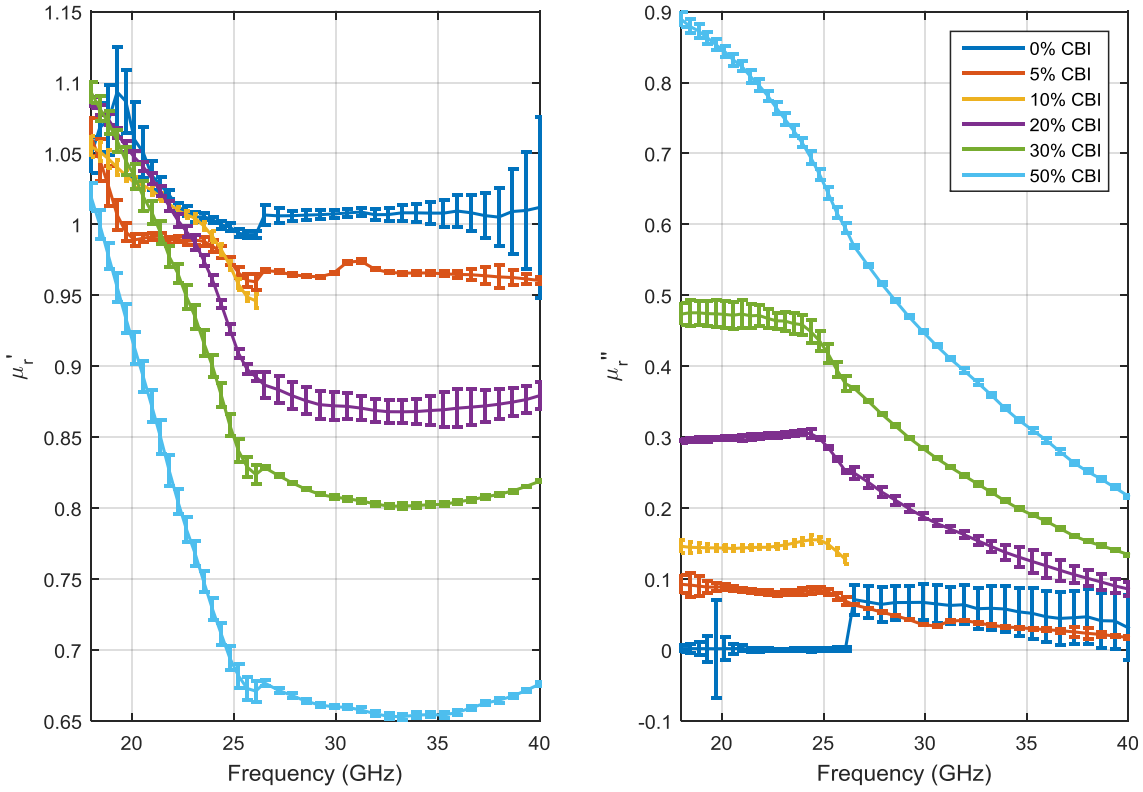

Figure 33: Plot of complex permeability of Stycast 2850 FT 23 LV with variable carbonyl loading by volume

Empirical fittings are applied to the complex permittivity and permeability quantities extracted from measurements to obtain continuous material property interpolations. Permittivity fittings are performed according to the formulations of Cole-Cole and Havriliak-Negami [66], shown in (16) and (17) respectively, and permeability is fit according to the Lorentzian model [66] given in (18);

$$\varepsilon(f) = \varepsilon_\infty + \frac{\varepsilon_s - \varepsilon_\infty}{1 + j\left(\frac{f}{f_r}\right)^{1-\alpha}}, \tag{16}$$

$$\varepsilon(f) = \varepsilon_\infty + \frac{\varepsilon_s - \varepsilon_\infty}{\left(1 + j\left(\frac{f}{f_r}\right)^{1-\alpha}\right)^{\beta}}, \tag{17}$$

$$\mu(f) = 1 + \frac{\mu_s - 1}{\left(1 + j\gamma\frac{f}{f_r} - \left(\frac{f}{f_r}\right)^2\right)^{k}}. \tag{18}$$

where ε_s and ε_∞ are the real static and infinite frequency permittivities respectively, μ_s is the static permeability, j is the imaginary unit, f_r is the resonance frequency, α, β, and k are fit parameters ranging between 0 and 1, γ is an empirical fit parameter. Figure 34 shows the measured and fit relative permittivity and relative permeability respectively. Table 3, Table 4, and Table 5 show the fitted parameters for Cole-Cole, Havriliak-Negami and Lorentzian models respectively.

Table 3: Fitting parameters for Cole-Cole fitting of CBI loaded Stycast

CBI % by vol.	ε_s	ε_∞	f_r (GHz)	α
0	4.97	4.61	1000	2.22e-14
5	5.61	4.38	1000	0.0649
20	7.17	5.61	527	0.1683
30	8.69	7.08	168	2.22e-14
50	13.13	10.37	85.6	2.22e-14

Table 4: Fitting parameters for Havriliak-Negami fitting of CBI loaded Stycast

CBI % by vol.	ε_s	ε_∞	f_r (GHz)	α	β
0	4.96	1.02	1000	2.26e-14	0.0890
5	5.62	1.00	1000	0.1519	0.2433
20	7.13	4.09	163	2.22e-14	0.1988
30	8.68	6.90	169	2.22e-14	0.8950
50	13.13	10.37	85.0	2.22e-14	1

Table 5: Fitting parameters for Lorentzian fitting of CBI loaded Stycast

CBI % by vol.	μ_s	f_r (GHz)	k	γ
0	1	N/A	1	0
5	8.77-4.0j	0.859	0.8112	11.26-26.94j
20	20.48-13.92j	0.829	0.7582	11.08-30.55j
30	42.62-27.22j	0.841	0.7954	12.90-29.55j
50	58.34-43.91j	0.801	0.7487	14.57-28.41j

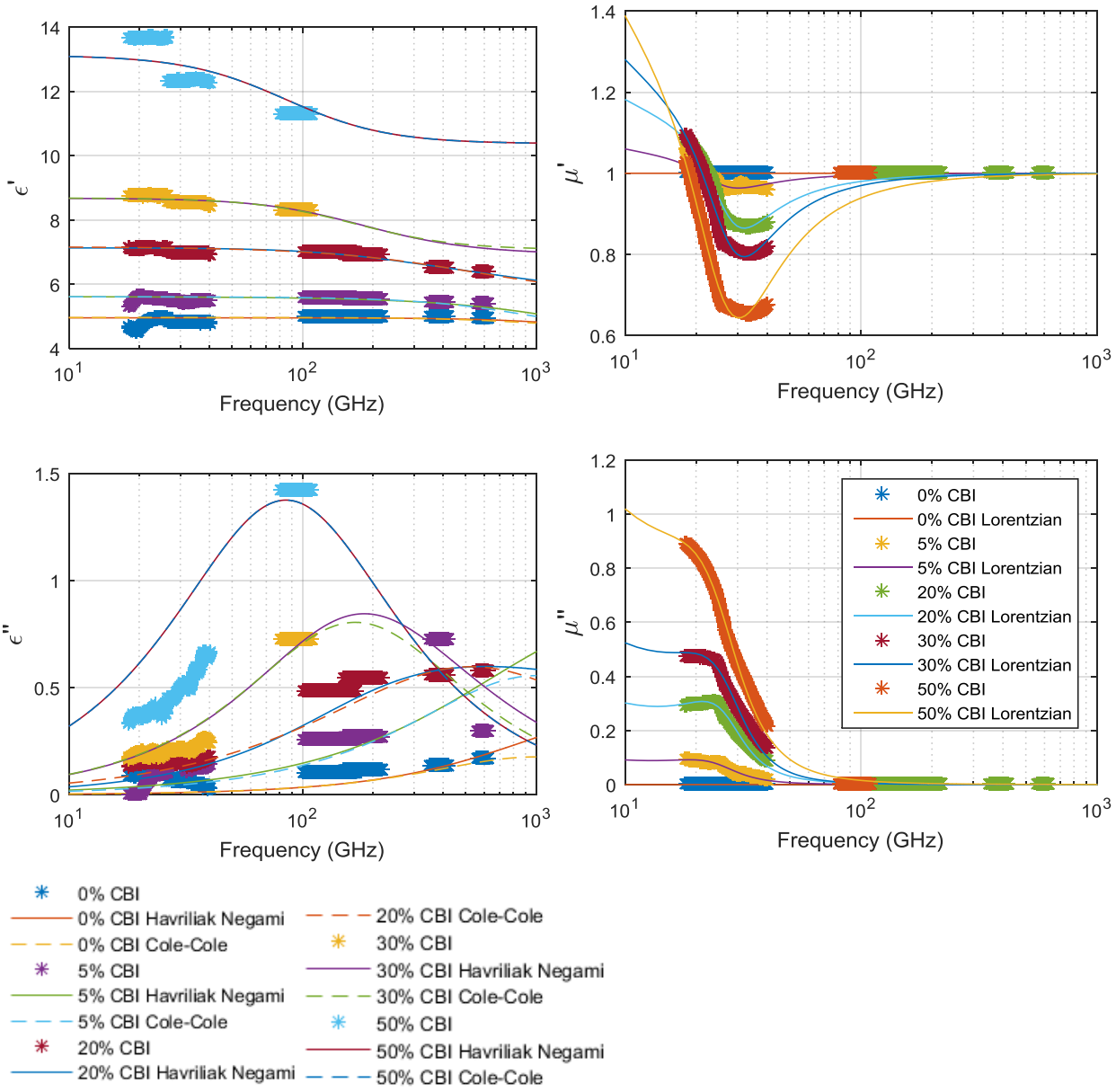

Figure 34: Measured and fitted complex relative permittivity and permeability

iii. Zotefoam insulation measurements

The thermal design determined that a thin layer of insulating foam on top of the low thermal conductivity absorber will reduce temperature gradients on the absorber surface and decrease brightness temperature uncertainty. A primary concern with putting a material in the free-space path between the source and receiver is reflection and attenuation of the thermal noise emitted from the blackbody source.

Using such a layer has been proposed and shown to have beneficial impact in [67] and we also learned that is was used with positive results in Ball Aerospace's calibration of GMI (GPM Microwave Imager). Closed-cell polyethylene foam was shown to have the lowest reflectivity, or best RF performance for a blackbody insulator. Typically, as the density of the foam increases the real permittivity also increases, a logical relationship as the lower density material has more air. The lowest density polyethylene is LD-15, referring to 15 kg/m^3. This low-density material has very little electromagnetic impact and is an excellent insulator, but we have the requirement of vacuum compatibility. We initially began the design assuming that HD-30 would be vacuum compatible, but were informed midway through the process, by external collaborators, that HD-60 is in fact the lowest density polyethylene foam that can stand up to repeated cycling in the vacuum chamber. We performed electromagnetic measurements of different densities of polyethylene foams in order to use the material data in the simulations.

Dielectric measurements were performed using a coaxial probe and waveguide-loaded samples. Both measurement techniques had their associated difficulties because of the easily compacted foam material. Cutting and loading the foam into a waveguide line was not straight forward due to difficulty cutting a perfect rectangular sample. If the sample became compressed the dielectric constant would be overestimated, and any airgaps would lead to poor extraction and an overall underestimation of the dielectric.

Figure 35 shows the coaxial probe results for real dielectric constant between 10 GHz and 50 GHz for various densities of polyethylene foam. The considerably higher values on the plot, near 1.2, result from a dense film layer discovered on some of the samples of HD-30. This film was caused from the manufacturing extrusion process and can be removed to lower the dielectric constant back to about 1.06. As stated previously, we were told by a colleague who had performed proprietary testing at Ball aerospace that the HD-60 or 60 kg/m^3 polyethylene material was the least dense material that survived repeated cycling in the thermal vacuum chamber. For this reason, HD-60 was chosen for use in the proceeding simulations. As discussed in the experimental

results only HD-80 was obtainable in white at the time of the purchase so this variant is used in the experimental testing and final product.

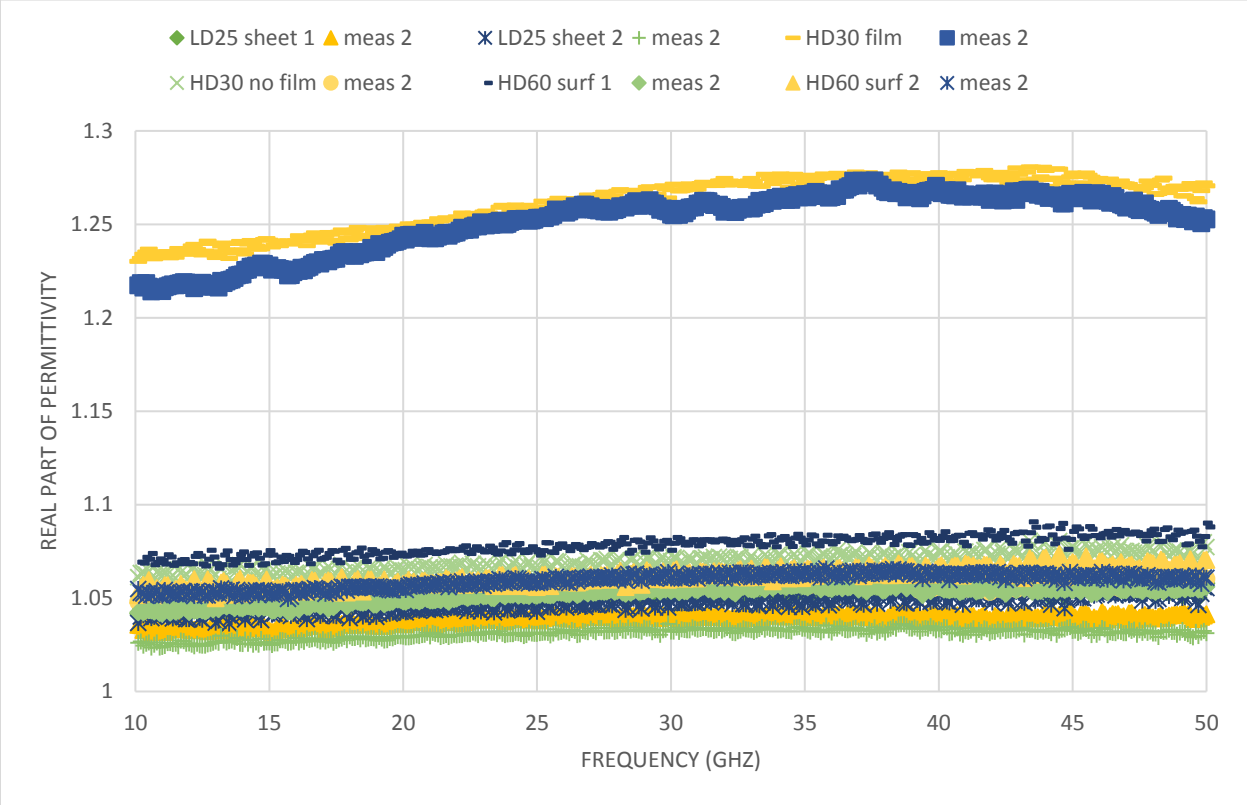

Figure 35: Coaxial probe results for dielectric constant of various densities of polyethylene foam materials

B. Cone Reflectance & Emissivity Modeling

Emissivity is the primary descriptor of how close a source is to radiating as an ideal blackbody. Microwave brightness temperature is defined based on the temperature of a blackbody; thus it is critical to maximize the emissivity of the source when calibrating brightness temperature. By conservation of energy and Kirchoff's law of reciprocity, a high emissivity 'blackbody' must have high absorptivity and thus very low reflectivity. Because the conical blackbody is backed with copper, we can safely assume that there is no transmittance. Emissivity as a function of elevation angle, θ, can then be defined relative to reflectance as [68],

$$\varepsilon(\theta) = 1 - \frac{\int_{\Omega_s=2\pi} |E_s(\theta,\Omega_s)|^2 r^2 \, d\Omega_s}{|E_i(\theta)|^2 A\cos(\theta)} \quad , \tag{19}$$

where E_i is the electric field strength of a plane wave incident on the blackbody, E_s is the electric field scattered off of the blackbody, r is distance, A is cross sectional area of the body, and Ω_s is the hemispherical solid angle over which the incident field is scattered. The differential term Ω_s is $sin(\theta_s)d\phi_s d\theta_s$ where θ_s and ϕ_s are the spherical coordinates of the scattering hemisphere in the coordinate system of the blackbody. The indices of θ_s are from 0 to $\pi/2$ and ϕ_s from 0 to 2π.

i. Geometric optics

The high-frequency approximation geometric optics (GO) or ray-tracing model was constructed as a quick, computationally inexpensive, first-order design approach. This method allows for a numerical optimization to minimize reflections by choosing an optimal combination or absorber types and thicknesses in the cone.

The number of 'bounces' experienced by a ray followed into the conical cross section can be expressed as [69],

$$M = \frac{180}{2\phi}, \tag{20}$$

where ϕ is the half-cone angle in degrees, and M is the number of bounces, to be rounded down to the nearest integer value. We assume a plane wave excitation such that the incident ray is parallel to the cone-axis. The angle of incidence in degrees for each subsequent bounce on the absorber layer can be described by the relation,

$$\alpha_i = 90 - i\phi \text{ for } i = 1,2,3 \ldots M, \tag{21}$$

where α_i is the angle of incidence for the ith bounce. Figure 36 provides a general drawing of the aforementioned geometry with the first two bounces shown.

The total reflection coefficient of each bounce is calculated from the oblique incidence Fresnel equations for layered magnetic and dielectric lossy materials following [70]. Maintaining the notation of [70] the total complex reflection coefficient for each bounce $\tilde{R}_{0,1}$ is calculated from the incidence angle, material properties and layer thickness. Figure 37 shows the geometry for a single bounce on the absorber structure, where N is the total number of layers in the absorber assembly, and the absorber is terminated with copper, approximated as a perfect electric conductor

(PEC). The total reflection for a given cone design is determined by the mean over polarizations of the squared product of reflection coefficients for individual bounces,

$$R_{total}{}^2(f,\phi,\boldsymbol{d},\boldsymbol{\varepsilon},\boldsymbol{\mu}) = \tfrac{1}{2}\sum_{pol}\left|\prod_{i=1}^{M}\tilde{R}_{0,1}{}^{pol}(\alpha_i,\boldsymbol{d},\boldsymbol{\varepsilon},\boldsymbol{\mu},f)\right|^2, \quad (22)$$

where R_{total} is the total reflectivity magnitude of the model, $\tilde{R}_{0,1}{}^{pol}$ is the total reflectivity for a single bounce on the multilayer absorber assembly of linear polarization pol ($pol = s,p$), $\boldsymbol{d}$ is the length N vector of layer thicknesses, $\boldsymbol{\varepsilon}$ is the vector of complex permittivities of the layers, $\boldsymbol{\mu}$ is the vector of complex permeabilities, and f is frequency. In order to determine the optimal absorber configuration, a nonlinear fitting algorithm is employed to minimize an objective function. The objective function to be minimized is defined as,

$$F(\phi,\boldsymbol{d},\boldsymbol{\varepsilon},\boldsymbol{\mu}) = \max(\{|R_{total}(f,\phi,\boldsymbol{d},\boldsymbol{\varepsilon},\boldsymbol{\mu})|: f \in f_{RS}\}) + \left|\sum_{i=1}^{N} d_i - d_{des}\right|, \quad (23)$$

where F is the scalar objective function value to be minimized, f_{RS} is the set of frequencies to be optimized over, and d_{des} is the desired total thickness of the absorber assembly. The second term on the right is a penalty term to ensure that the solution layer thicknesses sum to the desired total absorber thickness, determined by thermal requirements. As mentioned and discussed in section IV.C., a constraint imposed by thermal requirements is that the first layer consist of a 3 mm thick layer of closed-cell polyethylene foam similar to that described in [67]. An additional constraint on the absorber assembly was the 1 mm thick layer of pure epoxy (0% CBI loading) against the copper, or as layer N, required for mechanical stability of the freestanding absorber cone discussed in section IV.F.. We model the half-cone angle constrained to 10 degrees due to radius and length requirements, discussed in section III. The total absorber thicknesses examined were 7 mm and 8 mm, which includes the 3 mm polyethylene and 1 mm pure epoxy layer. This left 3 mm or 4 mm, respectively, to be optimized with CBI loaded lossy epoxy. For manufacturing practicality this corresponded to two individual absorber layers, or a total of 4 layers.

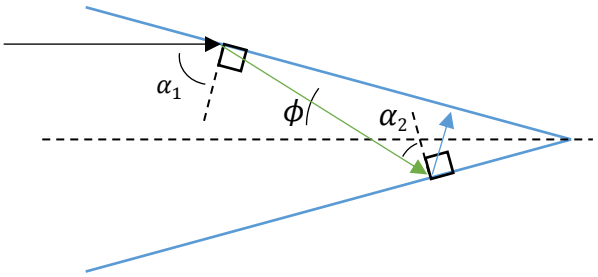

Figure 36: Sketch of geometric-optics geometry, first two bounces shown.

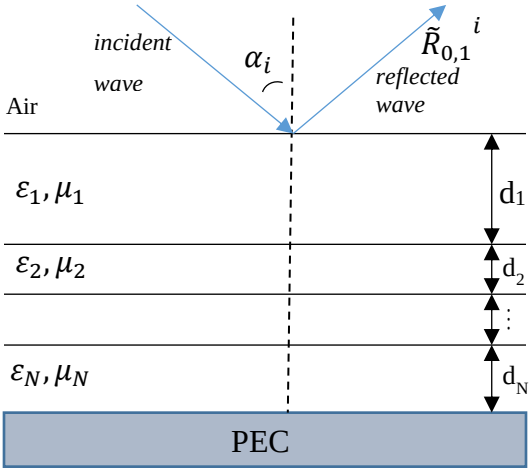

Figure 37: Sketch of a single oblique incidence bounce on the lossy, layered absorber surface

The possible absorber combinations of two absorber types are looped through and optimal thicknesses are determined from the non-linear fitting minimization (23). The minimum total reflectivity of the various combinations is taken to be the optimal absorber design. The algorithm was run using the following remote sensing-applicable frequencies for f_{RS} in GHz: 18, 19, 22, 23, 23.8, 31.4, 50, 50.3, 51.76, 52.8, 53.596, 57.29, 60, 88.2, 90, 118, 165.5, 183.31, and 220. The EM material properties from the fitting in section V.A.ii. are used for $\boldsymbol{\varepsilon}$ and $\boldsymbol{\mu}$. The permittivity of the HD-60 polyethylene foam, as discussed in section V.A.iii., was assigned a 'worst case' non-dispersive value of $\varepsilon_r = 1.08 - j1\text{e-}5$. Table 6 presents the two candidate optimal absorber assemblies.

Table 6: Optimized absorber types and thicknesses

Layer #	7 mm total	8 mm total
1	3 mm HD-60 Polyethylene Foam	
2	1.4 mm 5% CBI	1.8 mm 5% CBI
3	1.6 mm 50% CBI	2.2 mm 50% CBI
4	1 mm Stycast 2850 FT	
5	Copper (PEC)	

The optimal CBI loading percentages in both thickness cases are the same, both being 5% followed by 50%. This ordering follows what one might expect for a broadband absorber, providing a stepped gradient with the best matched, lowest dielectric, material closest to air and a more attenuating material deeper into the structure. Figure 38 shows the magnitude of the total reflectivity as calculated by (22) for the optimal configurations.

The optimized 7 mm total thickness structure does not provide adequate broadband reflectance for a high performance blackbody; we require less than -40 dB, roughly corresponding to emissivity >0.9999. The 8 mm total thickness design performs much better at critical remote sensing frequencies but does exhibit one peak above -40 dB at approximately 38 GHz. This small band of marginal performance will be tolerated, because further increasing the absorber thickness would have broadband thermal consequences, introducing greater temperature gradients in the absorber.

The effect of the polyethylene insulation layer is also presented in Figure 38. The model results are shown with and without the polyethylene foam because this was an easy comparison to make experimentally to confirm the predicted electromagnetic benefit of the foam. The polyethylene decreases the total reflectance slightly because it smooths and extends the EM impedance gradient from air to copper creating an improved impedance match.

The geometric optics technique has been shown to perform well against alternative simulation methods [71] but we wish to verify these results with a more exact solution method.

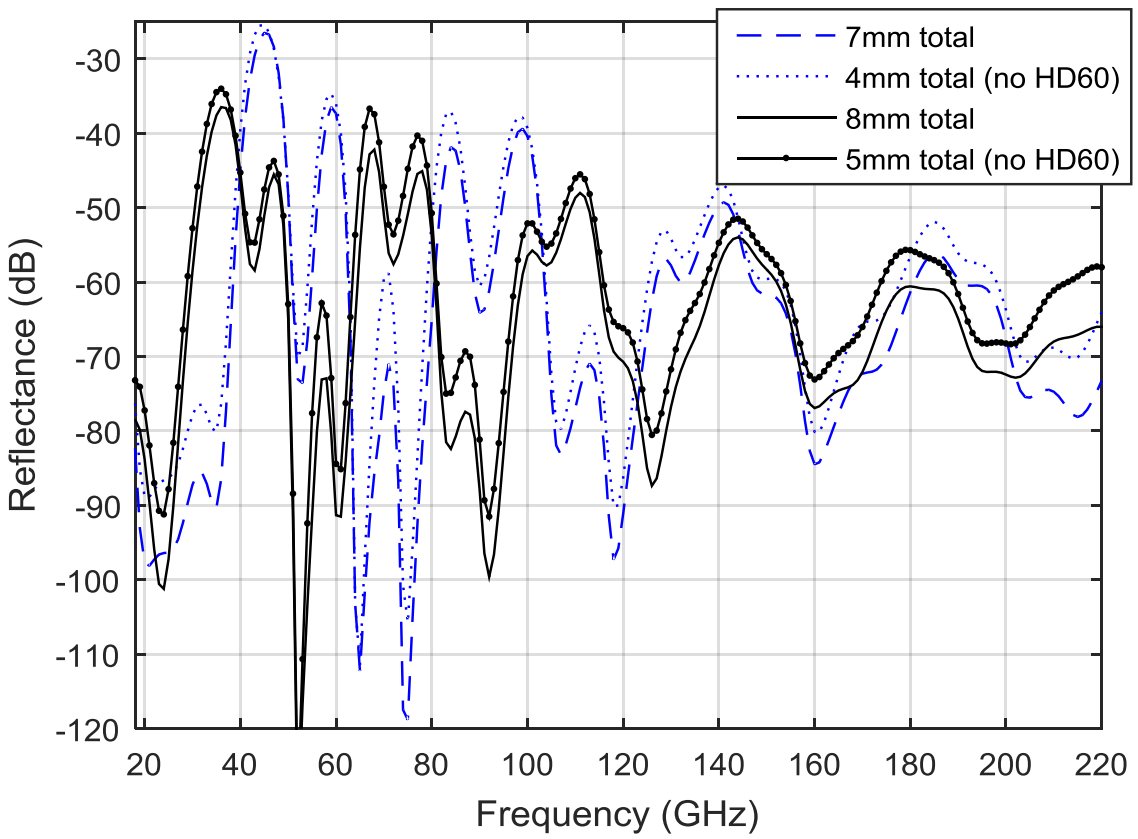

Figure 38: Plot of geometric optics calculated reflectance magnitude spectrum for optimized absorber assemblies with and without HD-60 insulation

ii. Finite element

A commercial EM simulation suite, ANSYS HFSS, is used to model and simulate the optimized conical blackbody design. The absorber and pure epoxy layers are modeled with a PEC backing boundary condition. The top layer of polyethylene foam insulation is also included as in section III. A. The dispersive, fitted, material properties discussed in section V.A. are input to the model. A visualization of the geometry and absorber layering structure as simulated in the FEM is provided in Figure 39.

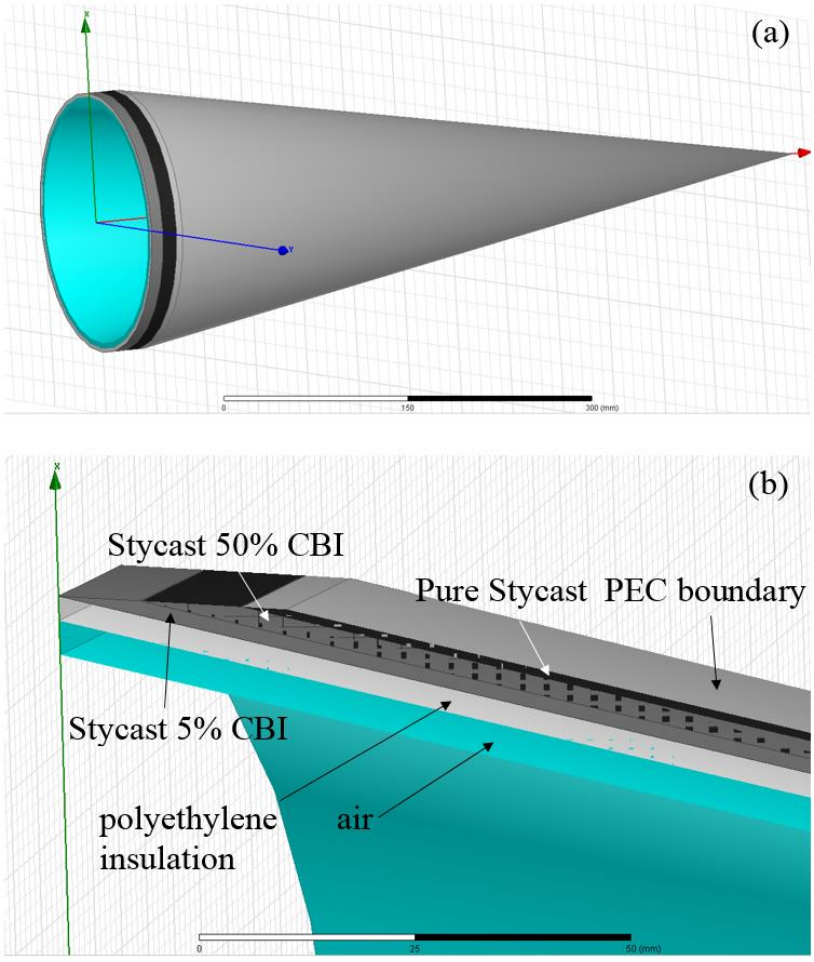

Figure 39: (a) Cone model in finite element software (b) zoomed perspective on layers

The air layer is λ/4 thick at 18 GHz, and the upper surface of the air section is defined as a 'finite element-boundary integral' hybrid boundary condition allowing the solver to use the method of moments in the air region inside the cone, minimizing the volume requiring finite element mesh. The model is excited with both a Gaussian beam of beam waist 36.2 mm and a uniform plane wave. The 3-dimensional cone model, having a radius of 108.5 mm, and a total thickness of 12.2 mm, is electrically large. This results in a large required mesh, and a computationally expensive simulation. The analysis is prescribed with custom convergence criteria, requiring the normal reflection magnitude to change no more than 1% (in dBs) between mesh adaption passes. The simulation is solved on a state-of-the-art, high-performance-computing cluster with 128 cores and 2TB RAM.

The simulation is solved at frequencies between 18 GHz and 60 GHz at 1 GHz steps for Gaussian beam excitation, and at discrete frequencies where convergence was obtained for plane

wave excitation at 18 GHz, 19 GHz, 22 GHz, and 23.8 GHz. The plane wave excitation requires more single-processor adaptive mesh passes to reach convergence, likely due to the higher relative power scattering from the edge of the cone aperture. This sharp 'knife edge' is a singularity point and requires fine mesh density. The plane wave solutions required up to 160 GB RAM and 9.5 total hours per frequency point, increasing with frequency, and the Gaussian beam solution required 180 GB and 2.5 hours per frequency point. The single-core adaptive mesh procedure caused the plane-wave model to solve considerably slower. Figure 40 shows the convergence of monostatic reflectance and the number of solved mesh nodes as a function of adaptive pass number.

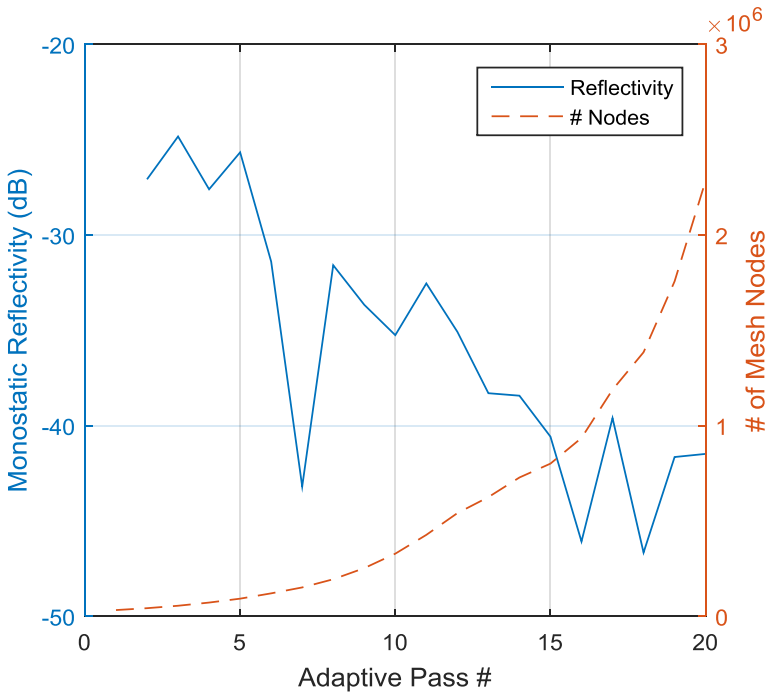

Figure 40: Convergence of monostatic reflectivity (left axis) and number of solved mesh elements (right axis) for plane wave excitation at 19 GHz as a function of the adaptive mesh pass

Full characterization of emissivity requires bi-static measurement of reflectance at a full spectrum of incidence angles, a four-dimensional product, integrated into the two-dimensional solid-angle dependent emissivity. This four-dimensional quantity has been referred to as the bidirectional reflectance distribution function (BRDF) in optical realms. Measuring this quantity experimentally is difficult but through simulation we can rather easily obtain this output. In addition to comparing normal monostatic reflectivity of simulated and experimental results we obtain hemispherical reflectance patterns and integrate the full analytical emissivity quantities.

Because of the circular symmetry of the cone, in spherical coordinates the dependence on angle ϕ can be eliminated. Note that the reflected field is a function of ϕ_r due to excitation polarization, but this is integrated out and the resulting emissivity is polarization independent. Following Kirchhoff's law of reciprocity and assuming no transmittance, due to PEC backing, emissivity is defined as [68],

$$\varepsilon(\theta) = 1 - R(\theta), \tag{22}$$

where ε is emissivity, R is the total integrated power reflectance defined as,

$$R(\theta) = \frac{\int_{\theta_r=0}^{\pi/2}\int_{\phi_r=0}^{2\pi} |E_r(\theta,\theta_r,\phi_r)|^2 r^2 \sin(\theta_r) d\phi_r d\theta_r}{P_i}, \tag{23}$$

where E_r is the reflected electric field, P_i is proportional to the incident power, r is the corresponding radius of the reflected field, ϕ_r and θ_r are the reflected field spherical coordinates, and θ is the incident angle of excitation. The analysis discussed herein is presented and described in equations 2.3.6 and 3.5.25 of [68]. When discussing plane wave excitation,

$$P_i = |E_i(\theta)|^2 A\cos(\theta) \tag{24}$$

where $E_i(\theta)$ is the incident electric field, A is the cross sectional area of the blackbody aperture and E_i is the incident EM field. Note we have cancelled the division by free-space impedance from both sides of (23) so P_i is in fact only proportional to power and has units of squared Volts. For the Gaussian beam excitation case we have [72],

$$P_i = \frac{1}{2}\pi|E_i(\theta)|^2 {w_0}^2 \tag{25}$$

where $E_i(\theta)$ is the maximum field strength, and w_0 is the beam waist. Again, this term is also proportional to power, normalized by free-space impedance. We also compute the reflectance assuming an isotropic radiator where the far field quantity $2\pi|E_r(0,0,0)|^2 r^2$ as $r \to \infty$ is used in the numerator of (23) instead of performing the full integration of the bidirectional distribution. A theoretically ideal blackbody is isotropic, but the conical geometry is designed to provide

directionally optimized absorbance. As shown in Figure 43, the normal integrated reflectivity or $R(0)$ does not perfectly agree or track with the isotropically assumed monostatic reflectivity. This is due to the non-isotropic and directionally dependent scattering of the conical cavity. The maximum of the reflectivity distribution is frequency and geometry dependent and does not necessarily occur at monostatic normal incidence ($\theta_r = 0$) but instead has a radiating pattern similar to that of an antenna. As shown in Figure 43 this explains why $R(0)$ cannot be predicted simply with knowledge of $E_r(0,0,0)$.

When a radiometer antenna is looking into the blackbody the range of θ over which the blackbody radiates into the antenna is a function of separation distance and radius of the blackbody,

$$\theta_{max} = tan^{-1}(\frac{r}{d}), \tag{26}$$

where θ_{max} is the maximum off-normal angle at which the cone radiates into the horn, and d is the separation distance. Figure 41 shows a drawing describing this geometry.

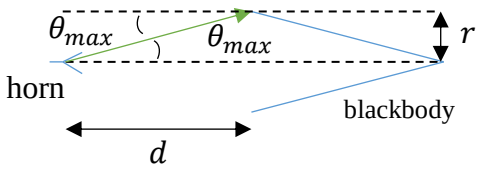

Figure 41: Diagram of geometry for analysis using far-field assumption

The FEM simulated reflectance as a function of θ for the conical target at 18, 19, 22, and 23.8 GHz with plane wave excitation are presented in Figure 42. We see that the peak in the reflectance function for the cone is not at $\theta = 0$ but instead varies as a function of frequency. This is preferable in order to reduce coupling between antenna and target and to attenuate any standing waves occurring between the two.

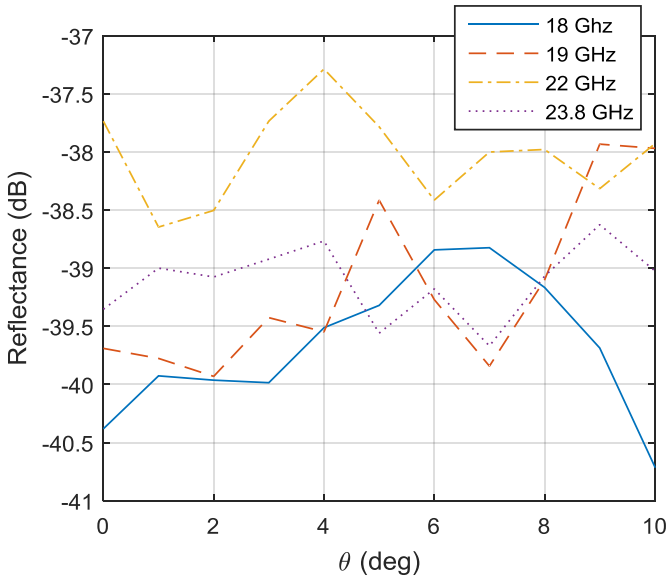

Figure 42: Integrated total reflectance of simulated blackbody with plane wave excitation at 18, 19, 22 and 23.8 GHz

The pattern of a horn antenna in the near-field will resemble something closer to a Gaussian beam than a plane-wave. For this comparison we excite the blackbody with a normal incident Gaussian beam of waist $w_0 = r/3$, where r is the cone radius. This ensures that the amount of spillover power is negligible (-78 dB).

The FEM results for both plane-wave and Gaussian excitations are shown in Figure 43 with both the isotropic assumption and full reflectance integration results shown. At present, there is no generally accepted way to quantify uncertainties from simulated results. We predicated our estimation on the convergence criteria in the simulation of the normal reflectivity $|E_r(0,0,0)|$ quantity. The estimated error bars represent 1% of this quantity in dB. These uncertainties are not propagated through the integration to total reflectance as we do not have an estimate of the uncertainty bounds of the solid angle dependent reflectivity.

The antenna power pattern determines the contribution of off-normal emissivity ($\theta \neq 0$) to a brightness temperature measurement. The boresight ($\theta = 0$) is typically the antenna gain maximum, but a monostatic normal incidence reflectivity measurement likely will not accurately quantify the emissivity at normal incidence due to the non-isotropic nature of the target geometry.

The differences between the isotropically-assumed reflectance and the 'true' integrated reflectance field shows the need for measurement of the BRDF. At smaller reflectances, the isotropic assumption is better at predicting the true reflectance, as seen in Figure 43. In a linear scale, the difference between -60 dB and -50 dB is an order of magnitude smaller than the

difference between about -40 dB and -30 dB. We conclude that using an approximately Gaussian beam excitation on the conical cavity will result in lower reflectance and higher effective-emissivity, and resemblance of the monostatic configuration to Gaussian beam excitation would, in practice, ensure a close approximation of true reflectance characterization.

The Gaussian beam excitation results also agree more closely with the geometric optics simulation than the plane wave excitation. Both the geometric optics and Gaussian excitations consider the bulk behavior of the cone while reflections from the plane wave excited simulation are somewhat disguised by the edge scattering and diffraction from the aperture.

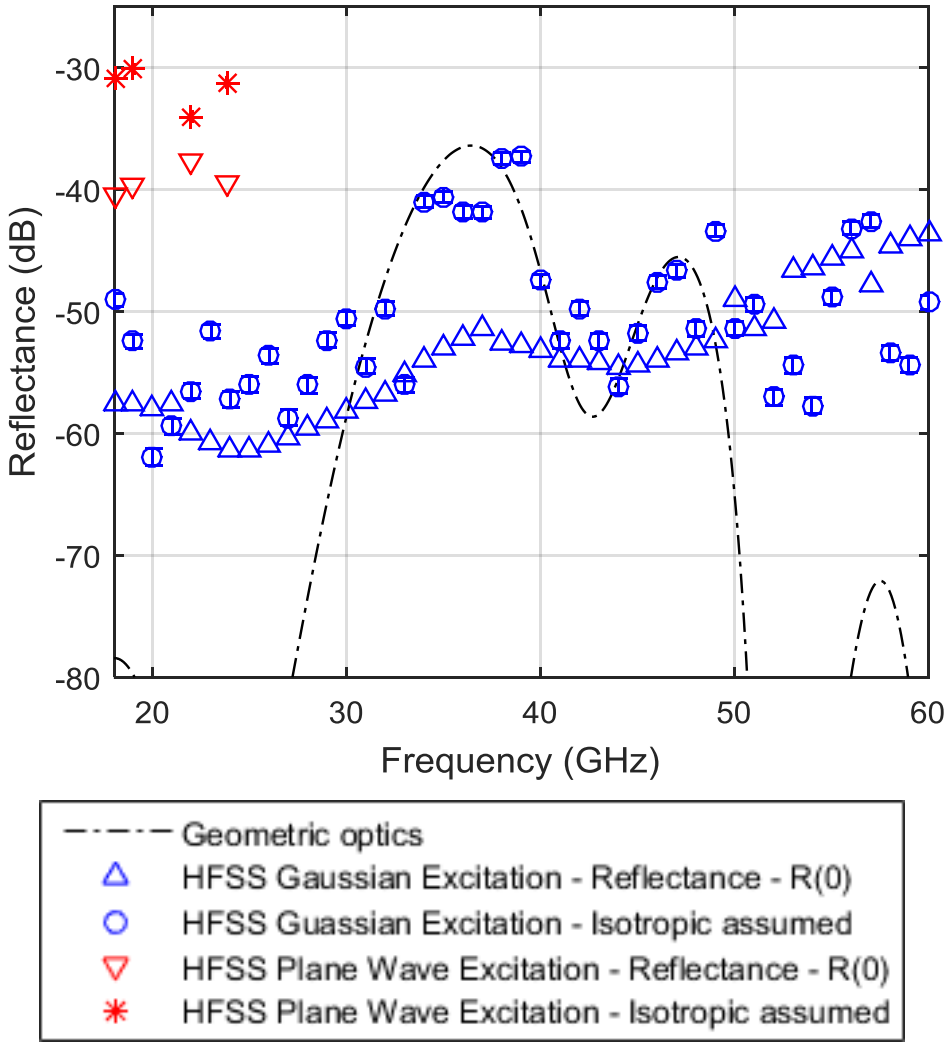

Figure 43: Finite element simulation results of integrated normal incidence reflectance. Geometric optics solution is also shown for comparison.

The finite element model results repeatedly showed higher reflectivity than the geometric optics model. It was hypothesized that numerical error became significant in the processing of the finite element results. When the finely stepped solid-angle dependent reflectance field is integrated in one degree increments in ϕ_r and θ_r, the resulting numerical 'noise floor' is relatively high. This 'noise floor' is shown to increase with frequency for a given mesh size. Figure 44 shows the reflected electric field in linear units plotted in a different color for each of the many reflection angles θ_r. The maximum at about 38 GHz as predicted from the GO model is apparent, but we also see the 'noise floor' and its increase with frequency. The mesh was adapted for 60 GHz Gaussian beam excitation and solved at 1 GHz steps between 18 GHz and 60 GHz. Figure 45 provides a different visual representation of the noise floor increasing with frequency, as you can see in general the color trend going from darker blue to lighter yellow from left to right.

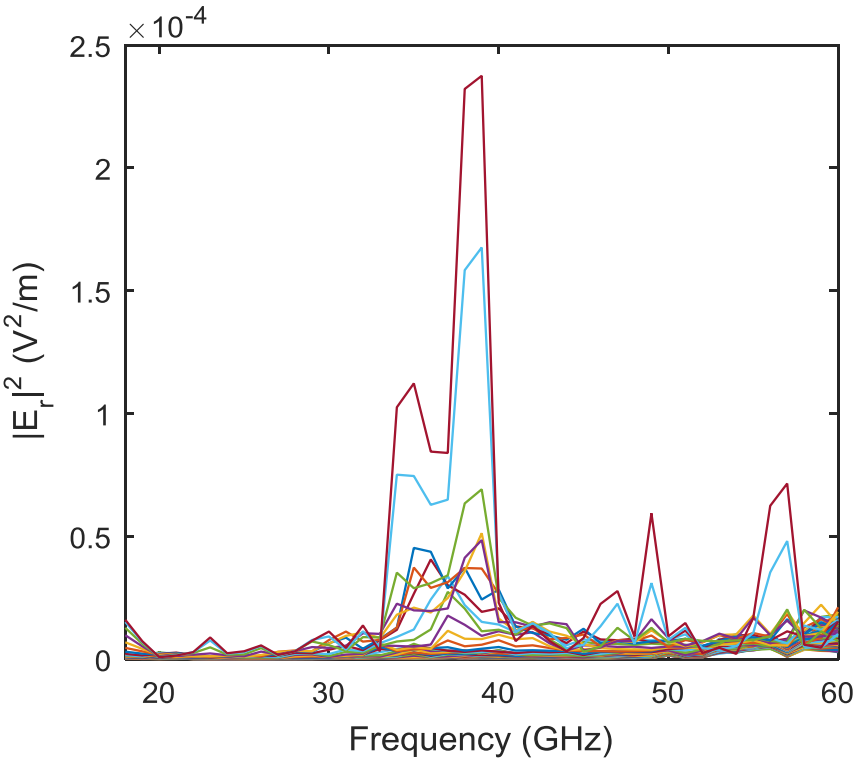

Figure 44: Squared reflected field magnitude from Gaussian field excitement in finite element model. Different color lines represent various reflection angles θ_r from 0 to 90 deg.

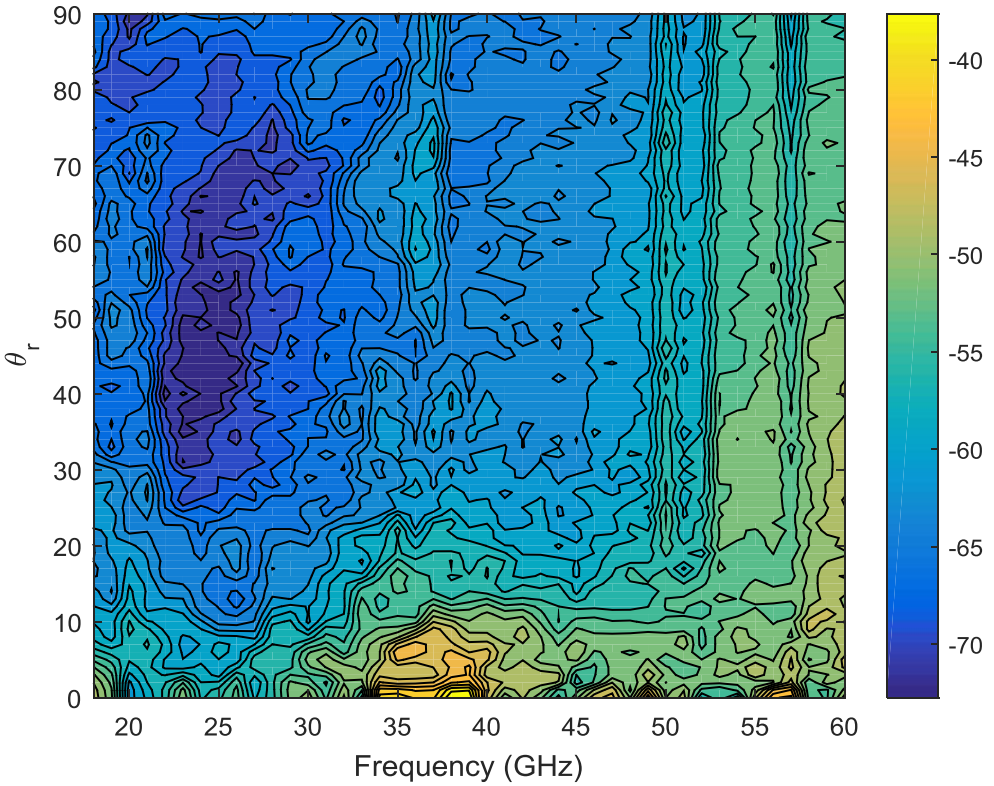

Figure 45: Alternate view of reflected field magnitude versus frequency and reflection angle θ_r

iii. Mode matching

In order to cross-check the GO and FEM methods, which were providing significantly different results, another full-wave modeling method was attempted. No meaningful results were extracted from this modeling attempt, but it is included here for completeness.

The idea behind this method was the use of analytical circular waveguide theory to model the absorber lined conical shape in small sections. By using theory for circular waveguide discontinuity junctions, it is possible to calculate the analytical scattering parameters from a junction between two different diameters of circular waveguide. The fractional power propagated through to the next waveguide section can then be formulated into modal form and the attenuation in the absorber lined circular waveguide section can be calculated. The transmission and reflection coefficients, S_{11} and S_{21} for each junction and straight section can be cascaded to result in the reflectivity of the full cone structure. By controlling the ratio between the difference in diameter in the discontinuity step and the length of the waveguide section, the appropriate cone angle can be modeled. The stratified geometry approaches the conical geometry in the limit as the number of junctions and straight sections goes to infinity.

The analytical solution for multi-layer dielectric lined circular waveguide sections has been determined [73][74][75]. The modified method discussed in [75] was chosen for determining the propagation constant in the dielectric lined circular waveguide sections because it allows solving a matrix equation of only 4 by 4 instead of a much larger matrix dependent on the number of layers. Finding the ordered complex roots of even the 4 by 4 matrix characteristic equation is non-trivial. With a one-layer test case we did not obtain the same agreement seen in figure 4 of [75]. The results are given in a unitless quantity of the product of wavelength and propagation constant. It turns out the result is not just linearly dependent on wavelength, so although the plotted quantity is unitless, it is frequency dependent. Hu does not include the wavelength for the examples provided so it is not possible to reproduce his findings. Locating the complex roots of the matrix characteristic equation provides the modal propagation constants. Knowing the order of the roots and not missing roots is critical to the modal analysis but is numerically difficult. Without *a-priori* knowledge of the values or spacing it is difficult to provide a root-finder with an adequate initial guess. Fitting the solution space with a high order polynomial allows the roots to be determined quickly and most importantly, in order, but is a computationally expensive process in its own right. This approach was taken to solve the first 44 roots for a one-layer dielectric-coated waveguide and compared to the 'original method' presented in [75]. The calculated result from the original and modified methods, at 18 GHz, with many different and missing roots between the two methods is shown in Figure 46 and a zoomed perspective in Figure 47. We provide the reference plot from [75] in Figure 48. Hu was able to obtain excellent agreement between the modified and exact, or original, methods at the unknown frequency he considered. Our results showed the modified method finding many more roots and the roots having larger imaginary components. The propagating imaginary components of the propagation constants are in agreement so the method could perhaps still be useful to model the lossy coated waveguide, but the evanescent modes may also have considerable contribution to the total power as the waveguide sections become a small fraction of a wavelength long. This single solve takes approximately 20 minutes for the one waveguide dimension. We expect at least $\lambda/32$ resolution is required to model the cone out of cascaded straight sections. This corresponds to 1184 waveguide sections at the lowest frequency of 18 GHz for the 62 cm long cone. Given the aforementioned root-finding and characteristic equation solution method this would take approximately 395 hours to solve a single frequency point.

The theory has also been developed to model a conical cavity as a cascading set of circular waveguide junctions. This has been done in the past assuming PEC waveguide sections [76], a much simpler situation than ours, but nevertheless a similar approach would be applicable to the lossy dielectric coated waveguide sections.

We are confident that the numerical root finding algorithms could be vastly improved and this solution approach may be potentially efficient. The timeframe for finalizing the absorber design was limited so this solution method was not pursued further.

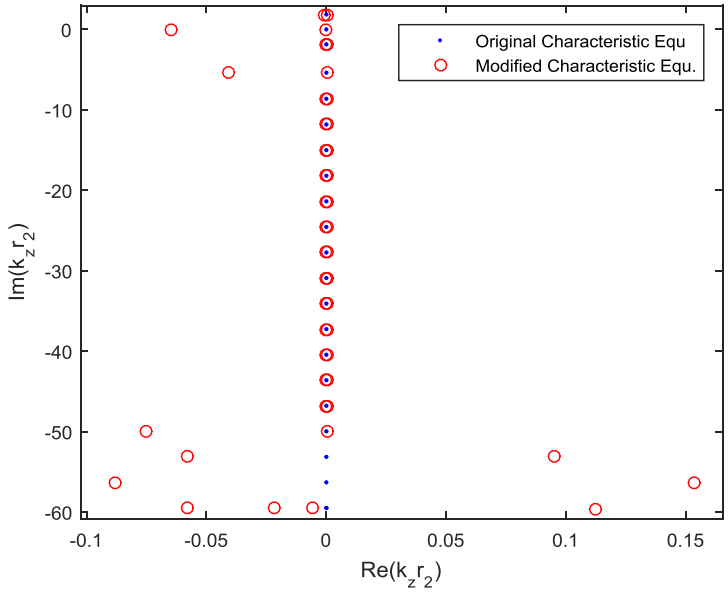

Figure 46: Comparison of two methods to compute complex modal propagation constants in lossy dielectric coated circular waveguide section

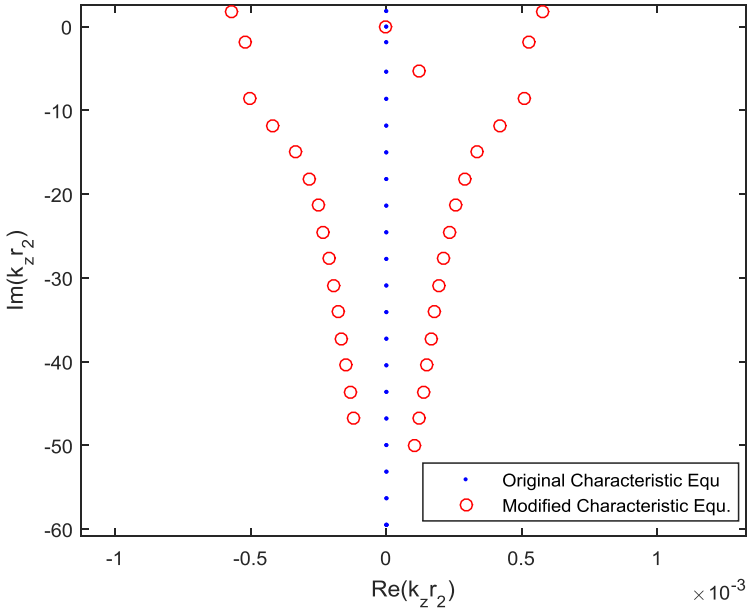

Figure 47: Zoomed perspective; comparison of two methods to compute complex modal propagation constants in lossy dielectric coated circular waveguide section

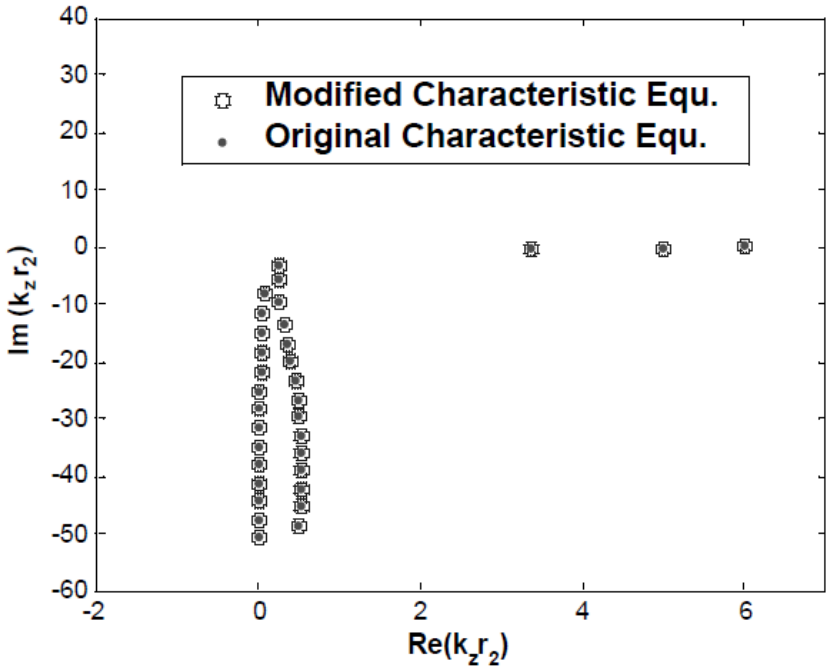

Figure 48: Reference plot, figure 4 from [75]. Comparison of two methods to compute complex modal propagation constants in lossy dielectric circular waveguide section

iv. Comparison GO & BoR-MoM

The body of revolution method of moments (BoR-MoM) is a 2.5 dimensional modeling method that allows efficient modeling of circularly symmetric geometries. Our collaborators at the Institute of Applied Physics at the University of Bern have been using a commercial implementation of this technique through a software package called GRASP [77]. The GRASP software only allows non-dispersive materials, so we were not able to model the true frequency-dependent CBI-loaded Stycast but we were able to model a non-dispersive material in the three models for comparison. We took the 5 mm thick, 3-layered, optimal Stycast absorber design and the corresponding material properties at 57 GHz and modeled the reflectance of this scenario in GO, HFSS, and BoR-MoM. The 108.5 mm radius cone was excited with a Gaussian beam with a beam radius of 36 mm. Convergence was not obtainable on the BoR-MoM with a uniform plane wave excitation, likely due to the fine mesh requirements to model the edge scattering at the aperture. A comparison of the results is given in Figure 49. The BoR-MoM and GO appear to agree closely with the GO model slightly overestimating the reflectance at the peaks of the spectrum. All the methods are comparing the same quantity, the full integrated reflectance over the whole hemisphere. The GO method contains all reflected power in a single 'ray' whereas both

the MoM and the HFSS models require numerical integration over the reflectance hemisphere. The HFSS results show less pronounced reflectance variations over the frequency range as compared to the other two methods. We believe there is some additive numerical noise from the numerical integration of the small magnitude (-60 dB) electric fields. We question the convergence of the HFSS method and presume there may have also been some error due to the finite angular step size of one degree in the output reflectance field.

The agreement between the BoR-MoM and GO results presented here, and further detailed in [71], in addition to the acceptable performance of the optimal design seen in HFSS, was deemed sufficient to proceed with the GO optimized CBI-loaded Stycast layering design.

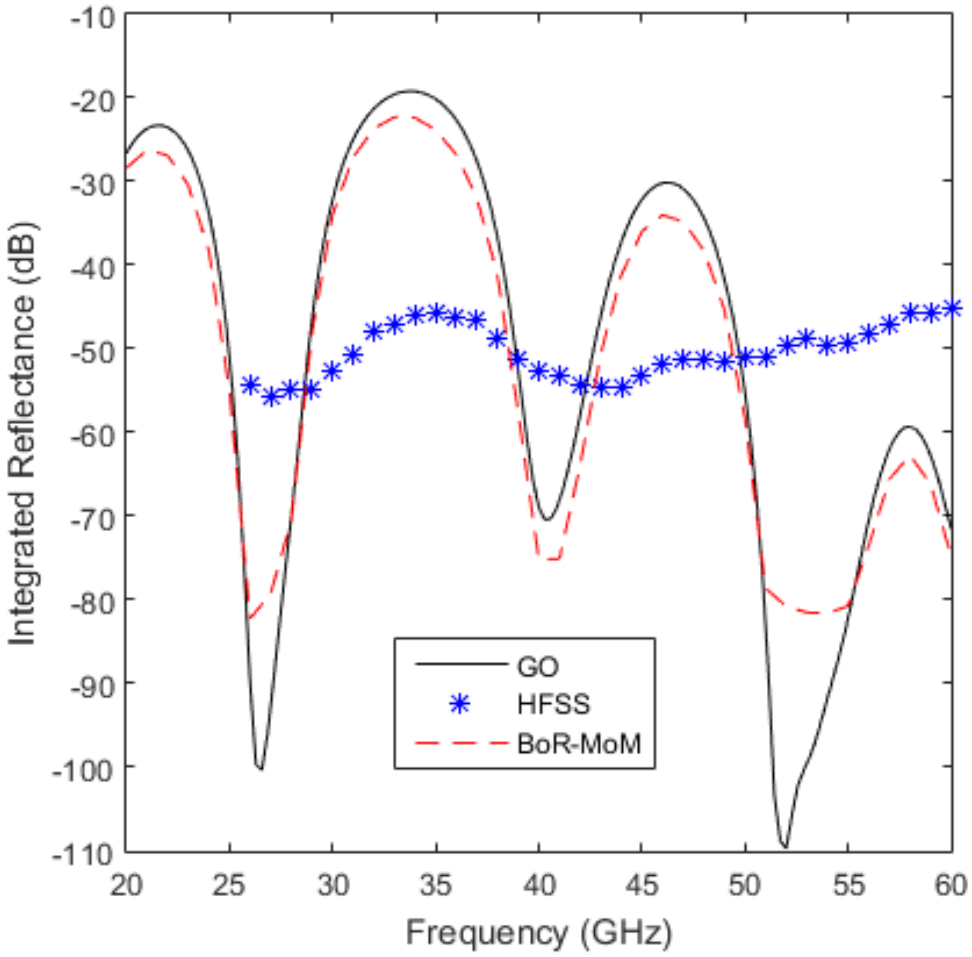

Figure 49: Comparison of Geometric Optics (GO), High Frequency Structure Simulator Finite Element software (HFSS), and Body of Revolution Method of Moments (BoR-MoM). This result is for a fictitious non-dispersive material. Only the result at 57 GHz corresponds to the predicted performance of the conical blackbody design.

C. Effective Blackbody Brightness Temperature and Uncertainty

Brightness temperature is linked to physical temperature and emissivity by definition. At the frequencies and temperatures considered herein, the Rayleigh-Jeans approximation is appropriate with the worst case error introduced at 80 K and 230 GHz equal to 0.5 mK, negligible compared to other uncertainty terms. When we apply the Rayleigh-Jeans and gray body approximations we can express brightness temperature as [78]:

$$T_b = \varepsilon T, \tag{27}$$

where T_b is brightness temperature, ε is emissivity, and T is physical temperature. This relationship is clearly quite simplistic, partially due to its point source formulation and isotropic gray body assumption. This simple relation efficiently conveys the basic principle of a blackbody, when the emissivity is unity, brightness temperature and physical temperature are equivalent. With a uniform, well characterized physical temperature, in addition to emissivity approaching unity, the brightness temperature can be deterministically expressed.

In practice the formulation becomes slightly more complicated, due to the use of directionally dependent absorbing geometries, and the introduction of an antenna viewing the blackbody. When an antenna views the blackbody, the antenna will inevitably receive some energy from outside of the solid angle subtended by the blackbody, often termed spillover. We will also see Ohmic loss and some emission from the antenna material itself. The formulation for brightness temperature as measured from an antenna is given as [32],

$$T_x = \alpha\left(\tilde{T}_b^{bb} + \tilde{T}_b^{bg}\right) + (1-\alpha)T_{phy}^{ant}, \tag{28}$$

where T_x is the brightness temperature seen at the antenna flange, or antenna temperature, $\tilde{T}_b^{bb}$ is the brightness temperature contribution from the blackbody, $\tilde{T}_b^{bg}$ is the brightness temperature contribution from the background, α is the antenna efficiency, and T_{phy}^{ant} is the physical temperature of the antenna. This paper focuses on quantifying the uncertainty of the calibration source, at the source, to remain general and broadly applicable to different ground-calibration environments, and various instrument and antenna configurations. We focus on the blackbody contribution term, and continuing to make the Rayleigh-Jeans and gray body approximations, we can expand this

contribution as follows,

$$\tilde{T}_b^{bb} = \frac{\int_{bb} T_{phy}^{bb}(\theta,\varphi)\varepsilon(\theta)F_n(\theta,\varphi)d\Omega}{\int_{4\pi} F_n(\theta,\varphi)\, d\Omega}, \tag{29}$$

where T_{phy}^{bb} is the solid angle dependent physical temperature of the blackbody, ε is microwave emissivity at the frequency of interest, F_n is the normalized antenna power pattern, and $d\Omega$ is the differential solid angle $sin(\theta)\, d\theta d\phi$. The indices bb and 4π refer to the solid angle subtended by the blackbody and the solid angle of the whole sphere respectively. The spherical coordinate system is shown in Figure 50.

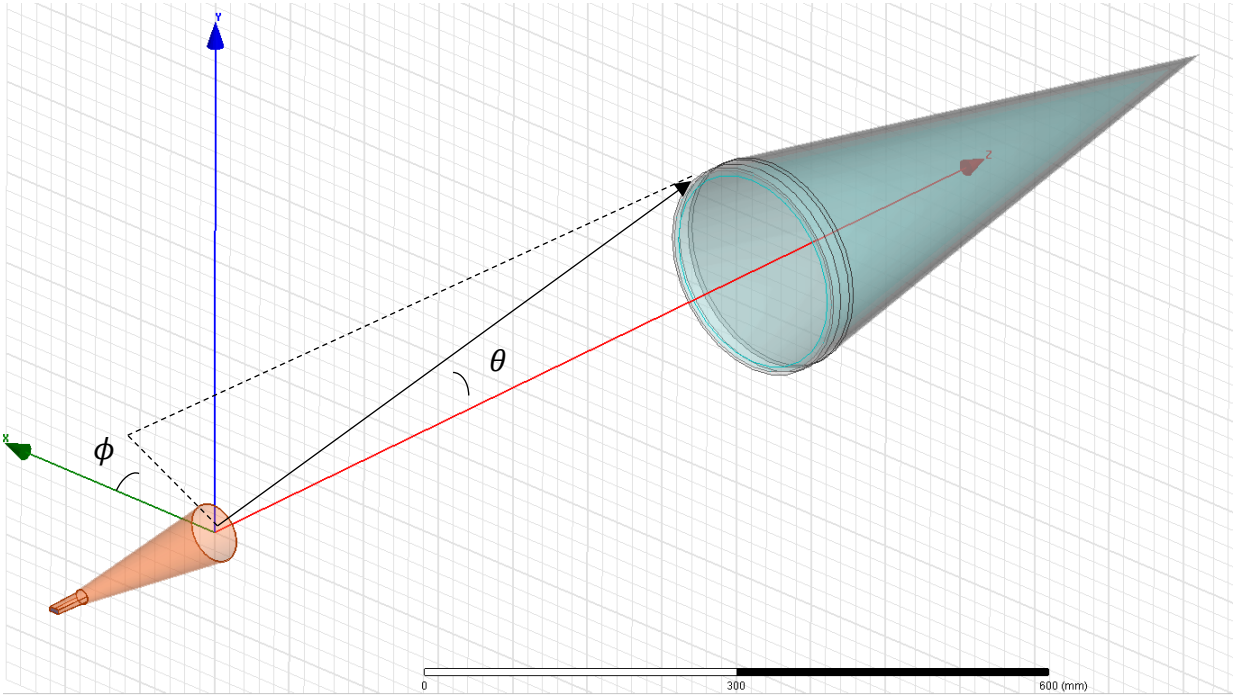

Figure 50: Diagram of antenna and conical blackbody spherical coordinate system. The Z-axis (red) points from the origin at the antenna aperture towards the apex of the cone.

Taking advantage of the circular symmetry of the cones simplifies the analysis of directional dependence. Instead of having emissivity dependent on two spherical angle coordinates, we have dependence only on elevation angle, or θ, the angle measured off of the cone axis. In other words, the conical blackbody is polarization independent. In the ambient temperature laboratory, at horizontal orientation, the physical temperature on the absorber surface

is a function of two spherical angles, because of buoyancy and convection, and the antenna pattern is also a function of two angles in spherical coordinates due to rectangular waveguide polarization. In the thermal-vacuum chamber, in the absence of convective heat loss, the physical temperature also has circular symmetry, eliminating the dependence on the azimuthal angle ϕ. In order to express (28) as a function of illumination efficiency, following the form used in [32], we make the following manipulation to (29),

$$\tilde{T}_b^{bb} = \eta_{IE} T_{eff}^{bb} = \eta_{IE} \left(\frac{\int_{bb} T_{phy}^{bb}(\theta,\varphi)\varepsilon(\theta) F_n(\theta,\varphi) d\Omega}{\int_{bb} F_n(\theta,\varphi)\, d\Omega} \right), \tag{30}$$

where T_{eff}^{bb} is what we call the effective blackbody brightness temperature and the illumination efficiency, η_{IE} is,

$$\eta_{IE} = \frac{\int_{bb} F_n(\theta,\varphi) d\Omega}{\int_{4\pi} F_n(\theta,\varphi)\, d\Omega}. \tag{31}$$

The effective blackbody brightness temperature is the parameter we are concerned with for quantifying the uncertainty associated with the blackbody itself. The uncertainty contribution associated with the spillover to the background, or the illumination efficiency, is discussed in [11]. We take the expression for the effective blackbody brightness temperature, in parenthesis in (30), and perform a Monte-Carlo sensitivity analysis by randomly perturbing the input variables.

We consider the uncertainty in the normalized antenna pattern, F_n, uncertainty in the emissivity, ε, and uncertainty in the physical temperature of the blackbody, T_{phy}^{bb}. These three contributing uncertainty terms are discussed in detail in the following sections, *i*, *ii*, *iii*, but for clarity and reference we provide a summary of the Monte-Carlo components in Table 7.

Table 7: Summary of Monte-Carlo Uncertainty Contribution Terms

Parameter	Expression	Description
effective blackbody brightness temperature of $\boldsymbol{i}$th Monte-Carlo iteration	$\boldsymbol{T_{eff,i}^{bb} = \frac{\int_{bb}\{T_{phy}^{bb}(\theta,\varphi)\}_i \varepsilon_i F_{Ni}(\theta,\varphi) d\Omega}{\int_{bb} F_{Ni}(\theta,\varphi)\, d\Omega}}$	integrated effective blackbody brightness temperature as a function of randomly perturbed inputs with subscript $\boldsymbol{i}$
perturbed physical temperature for ith Monte-Carlo iteration	$\{T_{phy}^{bb}(\theta,\varphi)\}_i = T_{phy}^{bb}(\theta,\varphi) + X_i\left(\sqrt{u_{PRT}^2 + u_{temp}^2(\theta,\varphi)}\right)$	$T_{phy}^{bb}(\theta,\varphi)$ is the simulated physical temperature field, u_{PRT} is the uncertainty in PRT measurements, u_{temp}

		is the uncertainty due to simulation error, environmental variability, and thermal contact
independent, random realization of Gaussian standard normal	$X_i \sim N(0,1)$	perturbs Monte-Carlo samples by a random sample from Gaussian standard normal
perturbed emissivity for ith Monte-Carlo iteration	$\boldsymbol{\varepsilon_i = \varepsilon_{wc} + X_i \sigma_\varepsilon}$	$\boldsymbol{\varepsilon_{wc}}$ is the worst-case emissivity, 0.9999, this corresponds to $\varepsilon_{wc} = 1 - R$, where the total reflectance R is -40 dB $\boldsymbol{\sigma_\varepsilon}$ is the emissivity uncertainty, assigned a value corresponding to ±3 dB of total reflectance
perturbed normalized antenna pattern	$\boldsymbol{F_{N_i}(\theta,\phi) = F_N(\theta,\phi) + 0.01 * X_i(\theta,\phi)}$	$\boldsymbol{F_N(\theta,\phi)}$ is the simulated normalized antenna power pattern 0.01 corresponds to a 1% random noise at each measurement point in spherical coordinate system
array of independent, random realizations of Gaussian standard normal	$\boldsymbol{X_i(\theta,\phi)}$	array of samples from Gaussian standard normal of the same size as interpolated $\boldsymbol{F_N(\theta,\phi)}$ or integration grid, here 512x512
uncertainty of effective blackbody brightness temperature	$\boldsymbol{u_{T_{eff}^{bb}} = \sqrt{\sigma_{T_{eff}^{bb}}{}^2 + \left[\left(\frac{1}{N}\sum_{i=1}^{N} T_{eff,i}^{bb}\right) - E[T_{eff}^{bb}]\right]^2}}$	root sum square of the standard deviation of $\boldsymbol{N}$ Monte-Carlo samples plus the convergence bias
standard deviation of N iterations of $T_{eff,i}^{bb}$	$\boldsymbol{\sigma_{T_{eff}^{bb}} = std(T_{eff,i}^{bb})}$	compute unbiased estimate of standard deviation of N samples

i. Antenna Pattern Simulations

The commercial software package HFSS is often used to simulate antenna power patterns. The finite element method is well suited for solving antenna patterns due to their moderate electrical size and single mode excitation. We have multiple licenses for this software at NIST so it was a logical choice for simulating antenna patterns.

Standard gain horns are often the cheapest and most prevalent horn antennas available. Most satellite instruments use higher gain corrugated antennas with lower sidelobes, but we demonstrate the method with standard gain horns as a 'worst case' scenario. It will be shown that a more directional antenna will result in a lower effective blackbody brightness temperature uncertainty.

We have procured pyramidal and conical standard gain horns in WR-42, WR-22, WR-15, and WR-10. A selection of these horns are shown in Figure 51. The antenna patterns are simulated for all of the remote sensing critical frequencies mentioned in the optimization procedure of section V.B.. These frequencies were 18, 19, 22, 23, 23.8, 31.4, 50, 50.3, 51.76, 52.8, 53.596, 57.29, 60, 88.2, 90, 118, 165.5, and 183.31 GHz. We have excluded 220 GHz as we do not currently possess test equipment in WR-5 or WR-4. We show an example of the simulated antenna power pattern at two polarizations at 88.2 GHz in WR-10 in Figure 52. We impose a 1% Gaussian random error on the normalized antenna pattern, a reasonable estimate based on antenna pattern measurements conducted at NIST. The resulting expression for the normalized antenna pattern is given as,

$$F_{N_i}(\theta,\phi) = F_N(\theta,\phi) + 0.01 * X_i(\theta,\phi), \quad (32)$$

where F_{N_i} is the normalized antenna power pattern for the ith Monte-Carlo iteration, F_N is the nominal simulated antenna power pattern, and X_i is the ith random realization of the standard normal Gaussian N(0,1).

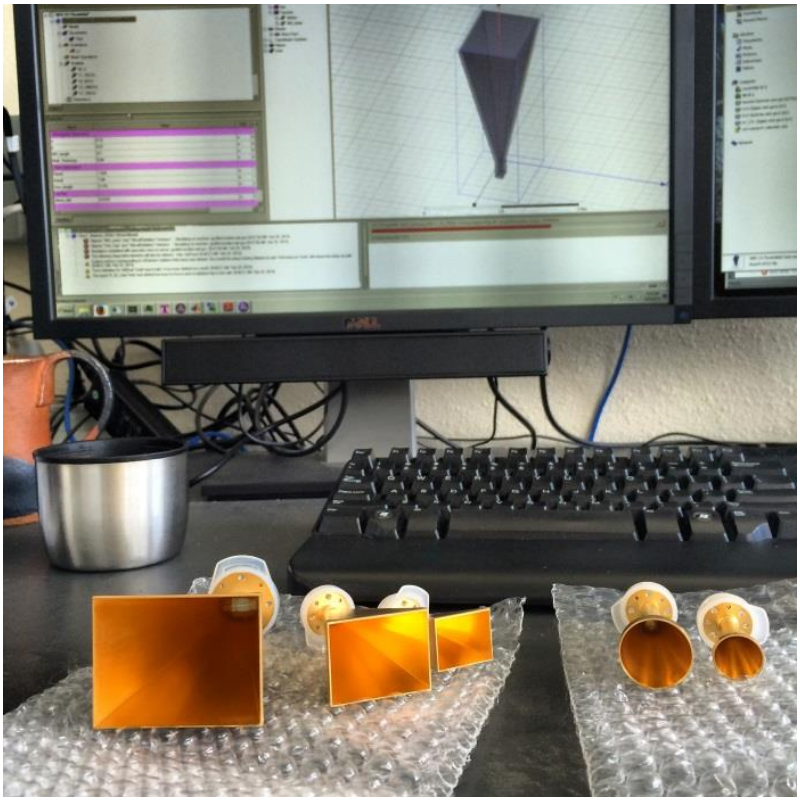

Figure 51: Standard gain horns for WR-42, WR-22, WR-15, and WR-10

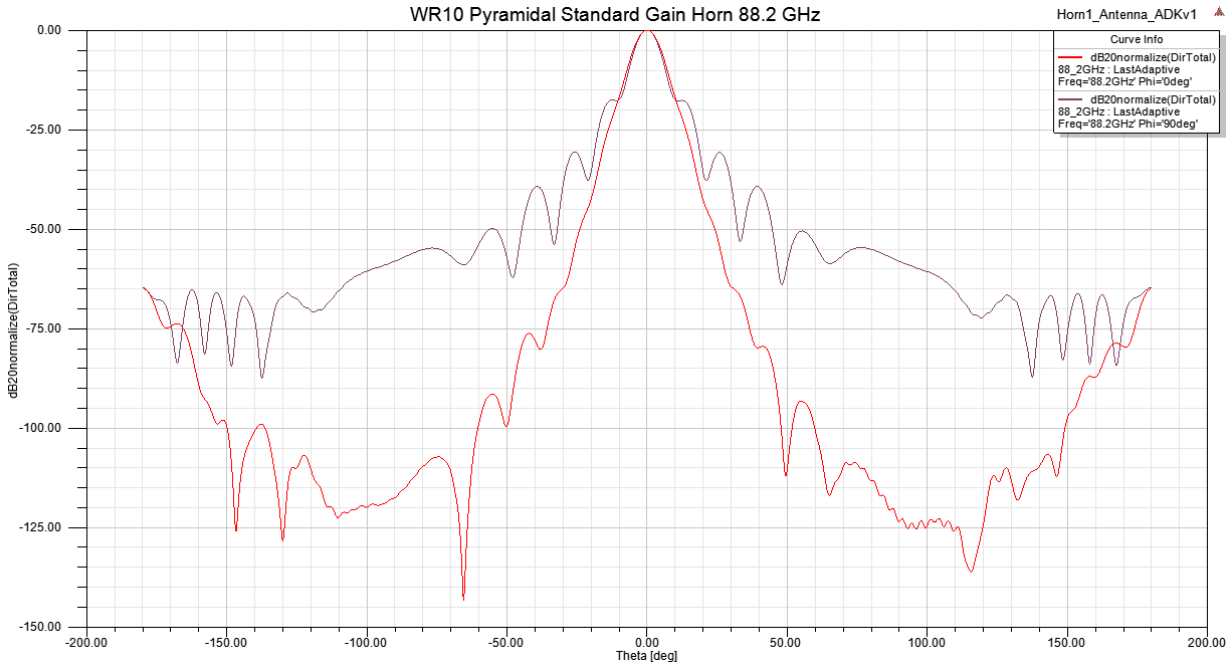

Figure 52: Example of HFSS simulated normalized antenna power pattern at 88.2 GHz for WR-10 pyramidal standard gain horn

ii. Emissivity Uncertainty

The contribution of emissivity to the uncertainty in the effective blackbody brightness temperature was first modeled from simulation and later simplified due to experimental results. A total hemispherical reflectance of -40 dB corresponds to an emissivity of 0.9999. When considering a maximum brightness temperature of about 350 K, this corresponds to a brightness temperature uncertainty of 0.0342 K.

For the pre-fabrication design model we used the HFSS hemispherical reflectance to model the predicted uncertainty. There were many more uncertainty contributors in the simulated emissivity than in the measured result, though we were only able to experimentally measure the monostatic reflectance, and not the BRDF required to fully characterize emissivity. The HFSS-modeled design had uncertainty contributions from material properties, numerical convergence, and absorber layer thickness. Running a Monte-Carlo simulation in the electrically large HFSS FEM model was impractical due to the long solve times. The lower limits of the manufacturer-quoted achievable layer thickness tolerance were simulated to see the sensitivity to this variable. In other words, simulating the effect of an erroneously thin absorber layer. This approach assumes that a thinner absorber layer would always increase reflectance, and that the relationship is linear

within the thickness tolerance. Estimating error sensitivity by simulating at the bounds is a valid approach for the uniform probability distribution such as a tolerance specification, but the Gaussian uncertainty distribution associated with the material property uncertainty would require many random iterations of the two complex material parameter inputs into the FEM to obtain the resulting reflectance distribution. This FEM uncertainty quantification approach was abandoned and an attempt was made to use the geometric optics model to propagate the material property uncertainty to the reflectance. The geometric optics model runs quickly and outputs the total reflectance, a much better candidate for Monte-Carlo analysis than the cumbersome FEM model. The ±0.2 mm thickness tolerance was modeled as a uniform random variable and the uncertainties in complex ε_r and μ_r were considered Gaussian random variables. The input error for the fit material properties was estimated from the maximum difference between measured and fit material parameters for each of the 4 components of the two complex terms, a conservative standard error estimator. These maximum deviations, larger than the uncertainties on the measured material properties, are used across all frequencies. Figure 53 shows the result of the geometric optics reflectance Monte-Carlo analysis for 100 independent samples.

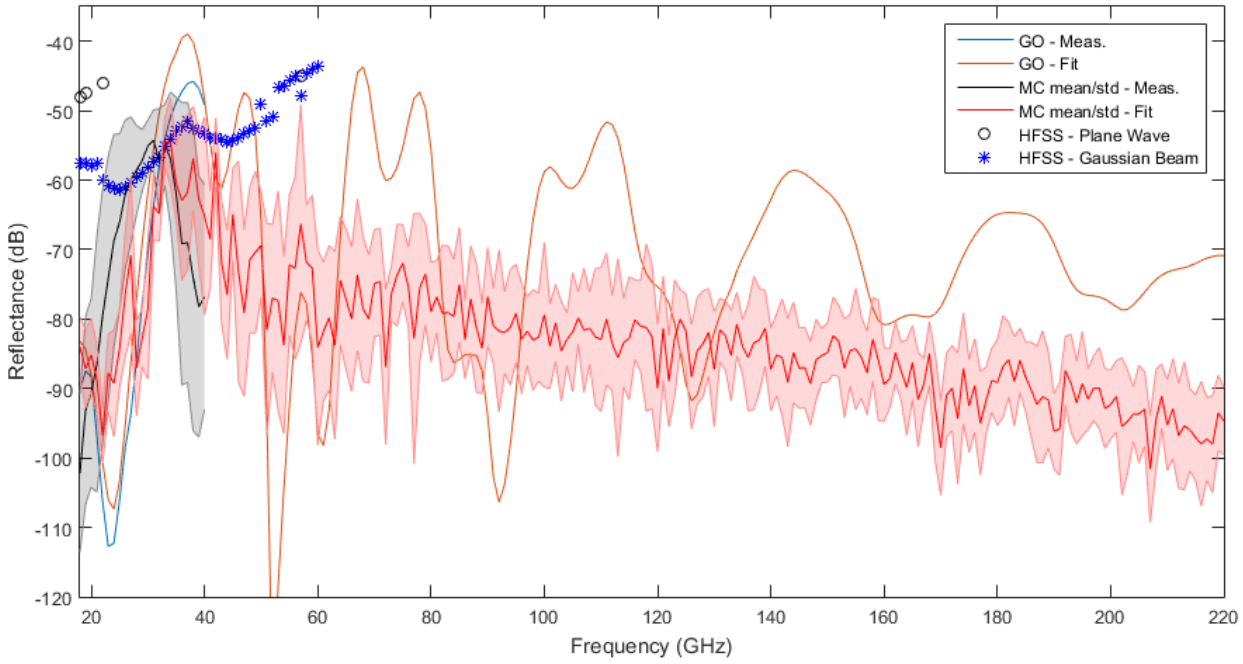

Figure 53: Result of geometric optics Monte-Carlo reflectance uncertainty propagation

We see that the mean of the Monte-Carlo iterated reflectances is not equivalent to the expected value of the reflectance. This suggests that the reflectance has a non-Gaussian

distribution. We see that the layer thickness uncertainty 'washes out' the spectral reflectance peaks by shifting the deep troughs across the frequency range over the individual random realizations. Because of this considerable bias between the expected value of the reflectance and the mean of the Monte-Carlo samples we never considered this simulation converged. We did not find an efficient model to propagate the reflectance uncertainty and ultimately ended up relying on the experimental measurement to approximate the uncertainty in the emissivity.

We showed in section V.B. that at low reflectance magnitudes the isotropic radiator assumption provides a reasonable estimate of the integrated reflectance. We would ultimately like to measure the BRDF of the conical target to provide primary traceability to emissivity, but for the uncertainty estimate we use the monostatic reflectivity measurement to confirm a 'worst case' reflectance of -40 dB with an associated maximum uncertainty of 3 dB. We show in section VI.A. that this is a reasonable worst case value. For simplicity, and because of its relatively small uncertainty contribution in comparison to the physical temperature, we use these quantities across the frequency band for the Monte-Carlo uncertainty estimate. The resulting expression for the emissivity of the ith random iteration can be expressed as,

$$\varepsilon_i = \varepsilon_{wc} + X_i \sigma_\varepsilon \tag{33}$$

where ε_i is the input emissivity for the ith iteration, ε_{wc} is the worst case emissivity, or -40 dB, σ_ε is the standard error of the emissivity, or 3 dB, and X_i is the ith random realization of the standard normal Gaussian N(0,1). The X_i here is independent from the X_i of section i. This operation is performed in dB, assuming a lognormal distribution on the emissivity error, and then converted to linear units for the remainder of the effective brightness temperature calculation.

iii. Physical Temperature Uncertainty

In order to calculate the realistic effective blackbody brightness temperature based on the simulated physical temperature, we first needed to simulate the target temperature at the actual achievable temperature. The FEM thermal simulation discussed in section IV.C. was re-run using a copper backside temperature of 342.8 K, the mean measured PRT temperature when the target is heated. The target is simulated with the polyethylene insulation layer and without the insulation to study differences, and for comparison to the infrared image discussed in section VI.C.. We show the simulated target temperatures in Figure 54 and Figure 55 for the polyethylene insulated cone and non-insulated cone respectively. The temperatures shown in these figures are used as

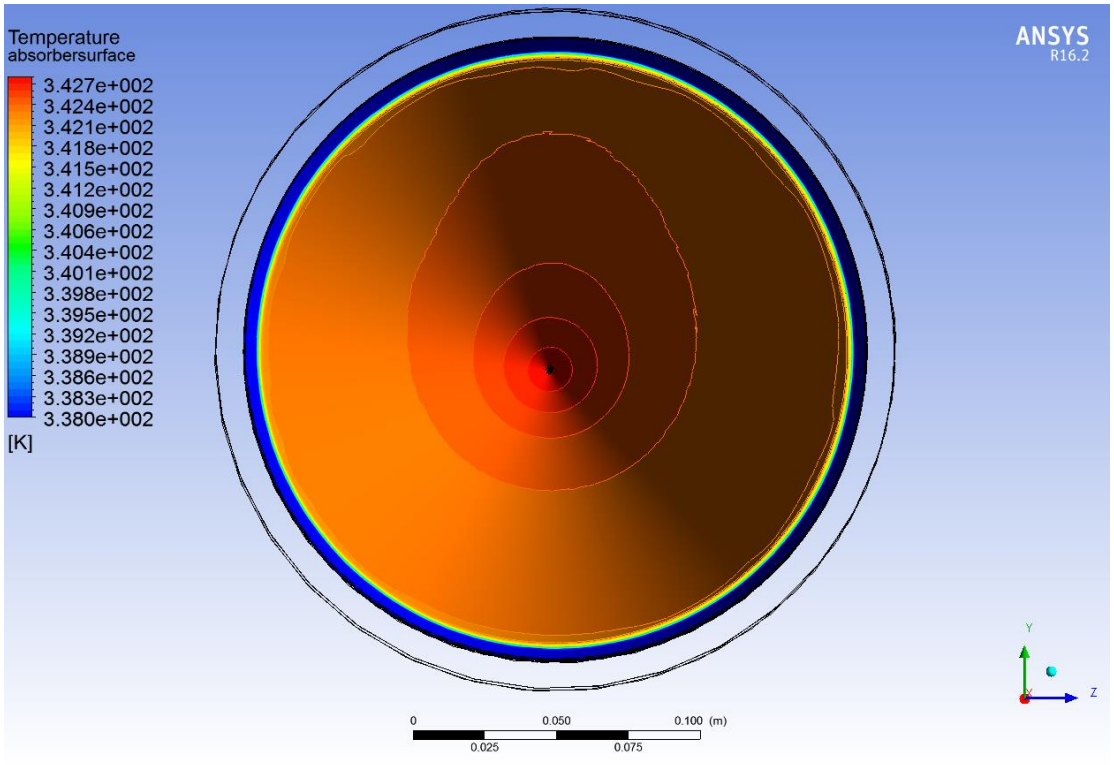

Figure 54: Simulated temperature distribution on absorber surface looking into cone with polyethylene insulation

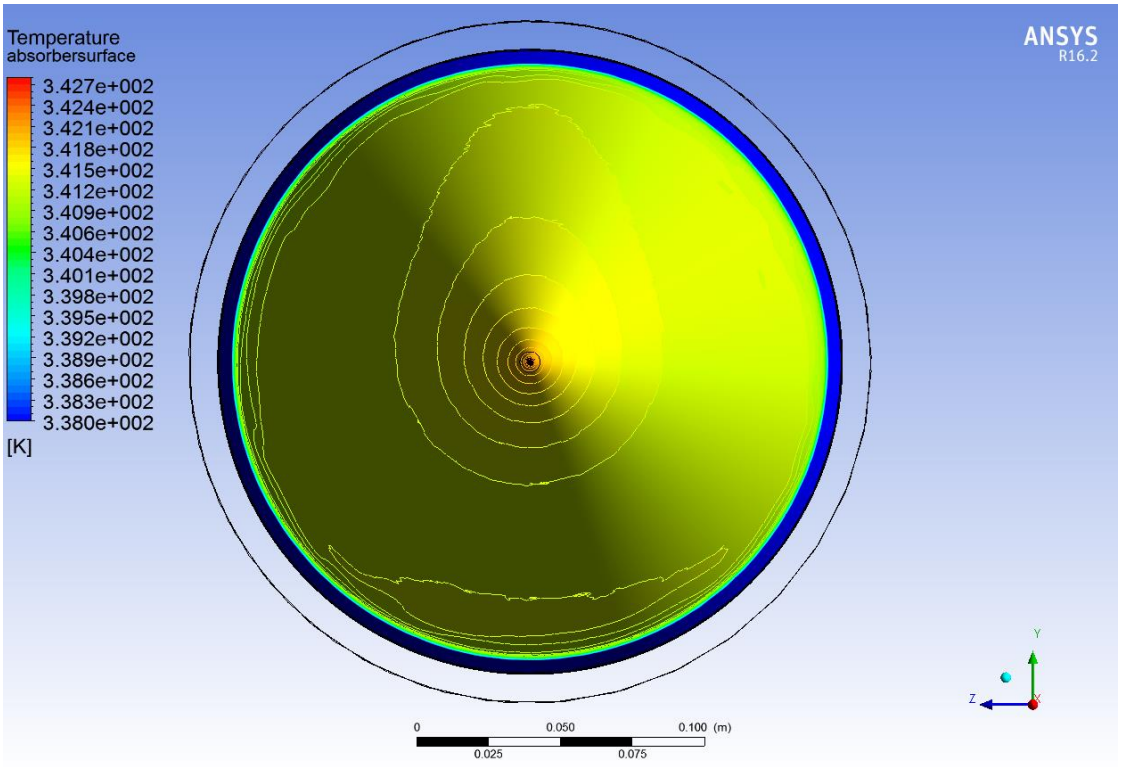

Figure 55: Simulated temperature distribution on absorber surface looking into cone without polyethylene insulation

the $T_{phy}^{bb}(\theta, \varphi)$ in the effective blackbody brightness temperature calculation. The theta is distance dependent as shown in Figure 50.

We now consider the sources of uncertainty. There are two primary contributors to the uncertainty of the physical temperature of the cone. First, there is uncertainty associated with the PRT sensors themselves, stemming from both the sensor calibration curve, conversion of Ohms to Kelvin, and the Type-B uncertainty of the temperature monitor with respect to the Ohm. The equipment we use to sense the temperature on the backsides of the copper cones are 12 Lakeshore PT103 PRTs and a Lakeshore LS-224 temperature monitor, and 8 Lakeshore PT103 PRTs and a Lakeshore LS-218 temperature monitor for the larger and smaller cones respectively. The quoted uncertainty of a Lakeshore calibrated PRT is 0.023 K. Because we purchased uncalibrated PRTs and calibrated them ourselves with a 5-point calibration this added another calibration uncertainty contribution. The PRTs were calibrated to the mean of 3 Lakeshore calibrated PRTs in a waterbath at 5 temperatures between 290 K and 342 K. The resistance versus mean calibrated PRT temperature was fit with a line for each of the 12 sensors. The calibration uncertainty was taken as the mean residual of the linear fit. These values showed a maximum of 0.021 K. Taking the root sum square of the two calibration uncertainties we obtain a PRT calibration uncertainty of 0.031 K that we will call u_{cal}. The uncertainty contribution from the temperature monitor is a function of the measured resistance and thus a function of temperature. The manufacturer quoted uncertainty, for the range of resistances under consideration, is 0.004 Ω + 0.01% of the measured quantity. Converting to Kelvin with the typical PT103 sensitivity of 2.58 Ω/K this corresponds to,

$$u_{monitor} = 0.0103\ \mathrm{K} + 0.0001 * \mathrm{T}_{meas}, \tag{34}$$

where T_{meas} is the measured temperature in Kelvin and $u_{monitor}$ is the uncertainty associated with the temperature monitor in Kelvin. Now we can express the total PRT uncertainty as the root sum square of the PRT calibration and monitor uncertainties,

$$u_{PRT} = \sqrt{{u_{cal}}^2 + {u_{monitor}}^2}, \tag{35}$$

where u_{PRT} is the uncertainty of a single PRT measurement. For the maximum observed target temperature of about 342.8 K, this uncertainty corresponds to 0.054 K.

Second, the other physical temperature uncertainty contribution relates to how well we know the temperature distribution on the absorber surface, or the variation due to environmental factors and the uncertainty of the FEM simulation itself. We have found from many simulations,

with and without convection, with and without polyethylene, at different levels of fan-forced convection that the temperature of the absorber surface near the apex of the cone is invariably equivalent to the copper backside temperature within 0.01 K. There remain some sources of potential difference between model and reality in that we assume perfect thermal contact between the copper and the absorber layer in the thermal model. To account for this difference, we conservatively estimate the uncertainty at the cone apex as 0.05 K. The physical temperature uncertainty closer to the aperture of the cone has been shown to have higher variability dependent on the environmental conditions and the presence of the polyethylene insulation. We model this as a linear, radius dependent, uncertainty term. The temperature uncertainty at the aperture of the cone is assigned a value of 0.4 K. The temperature uncertainty due to environmental variation, and due to model convergence and meshing errors are difficult to quantify so we chose 0.4 K, a value we consider a conservative estimate. The linear radius dependent temperature uncertainty is thus modeled as,

$$u_{temp}(\theta) = 0.05\ K + \frac{\theta}{\theta_{max}} 0.35\ K, \tag{36}$$

where u_{temp} is the linear radius dependent uncertainty, note we have transformed the radius into θ by the relation $\theta = \tan(\frac{r}{d})$, where r is radius and d is the distance from the target to the horn aperture. The parameter θ_{max} refers to the value of θ at the aperture of the target, or where $r = .1085\ m$ for the large target. The randomly permutated physical temperature can then be expressed for the ith Monte-Carlo iteration as,

$$\left\{T_{phy}^{bb}(\theta,\varphi)\right\}_i = T_{phy}^{bb}(\theta,\varphi) + X_i\left(\sqrt{u_{PRT}^2 + u_{temp}^2(\theta,\varphi)}\right), \tag{37}$$

where $\left\{T_{phy}^{bb}(\theta,\varphi)\right\}_i$ is the target physical temperature for the ith iteration, and X_i is a random realization from the standard normal Gaussian, N(0,1). The X_i here is independent from the X_i discussed in sections *i* and *ii*. We now have quantified the uncertainty associated with each input to the effective blackbody brightness temperature and we can proceed to run the Monte-Carlo simulation.

iv. Monte-Carlo uncertainty

In order to perform numerical integration of the product of the antenna pattern, emissivity, and physical temperature, according to,

$$T_{eff,i}^{bb} = \frac{\int_{bb}\left\{T_{phy}^{bb}(\theta,\varphi)\right\}_i \varepsilon_i F_{Ni}(\theta,\varphi)d\Omega}{\int_{bb} F_{Ni}(\theta,\varphi)d\Omega}, \tag{38}$$

where the variables have been derived and defined in equation (30), we interpolate the data onto two dimensional grids of θ and φ. We prescribe 512 points between 0 and θ_{max} for θ and 512 points between 0 and 2π for φ. We run 100 Monte-Carlo iterations in parallel on a 16 core machine, and it takes about 1 hour per frequency point. Each randomly perturbed iteration of the input variables $F_{N_i}(\theta,\phi)$, ε_i, and $\left\{T_{phy}^{bb}(\theta,\varphi)\right\}_i$ are input to (38) and the effective blackbody brightness temperature for the ith Monte-Carlo iteration, $T_{eff,i}^{bb}$, is solved. The resulting standard uncertainty of the effective blackbody brightness temperature, $u_{T_{eff}^{bb}}$, is calculated as,

$$u_{T_{eff}^{bb}} = \sqrt{{\sigma_{T_{eff}^{bb}}}^2 + \left[\left(\frac{1}{N}\sum_{i=1}^{N} T_{eff,i}^{bb}\right) - E[T_{eff}^{bb}]\right]^2}, \tag{39}$$

where ${\sigma_{T_{eff}^{bb}}}^2$ is the standard deviation over the $N = 100$ iterations of i, and $E[T_{eff}^{bb}]$ is the expected value of the effective blackbody brightness temperature calculated from the un-perturbed case. The second term under the radical in (39) adds the uncertainty due to the convergence error or bias in the Monte-Carlo estimation. This bias term takes on values of less than 0.01 K for all distances and frequencies, suggesting adequate convergence relative to the quantities of interest. We also calculate the difference between $u_{\tilde{T}_b^{bb}}$ for $N = 50$ and $N = 100$ iterations. This difference is less than 0.005 K for all variations, providing a bound on convergence error of the uncertainty, $u_{\tilde{T}_b^{bb}}$, of about 5%. We show the calculated blackbody brightness temperature versus frequency and error bars equal to one standard uncertainty $u_{\tilde{T}_b^{bb}}$ for the set of 16 remote sensing frequencies in Figure 56. The results presented are calculated for the 22 cm diameter target for a backside copper temperature of 342.75 K, the hottest our available water circulator was capable of reaching. This analysis took about 84 minutes per frequency point running on 16 processors for a total time of 22.3 hours. We also calculated the distance dependence of the effective blackbody brightness temperature and uncertainty as a function of separation distance and plotted for the polyethylene insulated, and non-insulated cases in Figure 57 and Figure 58.

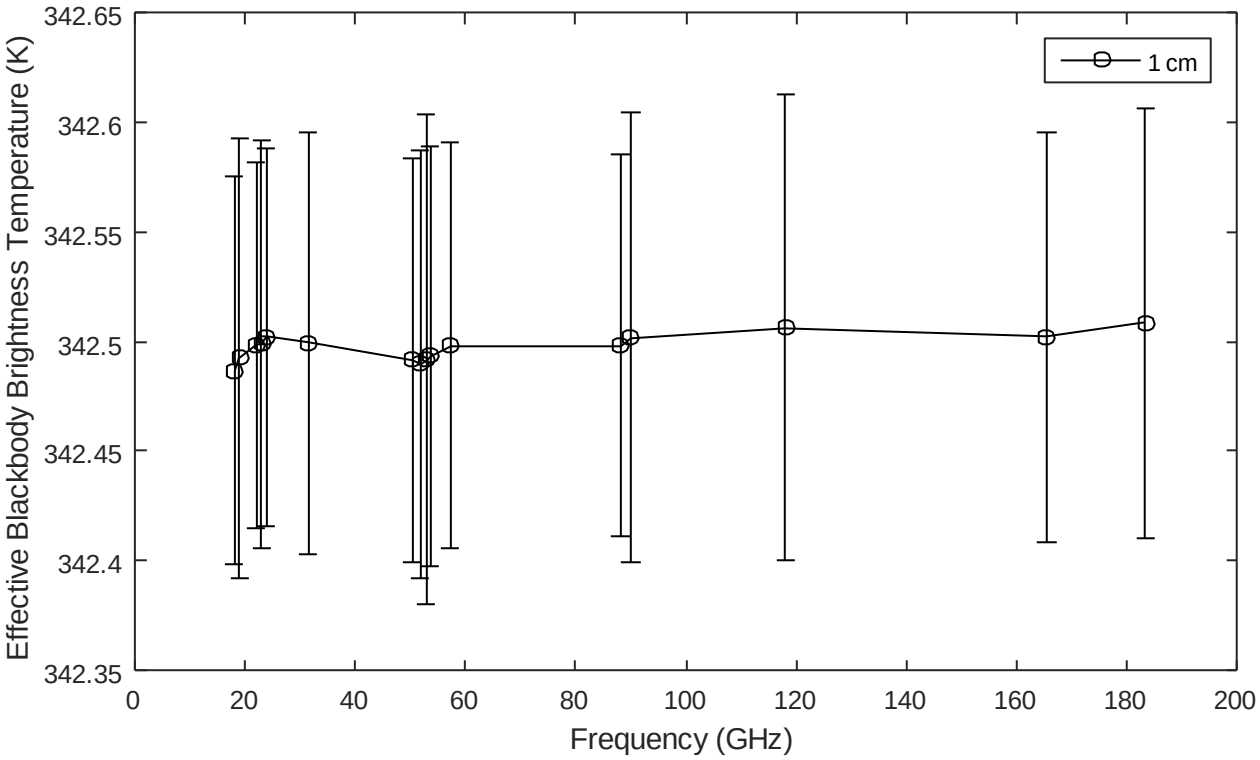

Figure 56: Calculated effective blackbody brightness temperature versus frequency with Monte-Carlo uncertainty estimates shown as error bars. Polyethylene insulated case.

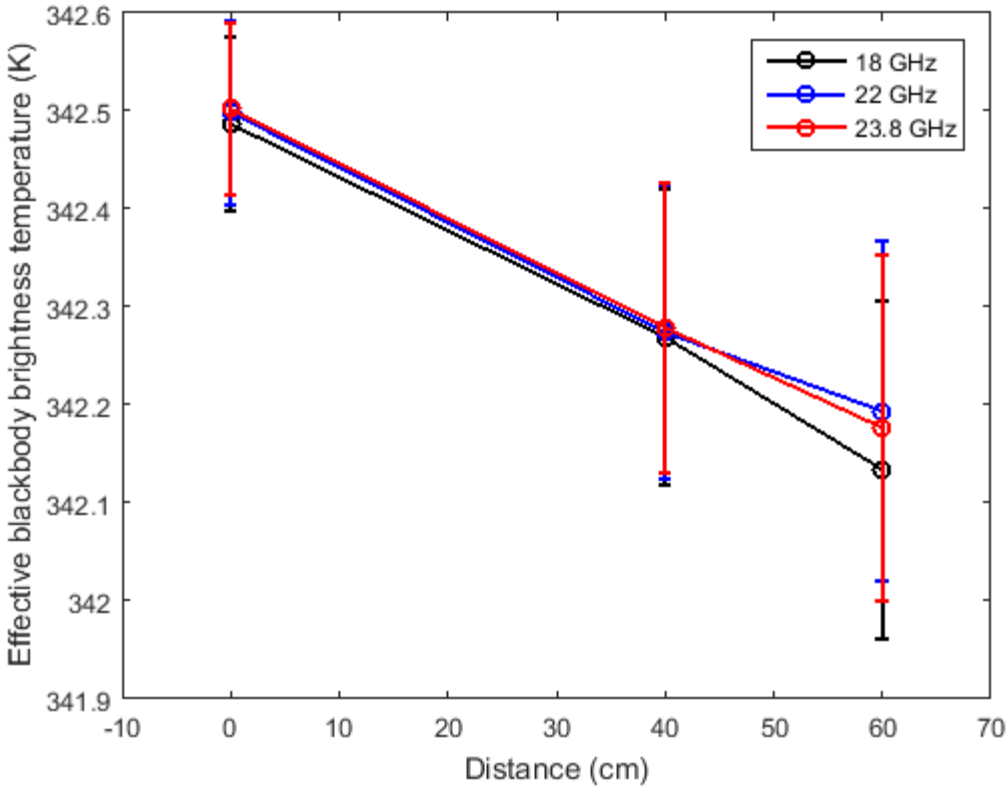

Figure 57: Calculated effective blackbody brightness temperature versus distance with Monte-Carlo uncertainty estimates shown as error bars. Polyethylene insulated case.

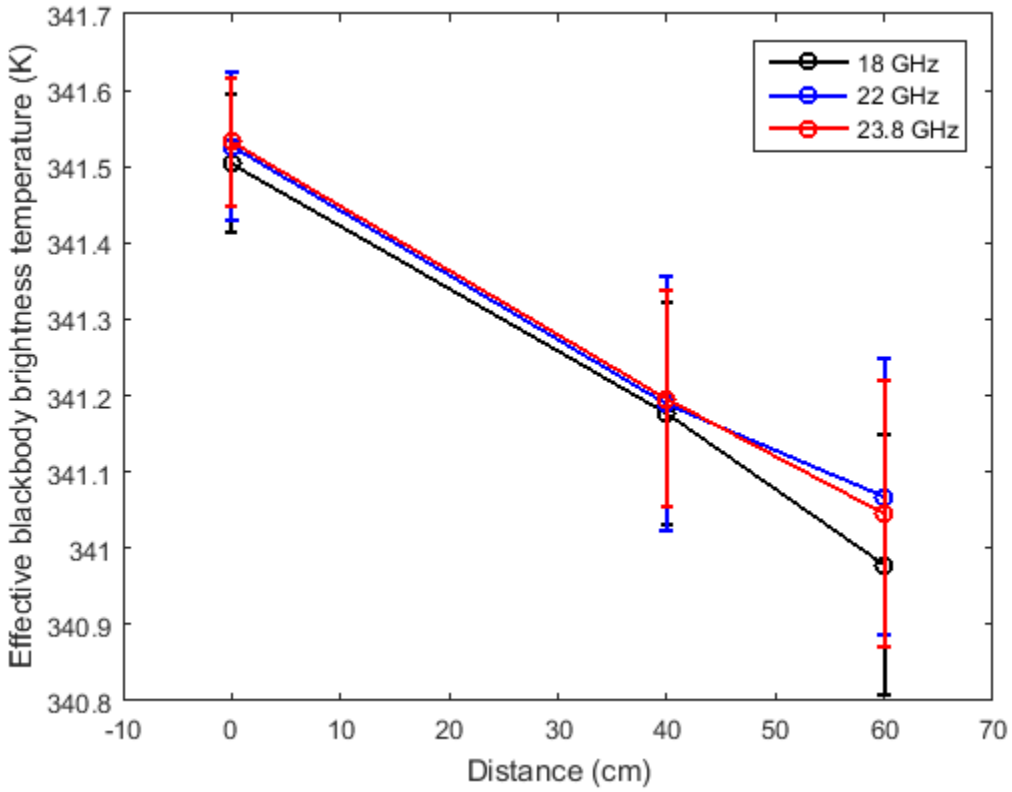

Figure 58: Calculated effective blackbody brightness temperature versus distance with Monte-Carlo uncertainty estimates shown as error bars. Non-insulated case.

As expected, we see decreasing effective blackbody brightness temperature with distance, as well as increasing uncertainty. This relates to how the antenna pattern 'illuminates' the target at further distances. At 1 cm, the main beam of the antenna falls in and around the hotter apex of the cone and as the distance decreases, more of the antenna beam sees the cooler aperture edges of the cone. The uncertainty increase is due to the radius dependent temperature uncertainty. As the distance increases the horn 'sees' more of the higher uncertainty cone aperture. Higher frequencies, for a given horn dimension, will have more directionality, or higher maximum gain. We see this relationship in the effective target brightness temperature difference between frequencies. A more directional horn antenna than a standard gain horn will be weighted more heavily at the center of the cone resulting in a slightly higher effective blackbody brightness temperature and lower uncertainty.

VI. CHARACTERIZATION

A. Monostatic Reflectivity

Full characterization of true solid-angle-dependent emissivity requires BRDF measurements over a full range of incidence angles. This measurement is difficult to realize in practice, and a monostatic S_{11} measurement has often been accepted as an adequate approximation for expressing the emissivity of calibration sources [79]. NIST has developed a method of performing a free-space calibration of monostatic reflectance measurements [80]. The experimental approach presented here follows this measurement method and analysis.

We measure the reflectivity at a distance greater than the $2D^2/\lambda$ far-field criterion for the far-field measurement, and at distances between 1 mm and 5 cm for the near-field measurements. Reported distances are measured from the horn aperture to the cone aperture. All measurements have been performed for the larger of the two targets of 22 cm diameter.

The conical target is attached to a linear motion stage capable of 2 μm repeatable steps over a 30 cm distance. The cone and linear motion axis are aligned with a standard gain horn antenna and straight waveguide section by use of a laser, shone through the waveguide flange, horn, cone aperture, and into the apex of the cone. A vector network analyzer (VNA) is attached to the aligned waveguide section. The horn is then removed and the VNA is calibrated with the one-port short-offset-load (SOL) method. The horn is then reattached after the VNA has been calibrated.

We made measurements at 100 MHz increments in the frequency range from 18 GHz to 110 GHz, except for two gaps between 26.5 GHz and 30 GHz, and 67 GHz and 75 GHz because of hardware unavailability. The complex reflection coefficient is measured at multiple distances stepped at less than λ/16 increments over a 5 cm (K-band) to 1 cm (W-band) span. We measure the conical target and a flat polished aluminum plate, following the NIST free-space calibration method.

In the far field, the excitation more closely approximates a plane wave and the edges of the structure are illuminated with equal intensity to the internal apex of the cone. Initially, some of the copper tubing structure and aluminum mounting structure was ‘visible’ to the horn when viewing into the cone. This issue was remedied by placing a piece of anechoic foam absorber in front of the cone with an aperture cut to only allow viewing into the cone. This piece of absorber is separate and freestanding from the linear stage so it will not contribute to the standing wave

when the stage is stepped. A photograph of the far-field reflectivity setup in the anechoic chamber is provided in Figure 59. Figure 60 shows a photograph of the near-field reflector plate measurement setup.

Due to the small magnitude of the standing wave pattern reflected from the target, the drift in the network analyzer becomes significant. We remove this drift, prior to further processing, using a second-order fit. We provide an example of the original raw data at 89 GHz along with the second-order fit and the detrended wave in Figure 61. The detrending process also eliminates the need for the loss term in [80], allowing us to use the simpler and faster linear fitting. The uncertainty due to the gain drift correction is accounted for in the type-B systematic uncertainty, which is greater than the drift amount.

Measured and detrended standing-wave patterns are plotted in Figure 62 and Figure 63, and show, at an arbitrary example frequency of 89 GHz, the target and aluminum reflector in the near-field and far-field, respectively. The far-field wave patterns for the reflector are uniform, whereas the near-field reflector measurement shows an interference pattern from a multiple reflection, presumably the horn. Because of the low reflectance magnitude of the target, this multiple reflection is damped, and the standing-wave pattern is more clearly visible than for the plate.

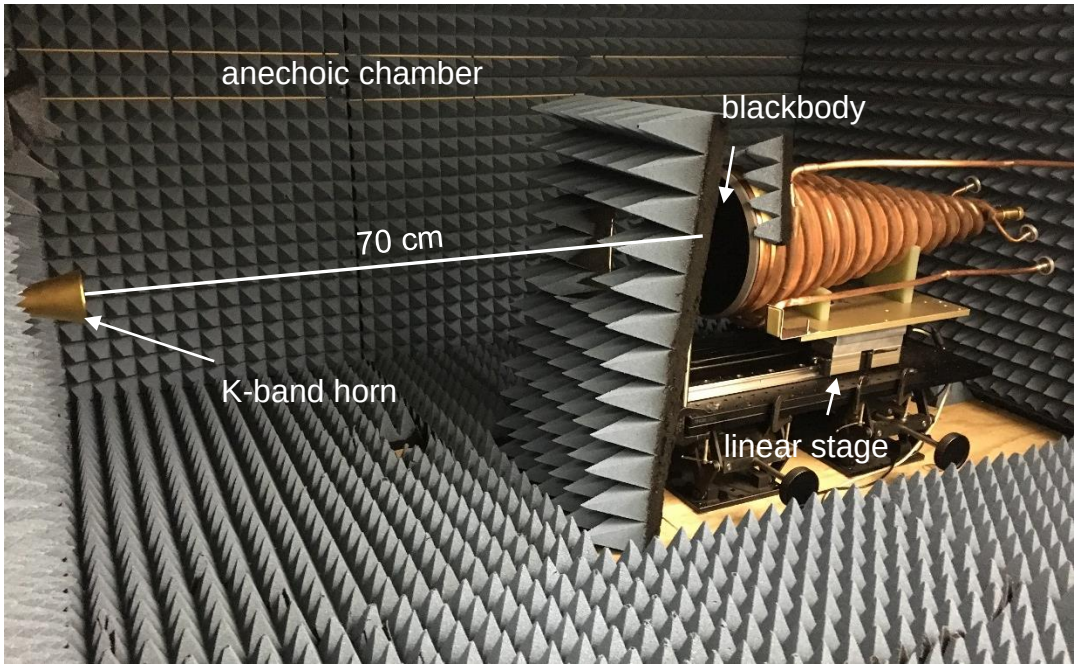

Figure 59: Conical microwave blackbody setup in anechoic chamber for far field reflectivity measurement in K-band

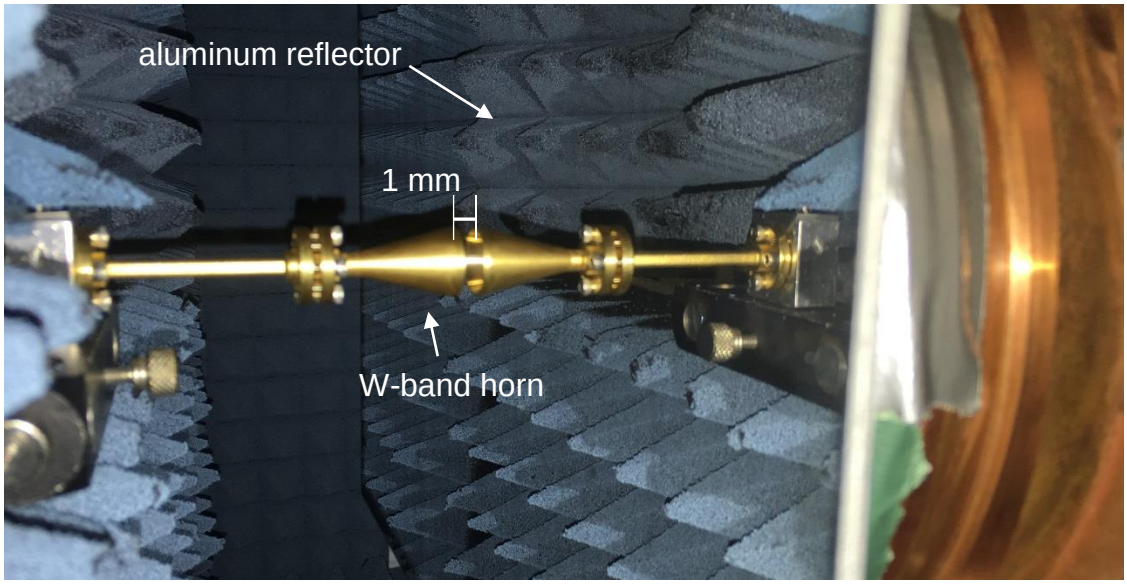

Figure 60: Conical horn and aluminum reflector plate setup in anechoic chamber for near field reflectivity measurements in W-band

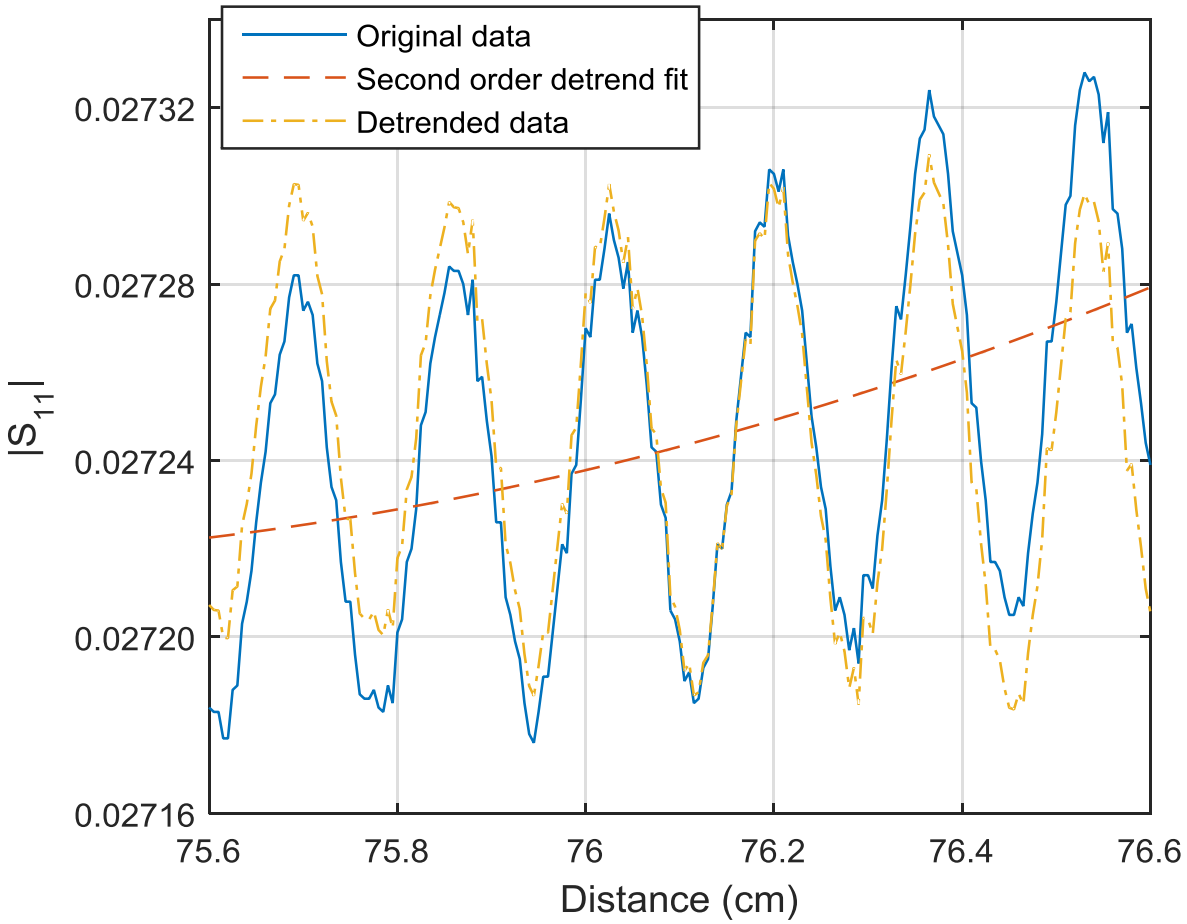

Figure 61: Raw reflectivity data (blue), second order gain drift detrending fit (red) and detrended data. This is an example from far-field data at 89 GHz; equivalent processing was done at all measurement frequencies.

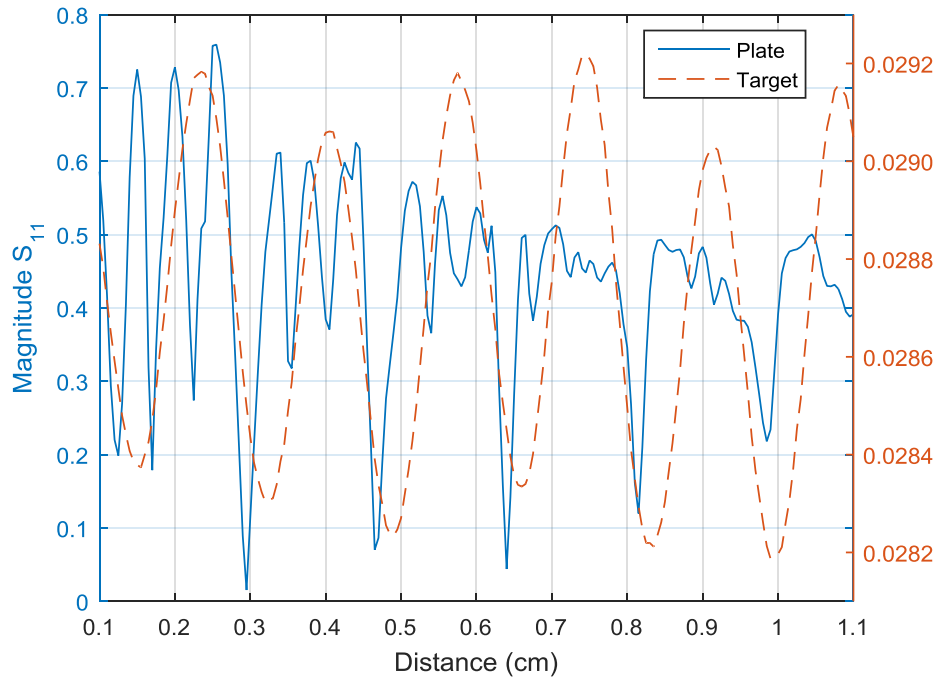

Figure 62: Example of near field standing wave patterns for aluminum plate (solid line, left axis) and conical target (dashed line, right axis) at 89 GHz as a function of distance between horn and cone apertures.

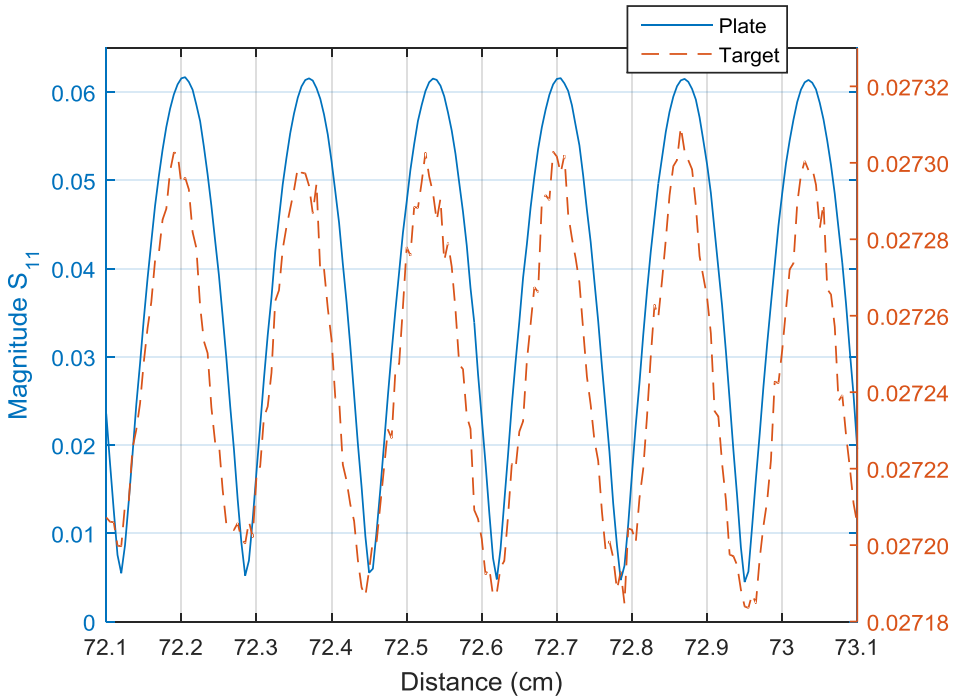

Figure 63: Example of far-field standing-wave patterns for the aluminum plate (solid line, left axis) and conical target (dashed line, right axis) at 89 GHz as a function of distance between horn and cone apertures.

The target reflectivities and associated uncertainties are computed with the linear-fit calibration scheme of [80]. The near-field and far-field reflectivity results and uncertainties are plotted in Figure 64 over the geometric optics data. The GO results vary slightly from the original

design presented in Figure 38 because the final cast absorber cone has a pure Stycast layer thickness of about 1.7 mm instead of the nominal design value of 1 mm. The 5% and 50% loaded CBI Stycast layers are accurately cast at thicknesses of 1.8 mm and 2.2 mm, respectively.

The near-field measurement results and GO theory for the cone with and without the polyethylene insulation layer are displayed in Figure 65 for comparison. This design element greatly reduces temperature gradients on the absorber surface, critical for radiometric brightness temperature characterization, without adversely affecting the EM performance of the blackbody. We see a reduction in reflectivity, as predicted by GO for the insulation layer, at the peaks near 32, 51, and 78 GHz. These differences are not significant with respect to the uncertainty bounds but do adhere to the trend predicted in the model. The reflectivity decrease is assumed to be due to the smoother dielectric transition or gradient impedance matching provided by the insulation. Because of the negligible attenuation loss in the polyethylene, we don't expect any emission or brightness temperature contribution from the polyethylene foam.

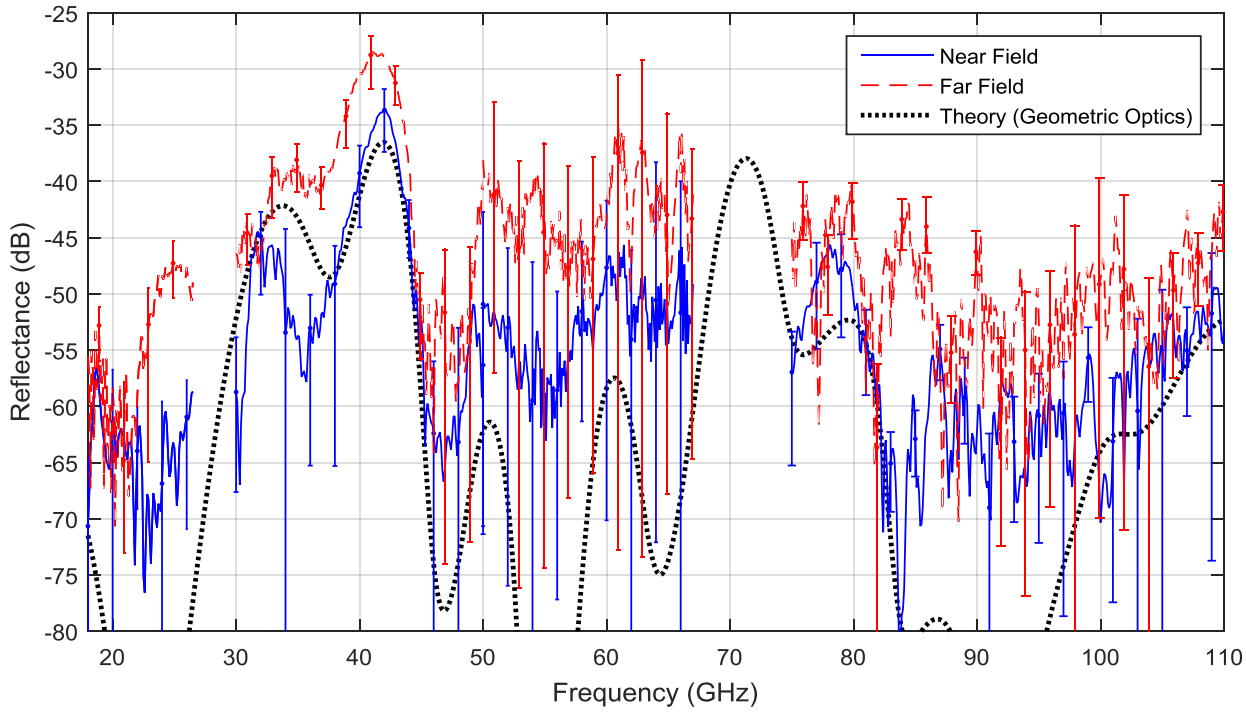

Figure 64: Measured reflectivity spectrum of 11 cm radius NIST conical blackbody in near field (blue solid) and far field (red dashed) along with geometric optics theory (black dotted). Error bars are plotted at 2 GHz increments for clarity, measurements were taken at 100 MHz increments.

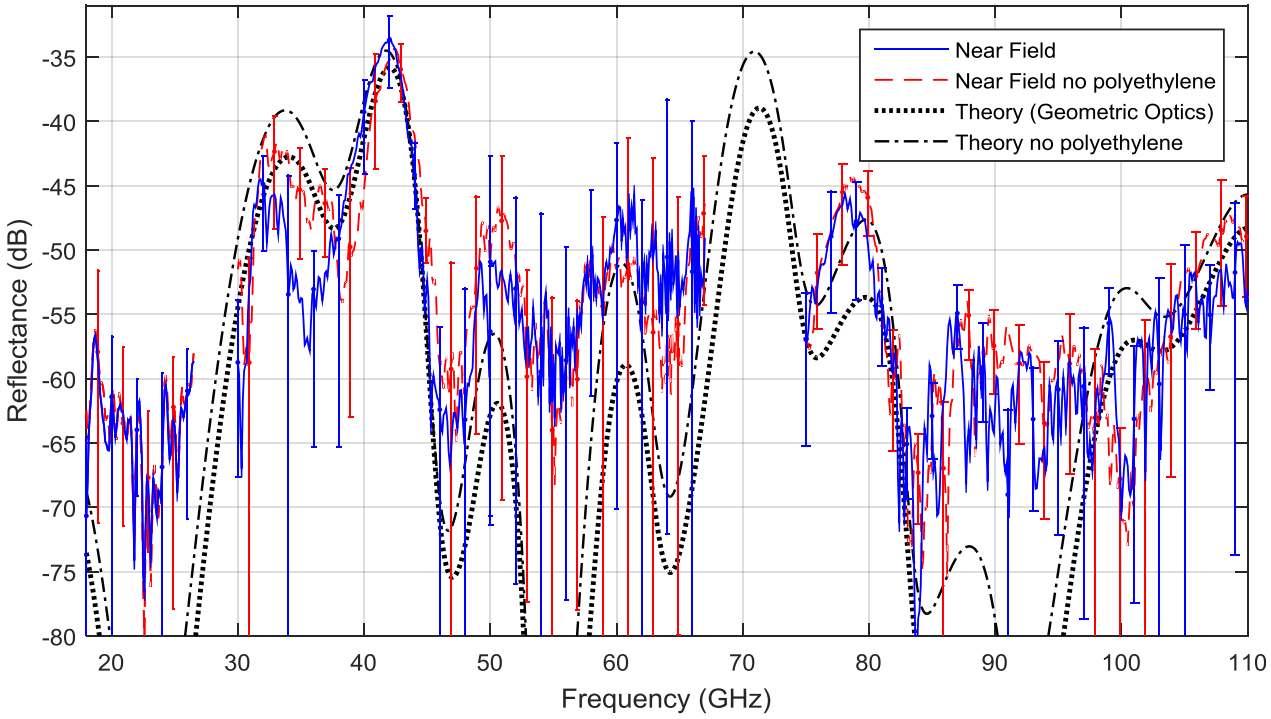

Figure 65: Measured near field reflectivity spectrum of 11 cm radius NIST conical blackbody with HD-80 polyethylene insulation (blue solid) and without insulation layer (red dashed). Geometric optics theory for insulated (black dotted) and non-insulated (black dash-dot) cases. Error bars are plotted at 2 GHz increments for clarity, measurements were taken at 100 MHz increments.

B. NIST Standard Radiometer Brightness Temperature Characterization

The conical blackbody has been proposed for use as a primary standard for microwave brightness temperature. In order to confirm the consistency and traceability to the NIST standard radiometers we measure the conical target with the standard radiometer procedure described in [32]. The NIST standard waveguide radiometers use two primary calibration points, a cryogenic standard and an ambient load to calibrate a highly linear bolometer power detector for thermal noise measurement at the third, device under test port. NIST maintains these waveguide radiometers in WR-62, WR-42, WR-28, WR-19, and WR-15. We demonstrate radiometric consistency at the low-end of the design frequency range, WR-42, at 18 GHz, 22 GHz, and 23.8 GHz. These frequencies were chosen because 18 GHz is the low end of the design range, 22 GHz is a popular remote sensing frequency and 23.8 GHz is the exact frequency of the first channel on ATMS. We chose to use only three frequency points as opposed to more for maximal accuracy. Measuring at more frequency points on the NIST waveguide radiometers requires more time between primary standard views and allows for increased measurement drift.

The WR-42 radiometer was set up in the anechoic chamber and the heat exchanger was connected for water circulation. The radiometer port reflectivities were measured and calibrated out using the sixport technique [81]. The loss of the extended waveguide section on the test port was calibrated out by measuring the mismatch ratio between two noise diodes on the cryogenic port and the device under test (DUT) port. A noise source 'check standard' is measured to confirm reliable calibration and compared to historical measurements of this check standard. We measured the target at a range of temperatures in order to follow the illumination efficiency (η_{IE}) extraction method of [32], to correct for spillover. We vary the temperature of the target between ambient room temperature, 296 K, to the maximum rated temperature of the circulator tubes of about 343 K (70 C). We make measurements at circulator bath set temperatures of 296 K, 305 K, 315 K, 325 K, 335 K, and 345 K. We then repeat the measurement at 345 K to calculate the effective blackbody brightness temperature using the illumination efficiency extracted from the previous measurements. This procedure is repeated at three distances, one extremely close distance with a very high illumination efficiency to minimize uncertainty, and two mid-field distances to demonstrate the distance dependence of the uncertainties; of both the blackbody itself, and the radiometer based traceability transfer technique. The distances measured were 0 cm, where the cone aperture was coplanar with the horn aperture, 40 cm and 60 cm separation between the two apertures.

A photograph of the WR-42 radiometer setup is shown in Figure 66. The linear fits of the mean PRT measured physical temperatures versus the radiometrically measured brightness temperatures (T_x) are shown in Figure 67. The uncertainties on T_x are plotted at the six temperature points, but fall within the marker symbol itself on the order of about 0.3 K. Table 8 shows the extracted illumination efficiencies and associated uncertainties at the three distances and frequencies. We see that at the 0 cm distance, as one might expect, we have very good coupling between the antenna power and the blackbody. The derived illumination efficiency for 0 cm and 22 GHz resulted in a value of 1.0051, a non-physical value, so this was corrected to 1, which was within the calculated standard uncertainty of 0.0056. At 60 cm we see that just over half of the total power into the horn comes from the blackbody. We show that higher illumination efficiency allows lower effective blackbody brightness temperature uncertainty, and provides lower reflectivity, and lower microwave emissivity uncertainty as shown in section VI.A.

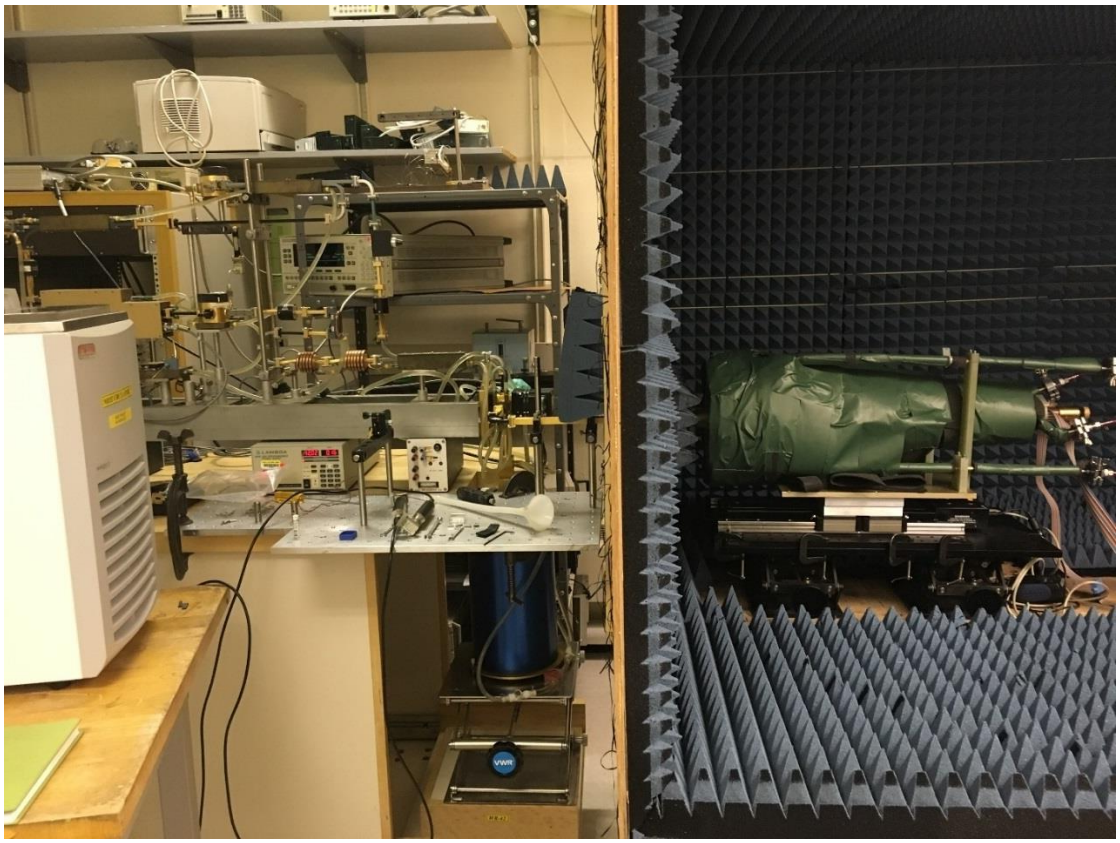

Figure 66: Photograph of NIST WR-42 radiometer setup with blackbody at closest distance in anechoic chamber

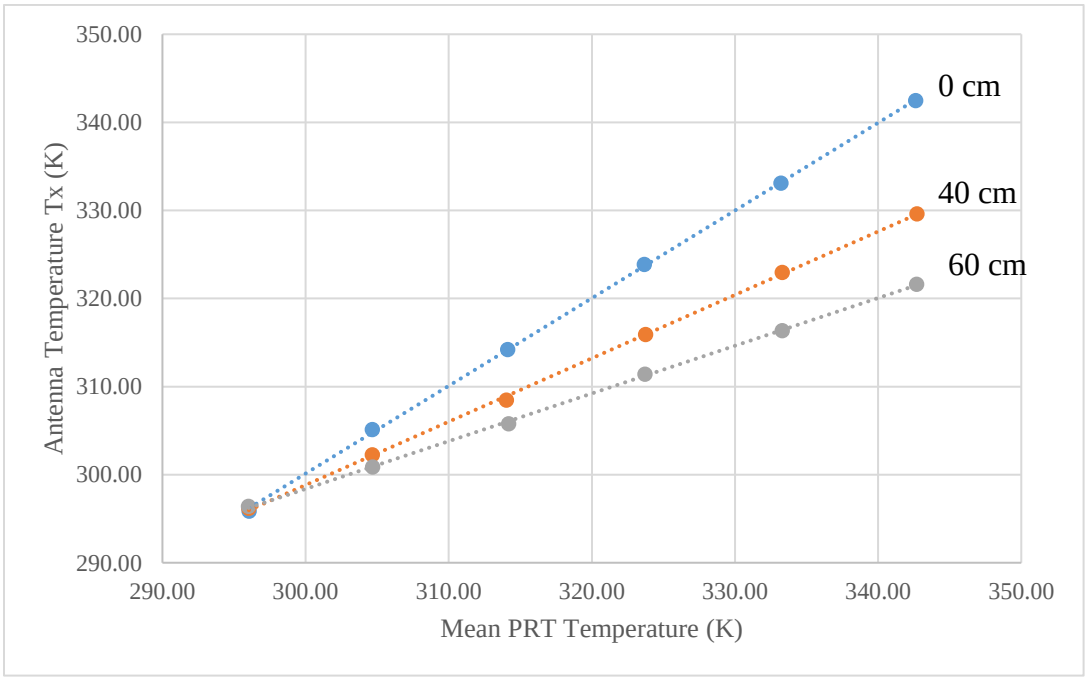

Figure 67: Linear fits for illumination efficiency extraction at different distances

Table 8: Radiometrically derived illumination efficiency values

18 GHz	Illumination efficiency η_{IE}	Illumination efficiency uncertainty $u_{\eta_{IE}}$
0 cm	0.9999	0.0082
40 cm	0.7273	0.0087
60 cm	0.5482	0.0078
22 GHz		
0 cm	1.0000	0.0056
40 cm	0.7459	0.0051
60 cm	0.5992	0.0052
23.8 GHz		
0 cm	0.9984	0.0071
40 cm	0.7507	0.0068
60 cm	0.6141	0.0071

After the illumination efficiencies were determined, an independent measurement was taken at the hottest target temperature of 345 K water-bath setting at each distance. The effective blackbody temperature is then solved for by inverting and substituting (30) into (28) to obtain [32],

$$T_{eff}^{bb} = \frac{1}{\alpha\eta_{IE}} T_x - \frac{1-\eta_{IE}}{\eta_{IE}} T_{phy}^{bg} - \frac{(1-\alpha)}{\alpha\eta_{IE}} T_{phy}^{ant} \tag{40}$$

where T_{phy}^{bg} is the physical temperature of the background. Note we have made the substitution $\tilde{T}_b^{bg} = (1-\eta_{IE})T_{phy}^{bg}$ to the form given in (28). All other notation has been described in section V.C. The physical temperature of the background is measured with 8 PRTs installed in the back wall of the chamber. By assuming that T_{phy}^{bg} is equivalent to the mean of the chamber PRTs, we assume a uniform background with an emissivity of 1. In the uncertainty quantification we inflate the associated uncertainty term $u_{T_{phy}^{bg}}$ by ten times, following the procedure of [32] to account for errors in this assumption. The radiometer-measured effective blackbody brightness temperatures should theoretically be equivalent to the calculated target brightness temperature values. We also plot the mean target PRT temperatures for reference as this is the typical way physical temperature is related to brightness temperature. The calculated effective blackbody brightness temperature values use the simulated temperature field discussed and plotted in section V.C.. Comparisons of

the radiometrically measured and numerically calculated effective blackbody brightness temperatures are provided in Figure 68, Figure 69, and Figure 70 for 18 GHz, 22 GHz, and 23.8 GHz respectively. Figure 71 provides a clearer visualization of the polyethylene insulated case at the closest distance, 1 cm. We see that the measured effective brightness temperature has error bars larger than the simulated brightness temperature uncertainty. This was a key motivating factor behind the use of a primary standard source rather than the standard radiometer for free-space brightness temperature calibration. We see the closest agreement between the measured and calculated result at the closest distance where the measurement uncertainty is the lowest. At further distances, when the illumination efficiency is lower, the background contributes more to the measured radiometer temperature, T_x, causing a larger uncertainty in the measured effective blackbody brightness temperature. When the illumination efficiency is small, thus large amounts of spillover, the large uncertainty and temperature gradients in the background inflate the total uncertainty regardless of the uncertainty in the blackbody brightness temperature. In summary, no matter how well characterized the blackbody source is, if you have a large contribution from an uncertain background, the resulting calibration will have a high uncertainty. Following this logic, we see the importance of having a high illumination efficiency, or good coupling between antenna and blackbody, when attempting to minimize calibration uncertainty. In our measured data we see the same trend identified in [32] where the effective blackbody brightness temperatures decrease with distance. The measured and calculated values for the polyethylene insulated target are in agreement to within their respective error bounds, but there appears to be a systematic effect in the extraction method. This decrease over distance appears to be larger than the calculated effect of higher antenna weighting on the cooler aperture of the cone. In other words, the measured effective blackbody brightness temperature decreases with distance more quickly than the calculated effective blackbody brightness temperature, closely resembling the trend seen in [32]. The non-insulated target measurements appear to agree more closely with measurements at farther distances, such as at 60 cm, we see close agreement between the calculated and measured effective blackbody temperature.

The error bars of the calculated effective blackbody brightness temperature with no polyethylene insulation do not fall within the error bars of the measured values at the closer distances 0 cm and 40 cm. The error bars show only one standard uncertainty, so the possibility of random error is not out of the question, but there could be some additional uncertainty that was not considered. When the target is not insulated, the temperature of the absorber surface inside the

cone is much more sensitive to environmental conditions and to the emissivity of the absorber surface. The thermal model assumed that circulating fans would maintain a steady state temperature inside the chamber of approximately 296 K, whereas we saw temperatures as high as 301 K inside the chamber when running the heated target. The hotter background not only contributes to the spillover brightness temperature but creates less radiative heat loss from the cone due to lower temperature difference between the surfaces.

We have successfully verified that at close distance, or at high illumination efficiency, the calculated effective blackbody brightness temperature agrees to within the measureable uncertainty of the radiometric effective blackbody brightness temperature, and we believe the standard uncertainty error bars calculated by the Monte-Carlo simulation to be reasonable. Future studies will aim to quantify the infrared emissivity of the anechoic chamber material, and also investigate the effect of the circulation fans. We also plan to experiment with the use of a reflective shroud to maximize illumination efficiency at larger distances, such as has been done with ATMS in the past.

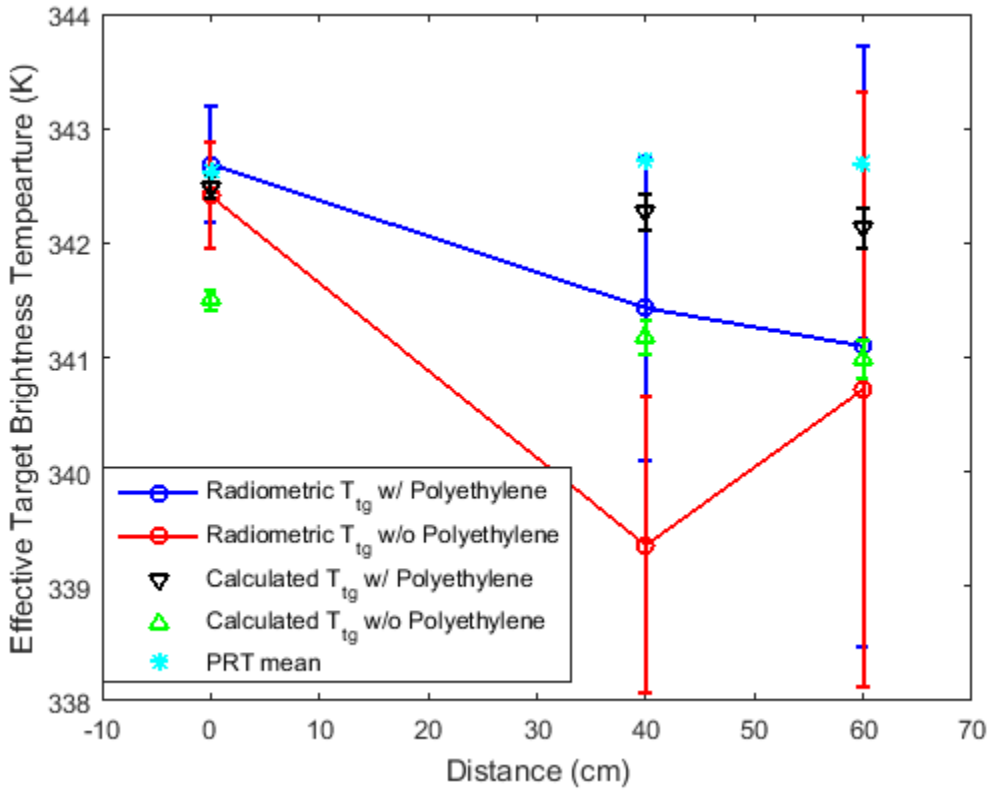

Figure 68: Effective blackbody brightness temperature versus distance at 18 GHz. Error bars correspond to one standard uncertainty for the associated parameters.

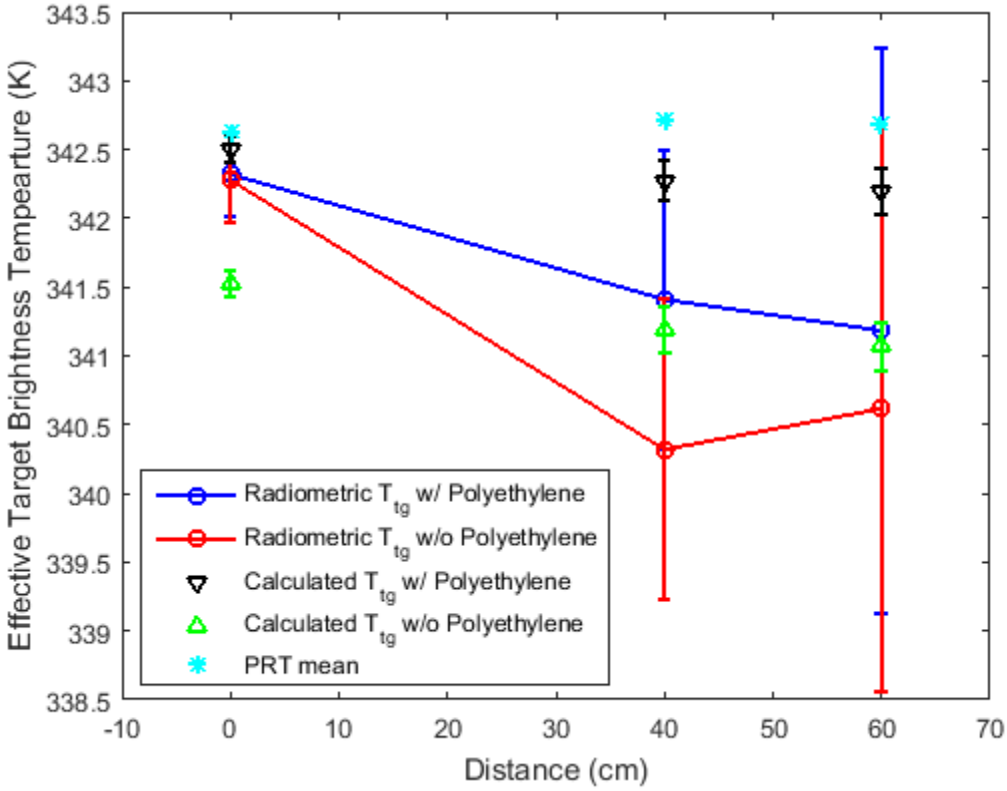

Figure 69: Effective blackbody brightness temperature versus distance at 22 GHz. Error bars correspond to one standard uncertainty for the associated parameters.

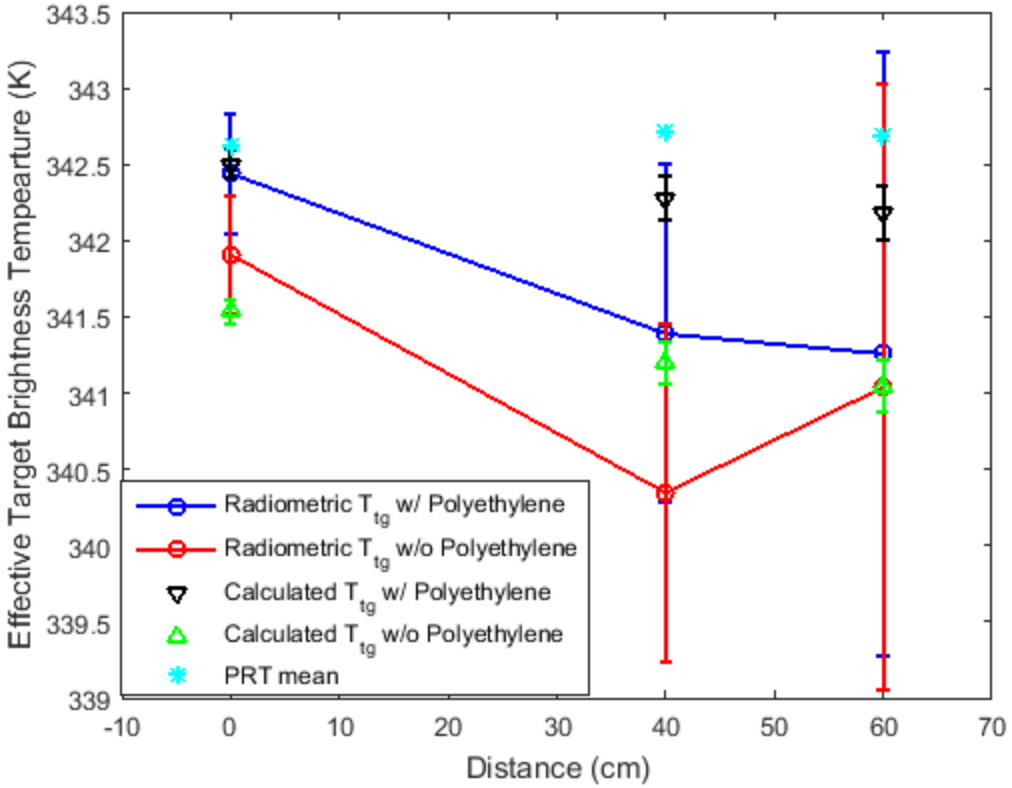

Figure 70: Effective blackbody brightness temperature versus distance at 23.8 GHz

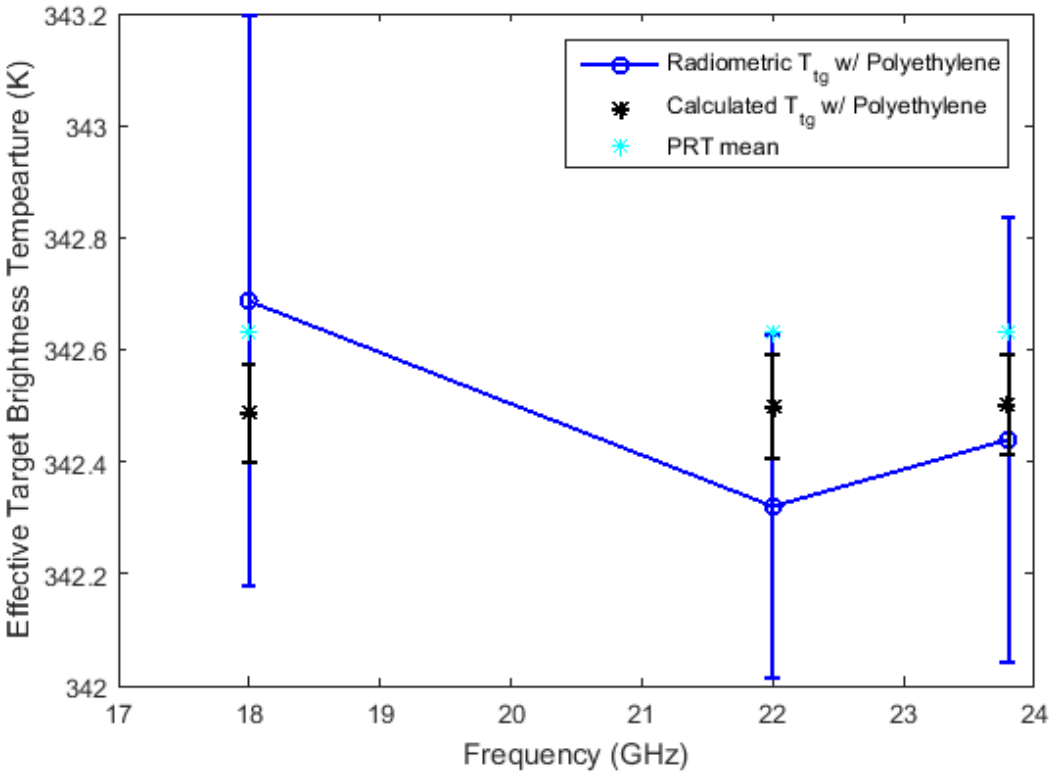

Figure 71: Effective blackbody brightness temperature versus frequency at 1 cm separation distance for polyethylene insulated target

C. Thermal Infrared Imaging

The blackbody was measured with a radiometric thermal infrared imager to verify the thermal models and calculate the emissivity of the Stycast absorber and polyethylene foam. In collaboration with Ball Aerospace, we used the Ball Experimental Sea Surface Temperature (BESST) radiometer [82] to view the heated blackbody inside of the anechoic chamber.

The BESST has three infrared filters across a sensor of 256 by 324 pixels. We wanted a consistent image of the cone in one infrared wavelength, so we attempted to place the target in a position that would allow the full 22 cm diameter to be measured by the center 12 μm channel. To achieve this, we had to move the target to the furthest position in the back of the anechoic chamber, and place the BESST camera slightly behind the window into the chamber. The lens of the BESST camera was aligned into the cone axis by centering the alignment laser on the back of the unit and then centering the image of the cone in the sensor's field of view.

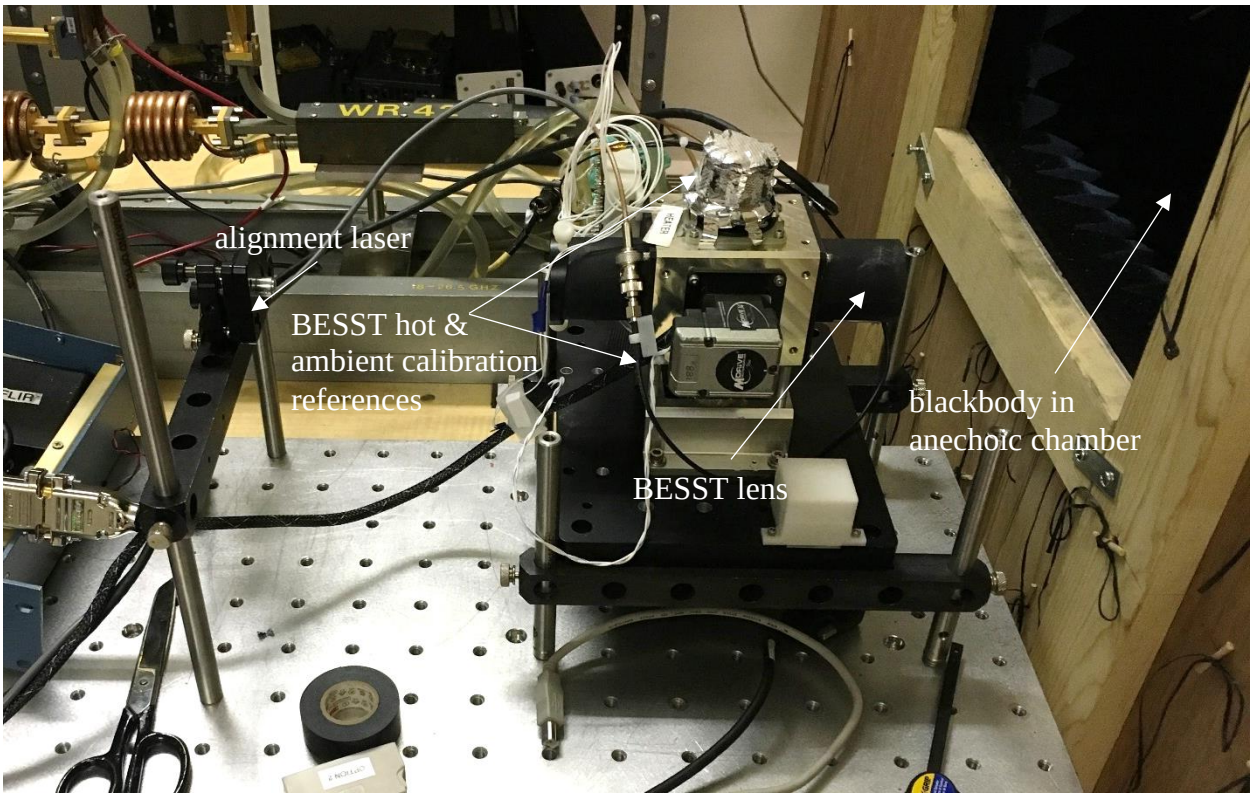

Figure 72: Photograph of BESST infrared imaging radiometer setup at the window to the anechoic chamber for IR imaging

By measuring the infrared radiation from the cone we hoped to characterize the temperature gradients and confirm the numerical result of Figure 12. From the microwave perspective, we are interested in the temperature of the absorber that is actually radiating as an approximate blackbody. In the design, this absorber is covered with the polyethylene foam that is transparent to microwaves but opaque to infrared. We quickly see the difficulty in measuring the infrared temperature of something behind an opaque sheet. We are left with two options to experimentally verify the temperature field on the interior of the cone. First is to remove the polyethylene and consider convection and radiation directly on the Stycast absorber. Second is to measure the temperature on the surface of the polyethylene insulation and compare this to the modeled polyethylene temperature. A challenge in using the cone's infrared radiation to accurately characterize its physical temperature is the uncertainty in the infrared emissivity. The target was designed to have high emissivity in the microwave operating frequency range but this does not necessarily say anything about its infrared emissivity. Because of the uncertainty in the infrared emissivity, the images proved useful for visualizing the temperature gradients over the cone but did not provide an absolute calibrated image of the blackbody's physical temperature.

We know from the result of many iterations of simulations that the maximum temperature of the cone at the apex is very close (±0.01 K) to the temperature of the copper backside that we monitor with the PRTs. We can use this information to solve for the approximate emissivity of the Stycast absorber. The initial BESST camera data was provided by Ball Aerospace as an array of calculated temperatures using rough estimates of the surface emissivities of 0.1 for the polyethylene foam [83] and 0.9 for the Stycast absorber [84]. These values originated from questionable sources and were listed for materials "polyethylene" and "black epoxy paint", not specific to closed cell foam or the specific epoxy type. The raw data were far from realistic and required some re-calibration. The measured infrared radiances were adjusted so the maximum measured radiance corresponded to the maximum known temperature at the apex of the cone. According to the Stefan-Boltzmann law and the greybody approximation, the radiance relates to emissivity and temperature as,

$$j = \varepsilon\sigma T^4 \tag{41}$$

where j is radiance, ε is infrared emissivity, σ is the Stefan-Boltzmann constant, and T is physical temperature. We define a proportional term j/σ and call it P. We find the measured P using the input emissivity estimates and calibrated temperature array,

$$P_{meas} = \varepsilon_{rough}(T_{meas})^4, \tag{42}$$

where P_{meas} is proportional to the measured radiances, ε_{rough} is the rough estimate of emissivity, either 0.1 or 0.9 for the polyethylene coated or bare Stycast cases respectively, T_{meas} is the array of measured temperatures. We find the effective calculated emissivity by,

$$\varepsilon_{calc} = \frac{\max(P_{meas})}{(T_{\max})^4} \tag{43}$$

where ε_{calc} is the calculated emissivity, and $T_{\max}$ is the known maximum physical temperature of 342.75 K at the cone apex. The corrected temperature array is then solved using the same relation,

$$T_{corr} = \left(\frac{P_{meas}}{\varepsilon_{calc}}\right)^{1/4} \tag{44}$$

where T_{corr} is the corrected infrared temperature array. The calculated emissivities for the polyethylene foam and bare Stycast absorber were 0.0638 and 0.5746 respectively. This emissivity for the CBI-loaded Stycast epoxy seemed initially too low, but after further digging, a study of similar materials showed measured infrared emissivities in the range 0.419 to 0.650 for CBI loaded epoxy-polyurethane resins treated with different annealing processes [85]. These

calculated emissivity values were used to simulate the physical temperature on the Stycast surface for the simulations shown in Figure 54 and Figure 55.

We present the corrected T_{corr} array for the full BESST sensor in Figure 73 and Figure 74 for the insulated and non-insulated cases respectively. The seam in the polyethylene insulation sheet can be seen in Figure 73 near the bottom of the cone. The appearance of this seam suggests that the insulation is not sufficiently blocking the radiation loss from the Stycast along this line, and we expect that the physical temperature of the Stycast surface is in fact cooler than what we would expect from simulation with a uniform polyethylene layer. In the future, the polyethylene will be attached to the Stycast in such a way that air gaps along the polyethylene seam are minimized.

We see that the background temperature appears much hotter in the infrared images than the PRT measured background temperature of about 299 K. This hot background is hypothesized to be partially due to IR radiation emitted from the hot target and reflected off of the chamber. The anechoic chamber is designed to be absorbing in microwave but the IR emissivity of the carbon-impregnated foam anechoic pyramids is unknown. If we assume no transmission into the anechoic chamber foam, we can calculate the reflectivity required to provide an infrared temperature of about 336 K. Assuming the true temperature of the anechoic chamber to be 300 K and the emissivity to be one minus the reflectivity, this corresponds to a reflectivity of 0.85 and emissivity of 0.15. The temperatures measured here are hotter than the hot calibration target within the BESST instrument, necessitating extrapolation rather than interpolation of the calibration curve. We expect there may be some error in the IR results due to this calibration extrapolation and non-linearity of the detector. Our collaborators confirmed that the temperatures under investigation here could in fact be outside the linear range of the BESST camera detector thus causing a decrease in the dynamic range.

We compare the FEM modeled temperature field with the IR measured temperature for the target without Stycast insulation. We interpolate the IR measured temperature field of Figure 74 onto the same 512 by 512 grid used in the effective blackbody brightness temperature calculation. The difference between the simulated and measured temperatures are calculated and plotted as a contour in Figure 76. We see agreement at the center of the cone (radius = 0) because this is where we assigned the IR data to take on the value 342.75 K, also the maximum of the simulated data.

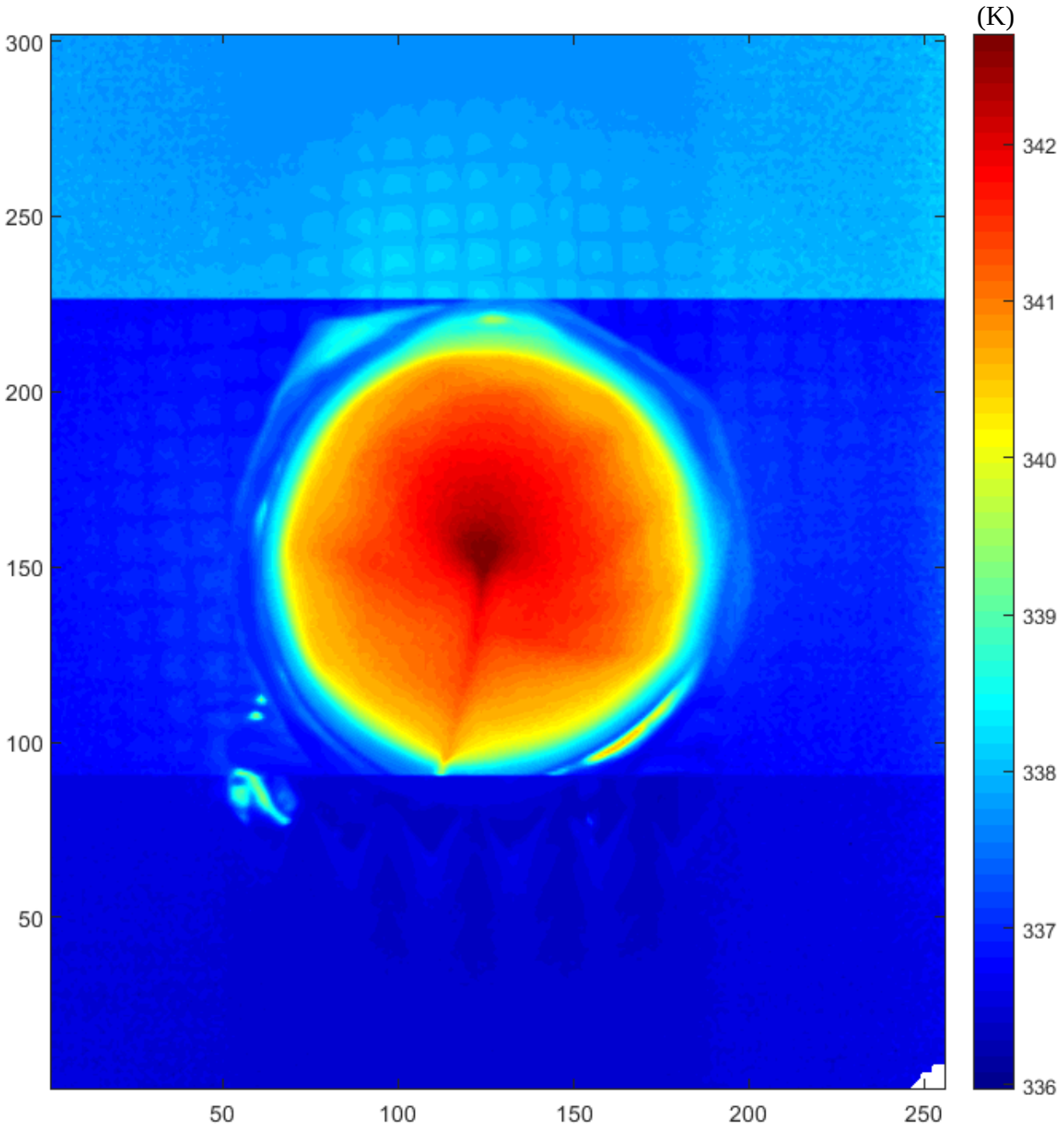

Figure 73: Corrected infrared image of polyethylene insulated target. Colorbar units in K, axis ticks are pixel numbers. The horizontal lines across the image are a result of the three different filters.

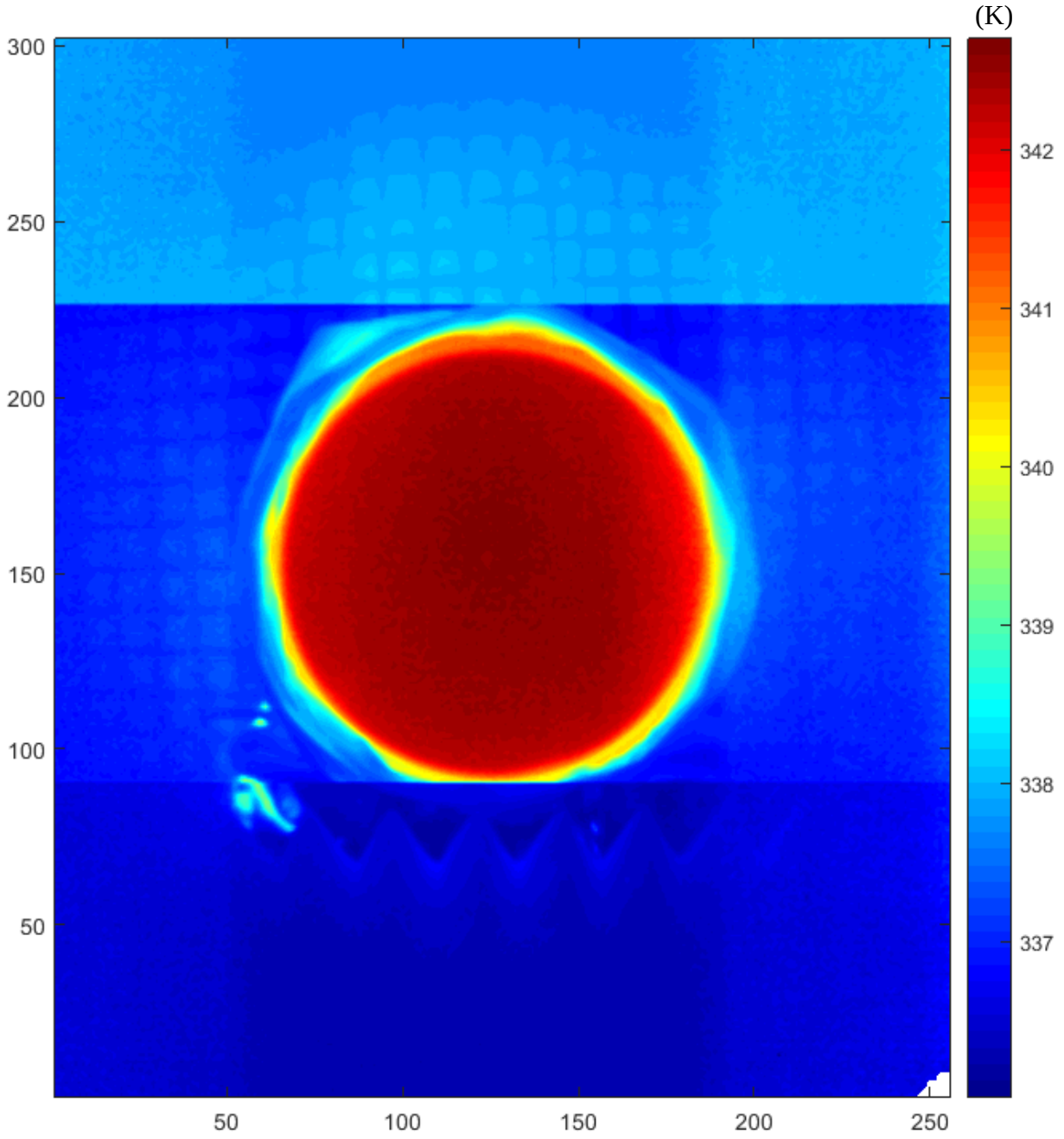

Figure 74: Corrected infrared image of non-insulated target. Colorbar units in K, axis ticks are pixel numbers. The horizontal lines across the image are a result of the three different filters.

Figure 75: Photograph looking into polyethylene insulated blackbody. The seam in the polyethylene can be seen towards the bottom of the cone.

We see do not see a quick drop-off in temperature in the measured data like we see in the simulated data. The IR measured data also remains much hotter near the aperture of the cone where we see a quick drop-off in the simulated temperature. The majority of the surface area of the cone shows temperature difference between IR measured and simulated on the order of about 1.25 K. This magnitude of temperature bias is believed to be within the measurement uncertainty of the IR camera near 340 K. In addition to non-linearity of the IR detector, there are several other possible explanations for the offset bias. The first and perhaps most obvious difference is the environmental differences between simulation and measurement. The simulation assumed forced convection in the form of circulation fans in order to reach a converged steady-state solution. The fans were never actually installed, leaving the cone to only free convection, which could have led to a hotter absorber surface temperature. Secondly, when we performed the recalibration of the IR data we assumed that the hottest temperature of 342.75 K inside the apex of the cone was clearly resolvable as an independent pixel in the image. If in fact the resolution was not this fine, this hottest point would have been washed out along with cooler temperatures, causing the hottest recorded pixel to be something less than the assumed 342.75 K. The combination of these error contributions is estimated to be larger than 2 K suggesting that we cannot state with any significance whether the IR data and simulation results agree. Nevertheless, the IR measurements proved useful for solving

the approximate infrared emissivity of the Stycast and polyethylene, and for visualizing the non-ideality in the polyethylene seam.

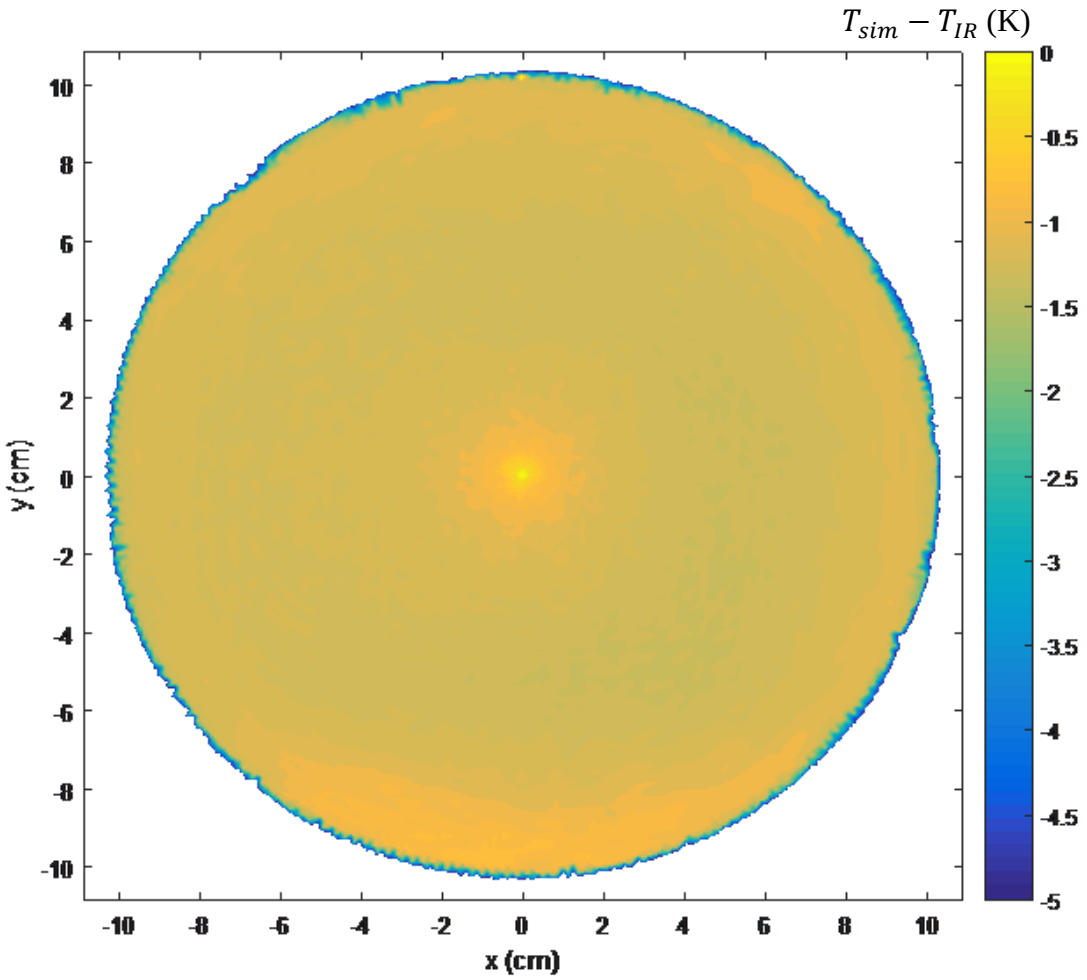

Figure 76: Contour of temperature difference of simulated minus IR measured temperature in units of Kelvin

D. Temperature Cycling

In the preliminary experimental results presented here we circulated water through the copper heat exchanger and were limited to temperatures of 70 C due to the tubing available. Due to hardware malfunctions we also had to rely on a lower power circulator than originally planned. We plan to improve many of these aspects of the temperature control system by circulating Novec engineering fluid with a higher thermal conductivity than water, and by using a 1600 Watt heating circulator rather than an 800 Watt circulator. The insulation on the outside of the copper can also

be vastly improved, we plan to have a custom Styrofoam casing 3D printed to fit snugly around the helical copper structure.

We present the temperature results from the variable temperature radiometric measurements used to perform the illumination efficiency extraction. The 12 PRTs installed in the large target have been named with a scheme to help identify their location. The number 3, 6, or 9 refers to the radius or distance from the cone axis in cm, and the letters, L, R, T, and B, refer to left, right, top, bottom respectively. The left and right directions are relative to the antenna looking into the cone. The recorded temperatures for the 6 set points are shown in Figure 77, and the full heating curve from room temperature to about 342 K is shown in Figure 78.

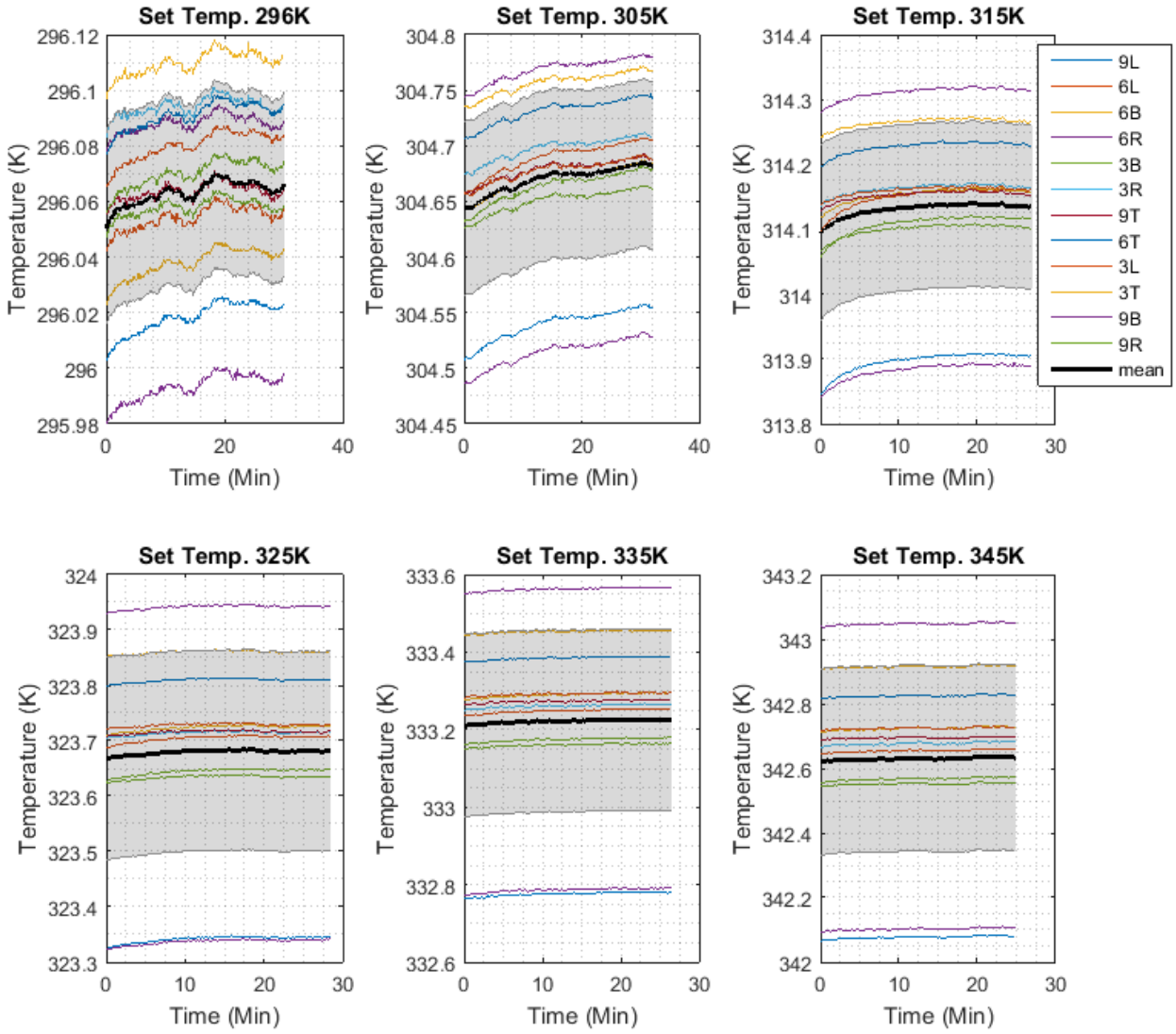

Figure 77: PRT measured temperatures of polyethylene insulated target during near-field illumination efficiency extraction measurements

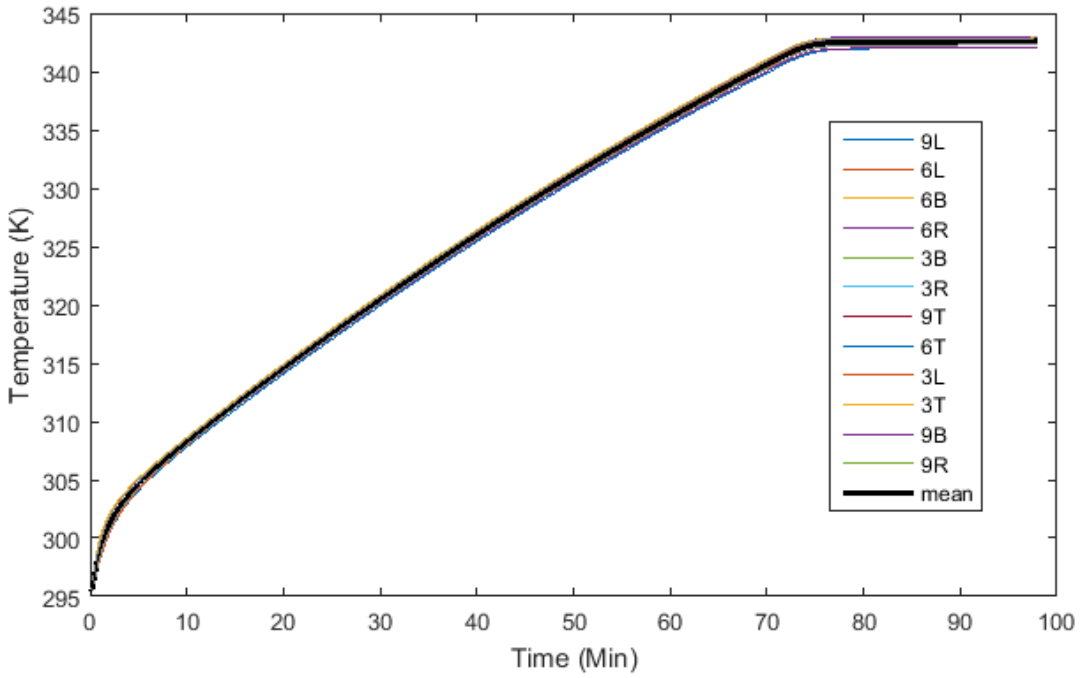

Figure 78: PRT measured temperatures of polyethylene insulated target during heating to 342 K

We observe in Figure 77 that at 345 K set-temperature there is almost 1 K spread between the PRTs attached to the copper backside of the cone. This is larger than what we expected from simulation. We examined the temperature gradient along the copper cone in the full CAD thermal model discussed in section IV.D.. We predicted only a 0.25 K gradient in the copper cone based on the full CAD FEM simulation but this simulation does not include convection and assumes a perfectly insulated copper backside. We expect that by improving insulation on the outside of the copper we can reduce this spread of measured temperatures. We also suspect that there is some variability in thermal contact to the copper due to imperfect installation of the PRTs.

We found that it takes approximately 90 minutes to heat the target from ambient room temperature to 342 K. This heating curve is close to linear after about 305 K so heating times to hotter temperatures can be extrapolated while providing a few extra minutes for settling time. We plan to use a circulator with a 1600 Watt heater in the future as opposed to the 800 Watt circulator used in this experiment. We expect the more powerful circulator to reduce the heating times by about half. The use of higher thermal conductivity engineering fluid instead of water may also help evenly distribute the temperature in the copper. We also expect a much smaller spread on the PRT readings in the vacuum chamber when convection is eliminated.

VII. ATMS PRELAUNCH CALIBRATION

There are many specifics regarding how the conical blackbodies will be used to transfer traceability to the ATMS instrument, or to any other microwave radiometer. We address some of these procedural concerns in this section. Many of the remaining programmatic requirements, measurement procedures, and data processing details will be discussed and determined with JPSS and Northrop-Grumman in the future.

The two conical blackbodies will replace what were referred to as the variable temperature, or scene temperature, targets in the instrument level thermal-vacuum ground-testing and calibration. The radii of the targets were designed to approximately match the minor axis of the previously used elliptical targets. The shrouds will have to be redesigned to maximize the illumination efficiency of the conical targets. The time on target will be slightly reduced due to the smaller dimension along the scan axis, but it was impractical to attempt a non-circular cone design, and we required a polarization independent source.

The pre-launch ground calibration of ATMS is used to correct for non-linearity in the detectors [86]. This method requires multiple temperature points of the target to be measured in order to determine the non-linearity as a function of brightness temperature between LN2 temperature and about 330 K. The non-negligible non-linearity of the ATMS detector means that the illumination efficiency extraction method of [32] is rendered infeasible. The illumination efficiency extraction method assumes a linear detector and uses the slope of the physical temperature versus radiometric brightness temperature to determine the illumination efficiency, or spillover. We have shown that at close distances, the illumination efficiency is unity for all practical purposes. The ATMS calibration distance will not be 0 cm, but we plan to add a reflective shroud, or baffle, to eliminate any background contributions and force the illumination efficiency to one. A similar concept has been applied to the ATMS pre-launch calibration in the past, but we will carefully design this shroud to ensure it is truly and solely reflecting the blackbody brightness temperature and not creating any standing waves such as those discussed in [27], or any other coupling effects. The illumination efficiency can be confirmed by simulation or from measured antenna pattern data with a simple integration of the antenna pattern, such as [87]. The conical blackbodies will still be used to perform variable temperature non-linearity correction such as in the original procedure.

We discuss a proposed method to transfer traceability from the conical calibration load to the internal calibration source in the ATMS instrument. There are numerous ways this can be achieved, but we believe this method minimizes additional uncertainty contributions. We will use the variable nature of the conical blackbody to essentially calibrate the PRTs on the internal ATMS target. Before the two-point Y-factor calibration that allows the raw counts to be transferred into units of brightness temperature, we make measurements in raw radiometer counts, the unprocessed units directly out of the analog to digital conversion on the detector. The reason we perform the transfer in raw units is that once the two-point calibration has been implemented there are already four corresponding uncertainty terms contributing to each radiometer measurement. The uncertainty associated with the brightness temperatures of the hot and cold sources, and the statistical errors associated with the two raw radiometer measurements themselves. We propose to measure the raw radiometric counts of the ATMS internal target and then switch to measure the conical target. We will adjust the set-point temperature of the conical target in a closed-loop feedback manner such that we obtain equivalent raw count measurements on both the internal and conical targets. The flow chart in Figure 79 describes this process.

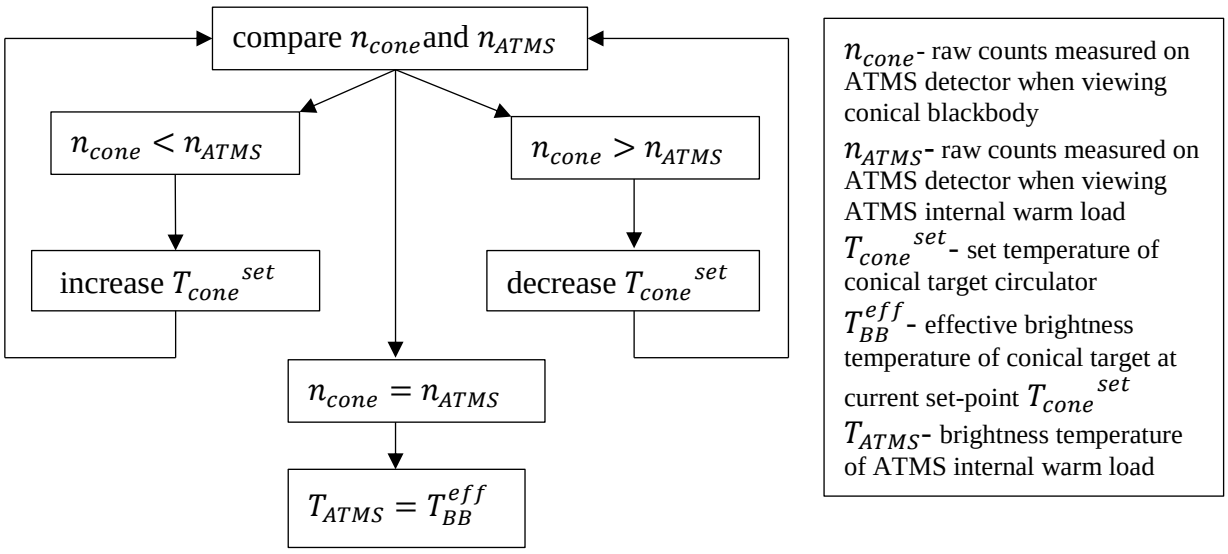

Figure 79: Simplified flow chart describing closed-loop process to equate raw radiometric measurement of conical blackbody standard with ATMS internal target. Terminology is described in the legend to the right.

The diagram of Figure 79 is simplified because in practice it may not be possible to obtain exactly the desired outcome $n_{cone} = n_{ATMS}$ due to random variation in the detector and temporal gain drift between the two looks. In practice both n_{cone} and n_{ATMS} will be means over some

nominal integration time, and the equivalence will be within some small but finite tolerance value. This tolerance will be a contributor to the resulting uncertainty of the transferred standard, so it is preferable to minimize this, with the tradeoff of taking more time to complete the calibration. The method will also require some wait time for thermal settling and equilibrium between each set-temperature change. It is possible that each channel needs to be tuned independently if there is considerable frequency dependence in the ATMS internal load brightness temperature. If the internal load has high broadband emissivity, the frequency dependence shouldn't be an issue, but this process will be a good check of the ATMS internal calibration load performance. The resulting ATMS internal warm load brightness temperature T_{ATMS} can be used to derive an offset, or transfer function, to the measured physical temperature on the backside of the internal load. If the warm load will experience a large range of temperatures on orbit, it may be worthwhile to check the consistency of the offset as a function of temperature by performing the transfer standard tuning process at the temperature extremes of the internal warm load.

The relatively slow process of tuning the conical standard temperature in the raw units of the radiometer allows the standard to be transferred at the lowest level, with the least amount of possible additional uncertainty sources. The process will be automated as a closed-loop algorithm and tested to minimize the time required. Vacuum chamber time is not cheap and efficiency will be key. If the two-point Y-factor calibration of the warm load and cold-space mimicking target were performed before transferring the standard, in units of brightness temperature, the error in both the warm and cold loads would already be propagating through to the gain and offset quantities used to convert the measurement to brightness temperature. Presumably if there are temperature gradients in the warm and cold targets, the cold target has warmer pyramid tips than the measured backside temperature, and the warm target has cooler pyramid tips than the measured backside, in effect this creates an overestimation of the slope in Kelvin per counts, or the calibration gain. If this calibrated gain was then used to interpolate a brightness temperature of the conical target at a different brightness temperature, the calibration error is propagating into the transference process.

The tuning method has eliminated the need to know the Kelvin per counts gain beforehand, and directly transfers the standard in units of raw counts.

VIII. DISCUSSION

The thorough and deliberate design of the NIST microwave blackbody resulted in a predictable and effective final product. Each additional requirement contributed unforeseen hurdles and unexpected modifications to the design but ultimately provoked a unique and functional solution. The high degree of coupling between the electromagnetic and thermal design necessitated an iterative design. This process made it difficult to present the design in a chronological or sequential manner. The following discussion examines and summarizes some examples of the challenges met in the process of designing and verifying the NIST microwave blackbody.

A parameter in the design process exemplifying the required iterative analysis was the thickness of the absorber. A thicker absorber provides lower reflections, or higher emissivity, but conversely increases physical temperature gradients between the apex and aperture of the cone, and between the temperature-controlled copper backside and the radiating absorber surface. The thickness of the absorber thus required iterative electromagnetic and thermal modeling to determine the minimal absorber thickness that would meet electromagnetic requirements. The final 5 mm total thickness Stycast with 3 mm polyethylene foam insulation was determined to be the sweet-spot in this design tradeoff.

Yet another example of this physical coupling in the design was the decision to separate the Stycast and copper cones to relieve internal stress. Due to the higher coefficient of thermal expansion of the Stycast relative to copper, the bonded contact between these materials generated large amounts of internal stress at cold temperatures. The decision to separate the absorber cone from the copper cone prompted a creative mechanical design solution, but introduced additional uncertainty in the thermal contact between the two materials.

Other examples of confusions and lessons learned were: the numerical error of simulating and integrating small reflections with the finite element method, resonances corrupting measurements in the two-port electromagnetic material property determination method, and the important role of Stycast and background (anechoic chamber) infrared emissivity. The sensitivity of both the microwave emissivity and physical temperature to small changes in the design created a challenging problem with a rewarding, and seemingly unique, solution.

The use of the polarization independent conical geometry, along with the design of a new microwave absorber has allowed for broadband performance ranging between 18 GHz up to, and

likely above, 220 GHz. The blackbody was designed to be capable of reaching temperatures between about 77 K and 350 K. Two conical devices have been manufactured, the larger has a radius of 10.85 cm and the smaller cone with a 6.8 cm radius. Both cones have been manufactured with the same absorber layering structure so they should have similar electromagnetic performance, but the smaller cone will experience increased edge scattering and diffraction from the aperture below about 50 GHz.

The design and electromagnetic verification has demonstrated the accuracy of the geometric optics technique at microwave frequencies for electrically large geometries. This method is fast and computationally inexpensive allowing efficiency optimization of the absorber design.

The use of a thin layer, 3 mm, of polyethyelene foam is shown by simulation to reduce temperature gradients between the blackbody's apex and aperture, as well as increasing the overall temperature on the radiating surface of the Stycast absorber for the heated target case.

The proposed procedure of transferring traceability in raw uncalibrated radiometer 'counts' eliminates uncertainty terms from other pre-launch references, such as a cold-space mimicking cold target. The closed-loop, raw counts, transfer method will determine the traceable brightness temperature of the internal flight load, or calibration reference. This traceable point along with the well-characterized cold-space brightness temperature may then serve as two traceable calibration points for in-flight radiometer calibration.

Initial experimental verification has indicated that the conical blackbody performs as modeled and within the Monte-Carlo predicted uncertainty. Many terms were taken as 'worst-case' quantities leaving open the possibility to decrease the effective blackbody brightness temperature uncertainty. Additional measurements in the future are expected to reduce the simulated uncertainty by lowering uncertainty on the input parameters, physical temperature, microwave emissivity, and normalized antenna pattern. With greater knowledge of the IR emissivity of the Stycast and polyethylene foam, in addition to characterized Stycast-to-copper thermal contact, the physical temperature uncertainty can be reduced. These quantities can be determined through calibrated IR imagery along with temperature monitoring of the Stycast surface. The uncertainty of the blackbody microwave emissivity can also be reduced. Experimental measurement of the BRDF will allow empirical calculation of the emissivity rather than relying on worst-case emissivity estimates justified by monostatic reflectivity measurement. Finally, the normalized antenna pattern uncertainty can be reduced on a case-to-case basis by

accurate measurement or simulation of the pattern. This term has the smallest effect on the resulting brightness temperature uncertainty, and will vary across each calibration, so future focus will be placed on reducing the physical temperature and microwave emissivity uncertainty terms.

IX. CONCLUSION

The lack of traceability among passive microwave instruments has long plagued the remote sensing community, and the accuracy of combined data products and long-term trends has suffered. Inter-calibrations and re-calibrations based on earth reference locations or simultaneous nadir overpasses have helped, but the resulting data still lacks a quantifiable absolute uncertainty traceable to a primary reference [9]. NIST initially demonstrated traceability based on free-space extrapolation of its standard microwave radiometers [32], but the achievable uncertainty of about ±0.7 K was less than desirable for the majority of microwave-based data products. The design and verification of the high-performance conical microwave blackbody introduced in this thesis demonstrates the ability to pre-launch calibrate a radiometer's internal calibration reference, operating at a large range of earth remote sensing pertinent frequencies, to within ±0.11 K of the primary NIST reference source.

If operational instruments begin the practice of obtaining pre-launch calibration and NIST microwave brightness temperature traceability, the long-term quality of environmental data records will be improved. Traceable microwave brightness temperature will allow meaningful studies between IR and microwave temperatures. The reliance on re-analysis and re-calibration techniques will be eased, and inter-satellite comparisons will be capable of providing quantified and traceable brightness temperature uncertainty.

X. WORKS CITED

[1] https://en.wikipedia.org/wiki/Black_body

[2] Gu, D., D. Houtz, J. Randa, D.K. Walker, "Realization of a standard radiometer for microwave brightness-temperature measurements traceable to fundamental noise standards", Proc. of IEEE Int. Geoscience and Remote Sensing Symposium, Munich, July, 2012.

[3] Macelloni, G., "L-band characterization of Dome-C region using ground and satellites data" Proc. of IEEE Int. Geoscience and Remote Sensing Symposium, Melbourne, July 2013.

[4] Macelloni, G. *et al*., "Ground-Based L-Band Emission Measurements at Dome-C Antarctica: The DOMEX-2 Experiment," in *IEEE Transactions on Geoscience and Remote Sensing*, vol. 51, no. 9, pp. 4718-4730, Sept. 2013.

[5] Alsweiss, S.O., W. L. Jones, "Suitability of the amazon rain forest as an on-orbit, microwave radiometric calibration target," *Proc. of IEEE SoutheastCon*, Richmond, VA, 2007, pp. 111-115.

[6] Mo, T., "Diurnal Variation of the AMSU-A Brightness Temperatures Over the Amazon Rainforest," *IEEE Transactions on Geoscience and Remote Sensing*, vol. 45, no. 4, pp. 958-969, April 2007.

[7] Changyong Cao, Fuzhong Weng, M. Goldberg, Xiangqian Wu, Hui Xu and Pubu Ciren, "Intersatellite calibration of polar-orbiting radiometers using the SNO/SCO method," Proceedings. 2005 IEEE International Geoscience and Remote Sensing Symposium, 2005. IGARSS '05., 2005, pp. 4.

[8] S. Brown, "Maintaining the Long-Term Calibration of the Jason-2/OSTM Advanced Microwave Radiometer Through Intersatellite Calibration," IEEE Transactions on Geoscience and Remote Sensing, vol. 51, no. 3, pp. 1531-1543, March 2013.

[9] Zou C.Z., Wang W. "Intersatellite calibration of AMSU-A observations for weather and climate applications" Journal of Geophysical Research, vol. 116, 2011.

[10] "IPCC Fourth Assessment Report: Climate Change 2007" Chapter 1, Section 1.2, "The Nature of Earth Science". https://www.ipcc.ch/publications_and_data/ar4/wg1/en/ch1s1-2.html

[11] Datla, R.U., M.C. Croarkin, A.C. Parr, "Cryogenic Blackbody calibrations at the National Institute of Standards and Technology low background infrared calibration facility" J. of Research of the National Institute of Standards and Technology, Vol. 99, No. 1, Feb 1994.

[12] Ohno, Y. "NIST measurement services: photometric calibrations," NIST Special Publication 250-37, Jul 1997. http://www.nist.gov/calibrations/upload/sp250-37.pdf

[13] Arp, U., et al., "Sychrotron radiation based irradiance calibration from 200nm to 400nm at SURF III" J. of Applied Optics, Vol. 46, Jan 2007, pp. 25-35.

[14] Datla, R., Emery, W. et al. "Stability and accuracy requirements for passive satellite remote sensing instrumentation for global climate change monitoring" Post-Launch Calibration of Satellite Sensors, ISPRS Book Series vol. 2. London 2004.

[15] Eymard, L., E. Obligis, Ngan Tran, F. Karbou and M. Dedieu, "Long-term stability of ERS-2 and TOPEX microwave radiometer in-flight calibration," in IEEE Transactions on Geoscience and Remote Sensing, vol. 43, no. 5, pp. 1144-1158, May 2005.

[16] Ruf, C.S., "Detection of calibration drifts in spaceborne microwave radiometers using a vicarious cold reference," in IEEE Transactions on Geoscience and Remote Sensing, vol. 38, no. 1, pp. 44-52, Jan 2000.

[17] Piepmeier, J.R., L. Hong and F. A. Pellerano, "Aquarius L-Band Microwave Radiometer: 3 Years of Radiometric Performance and Systematic Effects," in IEEE Journal of Selected Topics in Applied Earth Observations and Remote Sensing, vol. 8, no. 12, pp. 5416-5423, Dec. 2015.

[18] Bell, W., S. DiMichele, P. Bauer, T. McNally, S.J. English, N. Atkinson, F. Hilton, J. Charlton, "The radiometric sensitivity requirements for satellite microwave temperature sounding instruments for numerical weather prediction" *J. Atmosphereic and Oceanic Tech.*, vol. 27, Mar. 2010, pp. 443-456.

[19] B. Yan, F. Weng, J. Derber, "Assimilation of satellite microwave water vapor sounding channel data in NCEP global forecast system (GFS)," *The 17th Annual International TOVS Study Conference (ITSC-17)*, Apr 2010, pp. 1-15.

[20] É. Gerard, F. Karbou and F. Rabier, "Potential Use of Surface-Sensitive Microwave Observations Over Land in Numerical Weather Prediction," in *IEEE Transactions on Geoscience and Remote Sensing*, vol. 49, no. 4, pp. 1251-1262, April 2011.

[21] R. W. Saunders, T. A. Blackmore, B. Candy, P. N. Francis and T. J. Hewison, "Monitoring Satellite Radiance Biases Using NWP Models," in *IEEE Transactions on Geoscience and Remote Sensing*, vol. 51, no. 3, pp. 1124-1138, March 2013.

[22] "Global Space-based Inter-Calibration System, GSICS, World Meteorological Organization, http://gsics.wmo.int/index_en.html

[23] "Guide to the Expression of Uncertainty in Measurement (GUM)" Bureau International des Poids et Mesures, Joint Committee for Guides in Metrology (JCGM) 100: 2008.

[24] Randa, J. "Uncertainties in NIST Noise-Temperature Measurements" NIST Technical Note 1502, Mar 1998.

[25] Sandeep, S. & A.J. Gasiewski. "Electromagnetic Analysis of Radiometer Calibration Targets Using Dispersive 3D FDTD" Antennas and Propagation, IEEE Transactions on. vol. 60, iss. 6, 2012. pp. 2821-2828.

[26] Sandeep, S. & A.J. Gasiewski. "Effect of Geometry on the Reflectivity Spectrum of Radiometer Calibration Targets" Geoscience and Remote Sensing Letters, IEEE. Vol. 11, is. 1. 2014. pp. 84-88.

[27] Houtz, D., A.J. Gasiewski, D. Kraft, V. Leuski. "Characterization of Autoemission Reflection at High Frequencies for Precise Radiometer Calibration" National Radioscience Meeting (NRSM), URSI. 2014.

[28] Murk, Axel et al. "Development of Conical Calibration Targets for ALMA" International Symposium on Space Terahertz Technology (ISSTT), Oxford, 2010.

[29] Wylde, R., G. Bell, A. McNamara and A. Murk, "The need for and development of MM-wave radiometer calibration targets with very low coherent backscatter," Precision Electromagnetic Measurements (CPEM), 2012 Conference on, Washington, DC, 2012, pp. 260-261.

[30] Palacios Lázaro, M.Á., M. Bergadà Pujades, R. González Sola, A. Gamonal Coto, J. L. García Fernández and Y. Camacho, "Design, development and calibration of the MWR microwave radiometer on board Sentinel-3," Microwave Conference (EuMC), 2014 44th European, Rome, 2014, pp. 1671-1674.

[31] Murk, A., A. Duric, & F. Patt. "Characterization of ALMA Calibration Targets" Proc. of 19th International Symposium on Space Terahertz Technology, Groningen, 2008. pp. 530-533.

[32] Gu, D., D. Houtz, J. Randa and D. K. Walker, "Extraction of Illumination Efficiency by Solely Radiometric Measurements for Improved Brightness-Temperature Characterization of Microwave Blackbody Target," in IEEE Transactions on Geoscience and Remote Sensing, vol. 50, no. 11, pp. 4575-4583, Nov. 2012.

[33] Fernandez, S., A. Murk and N. Kämpfer, "Design and Characterization of a Peltier-Cold Calibration Target for a 110-GHz Radiometer," in IEEE Transactions on Geoscience and Remote Sensing, vol. 53, no. 1, pp. 344-351, Jan. 2015.

[34] "Plastazote HD60: high density polyethylene foam property data sheet" Zotefoams, Jan, 2004, *http://www.qualityfoam.com/docs/167_HD60.pdf*, accessed Aug 31, 2016.

[35] Almanza, O., MA Rodriguez-Perez, and JA de Saja, "Measurement of the thermal diffusivity and specific heat capacity of polyethylene foams using the transient plane source technique" Polymer International, Vol 53, 2004, pp. 2038-2044.

[36] "Thermal insulation materials made of rigid polyeurethane foam (PUR/PIR) Properties- Manufacture" Federation of European Rigid Polyeurethane Foam Associations, Report No. 1, Oct, 2006, Brussels, Belgium.

[37] "Stycast 2850 FT: Thermally conductive epoxy encapsulant, technical data sheet" Emerson & Cuming, Jun, 2001.

[38] Swenson, C.A. "Linear thermal expansivity (1.5-300 K) and heat capacity (1.2-90 K) of Stycast 2850 FT" Rev. Sci. Instrum., Vol. 68, No. 2, Feb, 1997, pp. 1312-1315.

[39] "Eccosorb CR: Two-Part Castable Load Absorber Series" Emerson & Cuming Microwave Products, Oct, 3008.

[40] "Copper" Wikipedia, *https://en.wikipedia.org/wiki/Copper*, accessed Aug, 31, 2016.

[41] "Material expansion coefficients: linear thermal expansion coefficients of metals and alloys" Laser and Optics User's Manual, Agilent Technologies, Jul, 2002, ch. 17, pp. 3.

[42] "G-10 Fiberglass Epoxy Laminate Sheet" MatWeb Material Property Data. Online resource, accessed Oct 24, 2016. http://www.matweb.com/search/datasheet.aspx?matguid=8337b2d050d44da1b8a9a5e61b0d5f85&ckck=1

[43] P. Cheng. Two-Dimensional Radiating Gas Flow by a Moment Method.
AIAA Journal, 2:1662-1664, 1964.

[44] R. Siegel and J. R. Howell. Thermal Radiation Heat Transfer. Hemisphere Publishing Corporation, Washington DC, 1992.

[45] T. P. Johnson et al., "Design and performance of an ambient calibration target for an airborne microwave and millimeter-wave radiometer," Radio Science Meeting (USNC-URSI NRSM), 2014 United States National Committee of URSI National, Boulder, CO, 2014, pp. 1-1.

[46] A. Murk, A. Schröder, M. Winser, Yichen Qian and R. Wylde, "Temperature/absorption cross integrals and the validation of radiometric temperatures for space-based radiometers," 2016 10th European Conference on Antennas and Propagation (EuCAP), Davos, 2016, pp. 1-3.

[47] P. Yagoubov, A. Murk, R. Wylde, G. Bell and G. H. Tan, "Calibration loads for ALMA," Infrared, Millimeter and Terahertz Waves (IRMMW-THz), 2011 36th International Conference on, Houston, TX, 2011, pp. 1-2.

[48] "Instruction, Platinum Resistance Thermometer Installation" LakeShore Cryotronics, Accessed Jan 18, 2017. http://www.lakeshore.com/Documents/F022-00-00.pdf

[49] A.M. Nicolson, and G.F. Ross, “Measurement of the intrinsic properties of materials by time-domain techniques,” *IEEE Trans. on Instrum. and Meas.,* Vol. 19, Nov, 1970, pp. 377-382.

[50] W.B. Weir, “Automatic measurement of complex dielectric constant and permeability at microwave frequencies,” *Proc. IEEE*, Vol. 62, Jan, 1974, pp. 33-36.

[51] J. Baker-Jarvis, E.J. Vanzura, and W.A. Kissick, “Improved Technique for Determining Complex Permittivity with the Transmission/Reflection Method,” IEEE Trans. on Microw. Theory and Techn., Vol. 38, No. 8, Aug, 1990, pp. 1096-1103.

[52] J. Baker-Jarvis, R.G. Geyer, and P.D. Domich, “A nonlinear least-squares solution with causality constraints applied to transmission line permittivity and permeability determination,” *IEEE Trans. on Instrum. and Meas.,* Vol. 41, No. 5, Aug, 1992, pp. 646-652.

[53] D. A. Houtz, D. Gu and D. K. Walker, "An Improved Two-Port Transmission Line Permittivity and Permeability Determination Method with Shorted Sample," in *IEEE Transactions on Microwave Theory and Techniques*, vol. 64, no. 11, pp. 3820-3827, Nov. 2016.

[54] U.C. Hasar, “A new microwave method based on transmission scattering parameter measurements for simultaneous broadband and stable permittivity and permeability determination,” *Prog. in Electromag. Research,* Vol. 93, May, 2009, pp. 161-176.

[55] J. Baker-Jarvis, M.D. Janezic, J.H. Grosvenor, and R.G. Geyer, “Transmission/reflection and short-circuit line methods for measuring permittivity and permeability,” NIST Project, Boulder, CO, Tech. Note 1355, 1992.

[56] S. Kim, and J. Baker-Jarvis, “An approximate approach to determining the permittivity and permeability near λ/2 resonances in transmission/reflection measurements,” *Prog. in Electromag. Research B*, Vol. 58, Mar, 2014, pp. 95-109.

[57] U.C. Hasar, “Two novel amplitude-only methods for complex permittivity determination of medium- and low-loss materials,” *Meas. Sci. and Tech.*, Vol. 19, Apr, 2008, pp. 55706-55715.

[58] K. Chalapat, K. Sarvala, J. Li, and G.S. Paraoanu, “Wideband reference-plane invariant method for measuring electromagnetic parameters of materials,” *IEEE Trans. on Microw. Theory and Techn.,* Vol. 57, No. 9, Aug, 2009, pp. 2257-2267.

[59] A.H. Boughriet, C. Legrand, and A. Chapoton. “Noniterative stable transmission/reflection method for low-loss material complex permittivity determination,” *IEEE Trans. on Microw. Theory and Techn.,* Vol. 45, No. 1, Jan, 1997, pp. 52-56.

[60] S. Kim, and J.R. Guerrieri, “Low-loss complex permittivity and permeability determination in transmission/reflection measurements with time-domain smoothing,” *Prog. in Electromag. Research M*, Vol. 44, Dec, 2015, pp. 69-79.

[61] N.R. Draper, and H. Smith. Applied Regression Analysis. Wiley, New York, 1998, ch. 24, sec. 2-3, pp. 509, 528.

[62] D.F. Williams, NIST Microwave Uncertainty Framework, Beta Version, http://www.nist.gov/pml/electromagnetics/related-software.cfm, 2011.

[63] J.A. Jargon, D.F. Williams, P.D. Hale, and M.D. Janezic. “Characterizing a noninsertable directional device using the NIST uncertainty framework,” *Proc. ARFTG 83rd Microwave Measurement Conference*, Tampa Bay, FL, Jun. 6, 2014, pp. 1-6.

[64] L.A. Bronckers, and A.B. Smolders, “Broad-band Material Characterization Method Using a CPW with Novel Calibration Technique,” *IEEE Antennas and Wireless Propagation Letters*, vol. PP, no. 99, Feb, 2016, pp. 1-4.

[65] P. Sarafis, E. Hourdakis, and A.G. Nassiopoulou, “Dielectric Permittivity of Porous Si for Use as Substrate Material in Si-Integrated RF Devices,” *IEEE Trans. on Electron. Devices*, vol. 60, No. 4, Apr, 2013, pp. 1436-1443.

[66] I. Zivkovic, A. Murk. “Characterization of Magnetically Loaded Microwave Absorbers,” *Progress in Electromagnetics Research B*, vol. 33, pp. 277-289, 2011.

[67] G. De Amici, R. A. Layton, S. T. Brown and D. Kunkee, "Stabilization of the Brightness Temperature of a Calibration Warm Load for Spaceborne Microwave Radiometers," in *IEEE Transactions on Geoscience and Remote Sensing*, vol. 45, no. 7, pp. 1921-1927, July 2007.

[68] Tsang, L., J.A. Kong, K.H. Ding, “Scattering of Electromagnetic Waves: Theories and Applications” Wiley & Sons, 2000.

[69] Murk, Axel et al. “Development of Conical Calibration Targets for ALMA” *International Symposium on Space Terahertz Technology (ISSTT)*, Oxford, 2010.

[70] Dib, N., M. Asi, A. Sabbah. “On the Optimal Design of Multilayer Microwave Absorbers” *Progress in Electromagnetics Research C*, Vol. 13, pp. 171-185, 2010.

[71] A. Schröder and A. Murk, "Numerical Design and Analysis of Conical Blackbody Targets With Advanced Shape," in *IEEE Transactions on Antennas and Propagation*, vol. 64, no. 5, pp. 1850-1858, May 2016.

[72] E.J. Galvez, “Gaussian Beams,” Department of Physics and Astronomy, Colgate University, 2009.

[73] R. C. Chou and S. W. Lee, "Modal attenuation in multilayered coated waveguides," in *IEEE Transactions on Microwave Theory and Techniques*, vol. 36, no. 7, pp. 1167-1176, Jul 1988.

[74] C. Yeh and G. Lindgren, "Computing the propagation characteristics of radially stratified fibers: an efficient method," Appl. Opt. 16, pp. 483-493, 1977

[75] F.G. Hu, C.F. Wang, Y. Xu, Y.B. Gan, “Modal method analysis of multilayered coated circular waveguide using a modified characteristic equation” Prog. in. Electromag. Research, vol. 45, pp. 243-263, 2004.

[76] S. G. Diamantis, A. P. Orfanidis and G. A. Kyriacou, "Conical Horn Antennas Employing an Offset Moment Method and Mode Matching Technique," in *IEEE Transactions on Magnetics*, vol. 45, no. 3, pp. 1092-1095, March 2009.

[77] “Method of Moments Add-on” TICRA, Copenhagen, accessed Mar 2017, http://www.ticra.com/method-moments-add

[78] G.B. Rybicki and A.P. Lightman, “Radiative Processes in Astrophysics” Wiley-VCH, 1991.

[79] Z. Li, D. Liu, M. Bai, J. Miao and X. Li, "Influence of calibration loads structure on emissivity at millimeter-wave lengths," *Microwave, Antenna, Propagation, and EMC Technologies for Wireless Communications (MAPE), 2011 IEEE 4th International Symposium on*, Beijing, 2011, pp. 798-801.

[80] D. Gu, D. Houtz, J. Randa and D. K. Walker, "Reflectivity Study of Microwave Blackbody Target," in *IEEE Transactions on Geoscience and Remote Sensing*, vol. 49, no. 9, pp. 3443-3451, Sept. 2011.

[81] W.C. Daywitt, “Radiometer equation and analysis of systematic errors for the NIST automated radiometers,” NIST Electromagnetic Fields Division, Boulder, CO, Tech. Note 1327, 1989.

[82] W. J. Emery, W. S. Good, W. Tandy, M. A. Izaguirre and P. J. Minnett, "A Microbolometer Airborne Calibrated Infrared Radiometer: The Ball Experimental Sea Surface Temperature (BESST) Radiometer," in *IEEE Transactions on Geoscience and Remote Sensing*, vol. 52, no. 12, pp. 7775-7781, Dec. 2014.

[83] “Optotherm Support: Emissivity in the Infrared” Optotherm Inc. Last Accessed Feb. 2017, http://www.optotherm.com/emiss-table.htm.

[84] “Emissivity Coefficients of some common Materials” Engineering Toolbox, Last Accessed, Feb. 2017, http://www.engineeringtoolbox.com/emissivity-coefficients-d_447.html.

[85] Y.P. Chen, G.Y. Xu, T.C. Guo, N. Zhou, “Infrared emissivity and microwave absorbing property of epoxy-polyurethance/annealed carbonyl iron composites coatings” Science China: Technology Sciences, vol. 55, no. 3, Mar. 2012, pp. 623-628.

[86] Weng, F., H. Yang, “Validation of ATMS calibration accuracy using Suomi NPP pitch maneuver observations” *Remote Sensing*, vol. 8, is. 332, Apr 2016, pp. 1-14.

[87] D. A. Houtz, D. Gu, D. K. Walker and J. Randa, "An investigation of antenna characterization techniques in microwave remote sensing calibration," *2012 IEEE International Geoscience and Remote Sensing Symposium*, Munich, 2012, pp. 4660-4663.